Advanced TEM Investigations on the Effect of Additives for Reactive Hydride Composites

Zur Erlangung des akademischen Grades eines

Doktors der Ingenieurwissenschaften (Dr.-Ing.)

von der KIT-Fakultät für
Maschinenbau
des Karlsruher Instituts für Technologie (KIT)

genehmigte

DISSERTATION

von

M.Sc. Ou Jin
geb. in China

Tag der mündlichen Prüfung:	11.01.2024
Hauptreferent:	Prof. Dr. Astrid Pundt
Korreferent:	Prof. Dr. Christian Kübel
Korreferent:	Dr. Claudio Pistidda

Kurzfassung

Eine nachhaltige Energiezukunft erfordert die Integration von Wasserstoff als wichtige Komponente. Seit Jahrzehnten wird an der Entwicklung von Materialien zur Wasserstoffspeicherung gearbeitet, um eine umfassende Nutzung von Wasserstoff zu ermöglichen. Unter den modernen Materialien für die Wasserstoffspeicherung haben sich reaktives Hydridkomposite (RHC), wie z.B. $LiBH_4$-MgH_2 und $NaBH_4$-MgH_2, als äußerst vielversprechende Kandidaten erwiesen. Sie weisen eine gravimetrische Speicherkapazität von bis zu 11,5 Gew. % H_2 auf und können theoretisch unter milderen Bedingungen als bestehende kommerzielle Lösungen arbeiten. Allerdings wird die praktische Anwendung insbesondere von $LiBH_4$-MgH_2 durch die langsame Dehydrierungskinetik aufgrund des sich träge bildenden MgB_2 behindert. Es wurde gezeigt, dass Additive die Bildung von MgB_2 erleichtern und die Dehydrierung von $LiBH_4$-MgH_2 beschleunigen können. Die zugrundeliegenden Mechanismen sind jedoch noch nicht ausreichend verstanden. Daher zielt diese Arbeit darauf ab, die Mechanismen zu klären, die die MgB_2-Bildung während der Dehydrierung von $LiBH_4$-MgH_2 beeinflussen, indem verschiedene Variablen wie der Anteil an Additiven, die Temperatur und die Auswirkungen des Zyklierens mittels moderner Methoden der Transmissionselektronenmikroskopie untersucht werden. Es zeigt sich, dass die verbesserte Dehydrierungskinetik von $LiBH_4$-MgH_2 auf das veränderte Nukleations- und Wachstumsverhalten von MgB_2 zurückzuführen ist, was zu unterschiedlichen Morphologien führt. In Abwesenheit von Additiven wurden balkenförmige MgB_2-Kristalle beobachtet, während plättchenförmige MgB_2-Kristalle in Anwesenheit von Additiven beobachtet wurden. Die Kontaktstelle zwischen MgB_2 und den entsprechenden Keimzentren gilt als entscheidend für die Beeinflussung der heterogenen Nukleation und des Wachstums von MgB_2. Durch Analyse der Kristallausrichtungen von MgB_2 und Anwendung des Edge-to-Edge-Matching-Modells wurden die Orientierungsbeziehungen und die elastische Spannungsenergiedichte an der Grenzfläche bestimmt. Es wurde festgestellt, dass die Einführung von Additiven die erforderliche elastische Spannungsenergiedichte signifikant reduziert, was das *in-plane* Wachstum von MgB_2 erleichtert und die morphologischen Veränderung von balkenförmig zu plättchenförmig verursacht. Diese damit verbundene Reduktion der elastischen Energie aufgrund der veränderten Grenzflächensituation führt zu einer erleichterten Bildung der MgB_2-Phase und damit zu einer schnelleren Dehydrierungskinteik. Darüber hinaus können höhere Temperaturen diese Beschränkung teilweise vermindern. Die Auswertung der Ergebnisse nach der Johnson–Mehl–Avrami–Kolmogorov (JMAK) Kinetik zeigen auch, dass die verbesserte

Dehydrierungskinetik bei Einsatz von Additiven mit einem diffusionskontrollierten Wachstum von MgB_2, nicht aber mit einem grenzflächenkontrollierten Wachstum, verbunden ist. Im zyklischen Prozess beruht die Nukleation von MgB_2 auf dem verbliebenen MgB_2, was ebenfalls zu einer starken Verbesserung der Kinetik führt. Daher wird die Kombination von kompatiblen Additiven, die eine geringe elastische Spannungsenergiedichte erreichen, und MgB_2-Nanopartikeln als vielversprechende Lösung angesehen, um die Kinetik von $LiBH_4$ für praktische Anwendungen zu verbessern.

Abstract

A sustainable energy future requires the integration of hydrogen as a vital component. To enable widespread use of hydrogen, the development of materials with enhanced gravimetric hydrogen storage capacity is one key aspect. Amongst the advanced materials for hydrogen storage, $LiBH_4$-MgH_2 and $NaBH_4$-MgH_2, the reactive hydride composites (RHCs), have emerged as highly promising candidates with a high storage capacity of up to 11.5 wt% H_2. In addition, it can theoretically operate under milder conditions compared to existing commercial solutions. However, the slow dehydrogenation kinetics especially of $LiBH_4$-MgH_2 caused by the sluggish formation of MgB_2 hampers its practical application. Transition metal-based additives have been found to facilitate MgB_2 formation and expedite $LiBH_4$-MgH_2 dehydrogenation, although the underlying mechanisms remain poorly understood. Therefore, this research aims to elucidate the mechanisms that influence MgB_2 formation during dehydrogenation exemplary on the system $LiBH_4$-MgH_2, by addressing various variables such as additive content, annealing temperature, and cycling effect using advanced transmission electron microscopy techniques including HRTEM, 4D-STEM and EELS. The results show that the enhanced dehydrogenation kinetics of $LiBH_4$-MgH_2 can be attributed to the altered nucleation and growth behavior of MgB_2, resulting in differing morphologies of MgB_2. In the absence of additives, bar-shaped MgB_2 crystals were observed, whereas platelet-shaped MgB_2 crystals were observed in the presence of additives. The interface between MgB_2 and the corresponding nucleation centers is considered crucial in influencing the heterogeneous nucleation and growth of MgB_2. By analyzing the crystal orientations of MgB_2 and applying the edge-to-edge matching model, the orientation relationships and elastic strain energy density were determined considering different interfaces. It was found that the introduction of additives significantly reduces the required elastic strain energy density, thus facilitating in-plane growth of MgB_2 and causing the morphological change from bars to platelets. This relaxation of the restricted in-plane MgB_2 formation accounts for the improved dehydrogenation kinetics of $LiBH_4$-MgH_2. In addition, higher annealing temperatures can partly alleviate this restriction. The results also demonstrate that the dehydrogenation kinetics improved by introducing additives is associated with diffusion-controlled growth, rather than interface-controlled growth of MgB_2. This verifies the impact of the relevant interface. During cycling, the nucleation of MgB_2 relies on the residual MgB_2, requiring zero strain energy density at the interface and thus leading to a

further improvement in dehydrogenation kinetics. It is suggested here that a combination of compatible additives capable of achieving low elastic strain energy density and MgB_2 nanoparticles are a prospective solution to further enhance the kinetics of $LiBH_4$ for practical applications.

Acknowledgement

I would like to seize this opportunity to express my profound gratitude and appreciation to the individuals and institutions that have significantly contributed to the successful completion of my dissertation.

First and foremost, I extend my deepest gratitude and admiration to my supervisor, Dr. Prof. Astrid Pundt, for her guidance, expertise, and unwavering support throughout my research journey. Her invaluable insights, constructive feedback, and constant encouragement have played an indispensable role in shaping the trajectory and quality of this work.

I would also like to extend my heartfelt appreciation to the co-referee, Prof. Dr. Christian Kübel, for his expertise and invaluable feedback that have immensely contributed to the refinement and overall strength of this dissertation. I am genuinely grateful for his dedicated time, meticulous attention, and scholarly contributions.

Furthermore, I am indebted to the exceptional colleagues and peers from the IAM-WK DIM group and INT EM group who have provided unwavering support and assistance throughout this process. Their intellectual contributions, engaging discussions, and willingness to share resources and knowledge have profoundly enriched my research. I am particularly grateful to Dr. Dorothee-Vinga Szabo, Dr. Di Wang, Dr. Xiaohui Huang, Dr. Xiaoke Mu, Dr. Stefan Wagner, Dr. Sabine Schlabach, Dr. Georgian Melinte, Dr. Svetlana Korneychuk, Dr. Kai Wang, and Dr. Yushu Tang for their collaboration, invaluable insights, and stimulating conversations. I would also like to express my gratitude to my co-workers, Dr. Claudio Pistidda, Dr. Thi Thu Le, and Yuanyuan Shang, from Helmholtz-Zentrum Hereon for their collaboration, unwavering support, and constructive feedback that have positively influenced the development and outcomes of my research.

I am also deeply indebted to the Karlsruhe Nano Micro Facility (KNMFi) for their commitment to academic excellence, provision of state-of-the-art research facilities, and the creation of a supportive research environment. The availability of these resources and the invaluable technical support have been instrumental in conducting my study and achieving meaningful results.

Moreover, I would like to express my gratitude for the financial support provided by the Deutsche Forschungsgemeinschaft (DFG). Their generous funding has not only alleviated financial burdens

but has also empowered me to dedicate myself wholeheartedly to my research. I am profoundly appreciative of their investment in my academic pursuits.

To my beloved grandmother, parents, and fiancée, I extend my sincerest gratitude for their unwavering support, unyielding encouragement, and steadfast understanding throughout this arduous journey. Their unwavering belief in my abilities, immeasurable patience during moments of stress, and motivational words have been a constant source of strength and inspiration.

In conclusion, the completion of this dissertation is an outcome of a remarkable collaborative effort, and I am humbled and deeply grateful for the contributions of each individual and institution mentioned above. Their unwavering support, expert guidance, and genuine encouragement have been the bedrock of this research, shaping its outcomes and ultimately contributing to the advancement of knowledge in the field.

Contents

Abbreviation

ADF	Annular dark-field
BF	Bright-field
CV	Contracting volume
DF	Dark-field
DOS	Density of states
DP	Diffraction pattern
DSC	Differential scanning calorimetry
EELS	Electron energy loss spectroscopy
EDXS	Energy-dispersive X-ray spectroscopy
ELNES	Energy loss near edge structure
EXELFS	Extended energy-loss fine structure
HAADF	High-angle annular dark- field
HRTEM	High-resolution transmission electron microscopy
JMAK	Johnson-Mehl-Avrami-Kolmogorov
PCTF	Phase-contrast transfer function
RDF	Radial distribution function
RHC	Reactive hydride composite
SI	Spectrum Imaging
SIRT	Simultaneous iterations reconstruction technique
SNR	Signal-to-noise ratio

STEM	Scanning transmission electron microscopy
TEM	Transmission electron microscopy
TPD	Temperature-programmed desorption
TVM	Total variation minimization
WPOA	Weak phase object approximation
XRD	X-ray diffraction
CCD	charge-coupled device
CMOS	complementary metal-oxide-semiconductor camera

Symbol

Constants

N_0	Avogadro's number: 6.022141×10^{23}
e	Elementary charge: 1.602176×10^{19} C
a_0	Bohr radius: 5.291772×10^{-11} m
m_0	Mass of electron: 9.109383×10^{-31} kg
c	Speed of light: 299792458 m/s
R	Ideal gas constant: 8.3145 J/(K·mol)
p_0	Atmospheric pressure: 101.325 kPa

Variables

σ_{atom}	Scattering cross section for a single isolated atom
$\sigma_{\mathrm{specimen}}$	Scattering cross section for a specimen
$\frac{d\sigma}{d\Omega}$	Differential cross section
θ	Scattering angle
ρ	Specimen density
t	Specimen thickness
A	Atomic weight of the scattering atoms
σ_{R}	Rutherford differential cross section
Ω	Solid angle
Z	Atomic number

ε_0	Dielectric constant
E_0	Kinetic energy of the incident electrons
$f(\theta)$	Atomic-scattering factor
f_{x}	Scattering factor for X-rays
λ	Wavelength of electron
λ_{R}	Relativistically corrected wavelength of electron
$F(\theta)$	Structure factor
σ_{T}	Ionization cross section
E_{c}	Critical ionization energy for a certain electron shell
n_{s}	Electron number in the ionized sub-shell
θ_{B}	Bragg angle
ΔH	Enthalpy of formation
ΔS	Entropy of formation
T	Temperature
k	Reaction rate constant
α	Fraction of released hydrogen
E_{n}	Activation energy of nucleation
E_{g}	Activation energy of growth
n	Avrami exponent
m	Growth mode parameter
d	Dimensionality of growth

1. Introduction

For achieving a sustainable energy future, it is necessary to incorporate hydrogen as a critical component, considering that hydrogen is a clean and reproducible energy carrier with the gravimetric energy density of about 120 kJ/g, which is the highest among all known substances. However, its widespread use is primarily being restricted by storage techniques [1, 2]. The current commercial solution for storing hydrogen involves primarily compressing hydrogen with an ultra-high pressure of above 10 MPa as a gas or cooling it down to its boiling point of below -253°C as a liquid, using specifically manufactured tanks [3, 4], to improve the volumetric storage capacity of hydrogen. Further restriction of using these tanks to store hydrogen is associated with the difficulty of broadening the application of hydrogen due to their limited hydrogen storage capacity (< 6 wt%), high production cost, and the need to apply harsh conditions. Therefore, a safer, more efficient, and sustainable way of storing hydrogen has been pursued for a long time [5, 6].

One of the promising solutions for safe hydrogen storage is based on alloys, such as $LaNi_5$ [7]. However, these materials only provide a limited hydrogen storage capacity (usually less than 5 wt%). In the last decade, light has been shed on reactive hydride composites (RHCs) in targeting efficient hydrogen storage materials with higher hydrogen storage capacity and milder operation conditions. RHCs were derived from complex metal hydrides (e.g., $LiBH_4$, $LiNH_2$, $NaAlH_4$, etc.) [8, 9], in combination with another metal hydride (e.g., LiH, MgH_2, etc.) [10, 11]. They deliver a gravimetric hydrogen storage capacity of up to around 12 wt%. The development of RHCs is based on the idea that mixing a (complex) metal hydride with another metal (hydride) can tailor the reaction enthalpy, allowing for milder operation conditions for practical applications [12, 13, 14, 15].

One of the most promising candidates among various RHCs for hydrogen storage is $LiBH_4$-MgH_2, with a gravimetric hydrogen storage capacity of around 11.5 wt%. It is one of the target materials to be studied in this work. The overall reaction enthalpy of $LiBH_4$-MgH_2 is reduced to about 41 kJ/mol compared to the original values of 75 kJ/mol for MgH_2 and 74 kJ/mol for $LiBH_4$ [16, 17, 18], leading to the thermodynamic destabilization of both hydrides. The reduction is ascribed to the exothermal formation of MgB_2 during dehydrogenation, leading to an equilibrium temperature of 225 °C under atmospheric pressure [16]. In contrast, the equilibrium temperature

under atmospheric pressure is 370 °C for $LiBH_4$, and it is 278 °C for MgH_2. Although $LiBH_4$-MgH_2 shows impressive hydrogen storage properties, the primary bottleneck that limits its on-board application for vehicles is the sluggish dehydrogenation kinetics. A one-step hydrogenation of $LiBH_4$-MgH_2 was reported by Bösenberg *et al.*, while the dehydrogenation occurs in two steps [19]. Firstly, MgH_2 is decomposed into H_2 and Mg, after which the generated Mg reacts with $LiBH_4$ to form MgB_2 and LiH, releasing the remaining amount of H_2. As RHCs, including $LiBH_4$-MgH_2, contain more than one metal hydride, the reaction of both hydrogenation and dehydrogenation processes is usually more complex than that of a single metal hydride, with the constituent components being involved in different steps of reaction occurring at their interfaces [20]. The sluggish dehydrogenation kinetics is thus suggested primarily as a result of the restriction of MgB_2 nucleation upon the reaction between Mg and $LiBH_4$ [19].

Nanostructuring through ball milling, nanoconfinement using carbon scaffolds, and utilizing additives based on transition metals are the primary focus of current research on enhancing the kinetics of hydride compounds [21, 22, 23, 24, 25, 26]. Additives, in particular, can impressively improve the dehydrogenation kinetics of RHCs while also preserving their hydrogen storage capacities. It has been suggested that the enhanced kinetics in $LiBH_4$-MgH_2 is likely attributed to the facilitation of the heterogeneous nucleation of MgB_2 by additives [27, 28]. However, due to a lack of thorough microscopic investigations, the exact role played by these additives in promoting dehydrogenation kinetics has not yet been explicitly clarified. In this work, investigations on a nanoscale were carried out using transmission electron microscopy (TEM) to study the microstructural evolution of MgB_2 in samples with and without Ti- and Al-based additives by using transmission electron microscopy (TEM). This illuminates the details of how the microstructure of materials affects the dehydrogenation kinetics of the system. Furthermore, the influence raised by relevant factors such as the additive content, the annealing temperature, and the cycling effect on the kinetics of $LiBH_4$-MgH_2 were also studied to help understand the underlying mechanism of MgB_2 formation. In order to extend the existing knowledge acquired from $LiBH_4$-MgH_2, both ex-situ and in-situ TEM analyses were conducted on the reactive hydride composite $NaBH_4$-MgH_2. The reason for this is that a similar two-step dehydrogenation process is observed in $NaBH_4$-MgH_2 as in $LiBH_4$-MgH_2. Furthermore, the dehydrogenation process of $NaBH_4$-MgH_2 requires significantly lower backpressure, making it well-suited for the available environmental gas cell system used in in-situ TEM experiments [29, 30].

This work comprises seven chapters. In Chapter 2, the most relevant materials for hydrogen storage, including the reactive hydride composites for this work, are introduced along with their mechanisms for kinetics and representative strategies for improving kinetics. In Chapter 3, the basics of TEM is described. Chapter 4 specifies the experimental details of this work, including the preparation of related samples, X-ray Diffraction analysis, kinetics measurements, and the

materials characterization by TEM experiments. The relevant results and discussion are presented in Chapters 5 and 6, respectively. Chapter 7 summarizes this work and provides outlooks.

2. Hydrogen Storage

Despite hydrogen possessing nearly three times the energy content of gasoline, with 120 MJ/kg for hydrogen versus 44 MJ/kg for gasoline, the practical application of hydrogen is limited due to gravimetrical storage issues. This chapter explores various aspects of hydrogen storage, outlining the key techniques of storing hydrogen in Section 2.1. Section 2.3 primarily focuses on the reactive hydride composites $LiBH_4$-MgH_2 and $NaBH_4$-MgH_2, as they are the primary focus of this study. Section 2.4 presents the relevant theories of kinetics and the edge-to-edge matching model for this work.

2.1. Hydrogen Storage Systems

Table 2.1.: Overview of important key parameters determined by the U.S. DOE technical system goals for onboard hydrogen storage in light-duty vehicles [31].

	2020	**2025**	**Ultimate**
System-based gravimetric capacity [kg H_2/kg system]	0.045	0.055	0.065
System-based volumetirc capacity [kg H_2/L system]	0.030	0.040	0.050
Min/Max delivery temperature [°C]	-40/85	-40/85	-40/85
Min/Max delivery pressure from tank [MPa]	0.5/1.2	0.5/1.2	0.5/1.2
Operational cycle life (1/4 tank to full) [cycles]	1500	1500	1500
Boil-off loss target (max reduction from initial 95 % Usable capacity after 30 days) [%]	10	10	10

The various hydrogen storage systems that have been implemented or are currently under active investigation can be categorized into two groups: physical-based storage systems, which rely on different types of tanks, and material-based storage systems, which utilize material media for hydrogen storage. The U.S. Department of Energy (DOE) has determined the target parameters for an optimal hydrogen storage system for the years 2020, 2025, and the ultimate future, as

highlighted in Table 2.1. Consequently, the ultimate objective for a hydrogen storage system includes achieving a gravimetric hydrogen storage capacity of at least 6.5 wt%, a volumetric capacity of 5.0%, an operating temperature range of -40 to 85°C, an operating pressure of less than 1.2 MPa, and so forth.

2.1.1. Physical-based Storage

Physical-based storage systems rely on specially designed containers to store hydrogen. The hydrogen stored using this method can be in either a gaseous or liquid state, depending on the temperature and pressure conditions applied.

2.1.1.1. Gaseous-state Storage

Compressed hydrogen gas is a well-established method for hydrogen storage, particularly for fuel cell electric vehicles [5, 32, 33, 34]. The low volumetric density of gaseous hydrogen, at 0.09 g/L under standard temperature and pressure conditions [35, 36], requires storage tanks to operate under high pressure (35 MPa or 70 MPa) to improve the volumetric storage capacity. However, this increased pressure demands strong and durable materials for the construction of the storage tanks.

Despite its technical maturity, compressed hydrogen gas storage has several critical drawbacks that need be addressed. The most significant disadvantage is the high pressure required to store gaseous hydrogen, which exceeds the target pressure set by the Department of Energy (up to 1.2 MPa, as shown in Table 2.1). This high pressure can lead to safety concerns and public apprehension. Another major issue is the cost of storage tanks, which drives up the price of hydrogen vehicles and could reduce public acceptance of this technology, hindering its widespread adoption [32].

Current solutions used by automotive industry leaders such as Toyota and Hyundai utilize a combination of a high-density polymer liner and a carbon fiber-reinforced plastic shell for their compressed gaseous hydrogen storage tanks [37, 38]. This lightweight solution reduces the weight of the tank, allowing it to store up to 5 kg of hydrogen at a pressure of 70 MPa, resulting in a storage capacity of around 5 wt%. The polymer liner is impervious to hydrogen, while the carbon fiber-reinforced plastic shell provides necessary strength and impact resistance.

2.1.1.2. Liquid-state Storage

Storing hydrogen in its liquefied form is a crucial technique for hydrogen storage due to its high density and high energy content. Hydrogen's strong repulsive interaction causes its critical temperature to drop to -253 °C, resulting in a dense liquid form with a density of 70.85 g/L, nearly twice that of compressed hydrogen gas at 70 MPa [36]. Given the largest gravimetric energy density of approximately 120 MJ/kg for hydrogen, liquid hydrogen is commonly used as a rocket fuel in combination with liquid oxygen for space travel [39].

However, a major challenge in storing hydrogen in its liquid form is the constant hydrogen loss. Maintaining the low temperature required to keep the hydrogen in a liquid state can consume 20-30 % of the stored hydrogen's total energy content [40], while the continuous evaporation of the liquid hydrogen (the boil-off effect) results in a daily loss of 0.3-3 % of the stored hydrogen [41]. This daily loss in hydrogen is not acceptable for medium- or long-term storage, as shown in Table 2.1. The limited storage space and energy loss associated with storing hydrogen in its liquid form make it suitable for frequent-travelling vehicles like trucks. On the other hand, for vehicles with lower usage frequency that necessitate long-term hydrogen storage, storing hydrogen in liquid form is not practical.

One noteworthy aspect of the physical-based storage systems using ultra-high pressure or ultra-low temperature is that the hydrogen which is released will be permanently lost and vanish in the high stratosphere or even into space due to its lowest atomic weight. In other words, a continuous hydrogen production is heavily relied upon by the physical-based storage systems, leading to a continuous loss of hydrogen from earth as a consequence. In this regard, the material-based storage systems are considered a more sustainable way of storing hydrogen.

2.1.2. Material-based Storage

Material-based hydrogen storage can be generally categorized into adsorbent materials, chemical hydrogen storage materials, and metal hydride materials, involving varying research focus on improving the hydrogen storage properties.

2.1.2.1. Adsorbent Materials

Adsorbent materials involve the physical storage of hydrogen molecules absorbed onto solid materials such as carbon materials (e.g. carbon nanotubes and fibers) and metal-organic frameworks (MOFs) through van der Waals forces [42, 43, 44, 45]. Thermal stimulation easily achieves the release of the hydrogen molecules, due to the weak interaction between hydrogen and the material,

leading to fast sorption kinetics. A previous study [46] reported that the porous carbon material KUA6 has a gravimetric hydrogen storage capacity of 8 wt% under the conditions of 77 K and 4 MPa excluding the tank weight, but only 3.2 wt% under the conditions of 298 K and 20 MPa. Increasing the effective adsorption temperature while preserving hydrogen capacity has been an area of research, due to low hydrogen storage capacities at ambient temperature and pressure conditions. Additionally, improving their volumetric and gravimetric storage capacities through optimizing the material's pore size, increasing pore volume, and surface area is the subject of intensive effort [47, 48].

2.1.2.2. Chemical Hydrogen Storage Materials

Chemical hydrogen storage materials generally consist of compounds that have the highest density of hydrogen, with covalently bound hydrogen and are mostly composed of light elements [49]. Representative examples, such as methanol CH_4O, ammonia NH_3, ammonia borane BH_6N, and formic acid CH_2O_2, deliver significant hydrogen storage capacities. However, the widespread utilization of these materials as large-scale hydrogen storage media faces several challenges, such as toxicity and corrosion [50, 51, 52]. Additionally, most methanol today is produced from fossil fuels, making green methanol production a significant challenge [53]. Furthermore, hydrogen release from chemical hydrogen storage materials is usually an exothermic process or an endothermic process with a small enthalpy, allowing only for off-board rehydrogenation procedures. Hence, the development of efficient regeneration processes for the spent storage material is necessary for the practical application [54].

2.1.2.3. Metal Hydride Materials

Metal hydrides are generally divided into interstitial metal hydrides and complex metal hydrides [11, 36, 55]. The most simple interstitial metal hydrides can be represented as MH_x, where M usually refers to light metal elements [56], including lithium Li, sodium Na, magnesium Mg, and heavy metal elements, including palladium Pd [57, 58]. Magnesium, extensively studied for hydrogen storage, has many benefits, including abundant reserves, low production and material costs, ability to withstand impurities in hydrogen, and a high hydrogen storage capacity of up to 7.6 wt% in MgH_2 [59] (as seen in Table 2.2). However, the practical applications of MgH_2 are hindered by high thermodynamic stability, slow reaction kinetics, and low characteristic thermal conductivity. [60, 61, 62]. Additionally, the high reactivity of Mg can lead to the formation of surface passivation oxide layers (SPLs) that can isolate the metal from interacting with hydrogen [63]. Although deactivated Mg can be reactivated by high temperatures, the SPLs may not be entirely removed, and a portion of magnesium may remain permanently inactive.

Interstitial metal hydrides can also be based on alloys. Representatives of hydrogen storage solutions in this regard include AB, AB_2, A_2B, and AB_5 alloys [64]. Examples of these alloy hydrides are shown in Table 2.2 [65, 66, 67, 68]. These alloys are composed of metallic elements A and B, with A usually representing elements with high hydrogen affinity, while B refers to transition metals with low hydrogen affinity [69]. The main advantage of using alloys for hydrogen storage is that they can store and release hydrogen at moderate temperatures and pressures, making them a safer option for widespread use. However, their hydrogen storage capacity remains limited, typically below 4 wt% and does not meet the DOE targets for hydrogen storage, as shown in Table 2.1.

Table 2.2.: Hydrogen storage properties of various metal hydrides.

Hydride Type	Desorbed State	Absorbed State	Hydrogen Storage Capacity [wt%]	Desorption Temp. at 0.1 MPa [°C]	Ref.
M	Mg	MgH_2	7.6	275	[60]
AB	FeTi	$FeTiH_2$	1.9	-8	[70]
AB_2	$ZrMn_2$	$ZrMnH_2$	1.8	440	[70]
A_2B	Mg_2Ni	Mg_2NiH_4	3.6	280	[71]
AB_5	$LaNi_5$	$LaNiH_6$	1.4	16	[72]
Complex	LiH&B	$LiBH_4$	13.6	370	[18]

Complex metal hydrides are created by forming mixed ionic-covalent compounds, typically consisting of lightweight metal cations such as Li^+, Na^+, and Mg^{2+}, and hydrogen-containing "complex" anions such as alanates $[AlH_4]^{-1}$ and borohydrides $[BH_4]^{-1}$ [73]. Complex metal hydrides, like $LiBH_4$, are particularly attractive for hydrogen storage due to their impressive hydrogen storage capacity as shown in Table 2.2. However, the poor intrinsic thermodynamics of $LiBH_4$ leads to the reversibility being only allowed under harsh conditions. For dehydrogenation, a temperature of up to 370 °C under atmospheric pressure is required to make $LiBH_4$ undergo the process, while hydrogenation requires even harsher conditions of temperatures reaching up to 600 °C and a pressure of 15.5 MPa [18].

2.2. Thermodynamics of Hydride Formation and Decomposition

The formation of metal hydrides $\mathrm{MH_2(s)}$ occurs through the interaction between gaseous hydrogen $\mathrm{H_2(g)}$ and the metal-based solid M(s), which is a reversible process. Reaction 1 provides a simplified overview of the reaction and does not take into account the complexities involved [36].

$$\mathrm{M(s)} + \frac{\mathrm{x}}{2}\mathrm{H_2(g)} \rightleftharpoons \mathrm{MH_x(s)} + \mathrm{Q} \qquad \{1\}$$

In the chemical equation above, Q refers to the heat of reaction. If the hydrogenation process is exothermic, and the dehydrogenation process is endothermic, Q has a positive value. The operating temperature and pressure required for the reversible reaction of the metal hydride system will vary depending on the specific metal M(s) used. The required conditions are determined by the interplay of both thermodynamics and kinetics in the metal hydride system.

A commonly used approach to determine the thermodynamic properties of these metal hydrides is to plot their pressure-composition-isotherms (PCIs). Figure 2.1a illustrates an example of PCIs measured at various temperatures, with the x-axis representing the hydrogen composition c_H (or [H/M]) in M(s) and the y-axis representing pressure. T_c refers to the critical temperature. When the applied temperature is below T_c, a PCI curve can be divided into three sections, each representing a different stage of (de)hydrogenation: α phase, coexistence of α and β phases, and β phase. The higher the temperature, the shorter the plateau of the coexistence of α and β phases. When the temperature exceeds T_c, the plateau vanishes.

For the purpose of clarity, the hydrogenation process of interstitial metal hydrides is depicted in a schematic manner in Figure 2.1b. The following explanation provides a detailed description of the process with step a through f [36, 74]:

(i) Hydrogen gas molecules from the environment are physically adsorbed onto the surface of M(s) through the van der Waals force (step a).

(ii) The adsorbed hydrogen molecules $\mathrm{H_2}$ can dissociate into H atoms by overcoming an activation barrier and form hydrogen-metal bonds, also known as dissociative chemisorption, as shown in Figure 2.1c (step b). The activation barrier for this process depends on the surface elements involved.

(iii) The chemically adsorbed H atoms can penetrate the surface of M(s) and diffuse into the host lattice via the subsurface layer (step c).

(iv) Within the host lattice, the potential energy of the interstitial sites (octahedral or tetrahedral holes) is lower than its surroundings, causing H atoms to occupy these interstitial sites and form a solid solution, also known as the α phase (step d). This corresponds to what is shown in Figure 2.1a, and is usually generated during the hydrogenation process when the hydrogen composition c_{H} is generally less than 10^{-4} in the case under consideration..

(v) As c_{H} increases and the lattice expands, hydrogen-hydrogen interactions become visible, triggering nucleation and growth of the hydride phase, i.e. β phase. According to the study by Baldi *et al.* [75], the hydride formation progresses from the outer to the inner part of palladium nanocrystals, and the interface between α and β phases shifts inward with increasing c_{H}, as shown in Figure 2.1b (step e and f). During this stage, α and β phases coexist and the increment in c_{H} can be achieved under constant pressure until the α phase has completely transitioned into the β phase. To store additional hydrogen, a further increase in hydrogen pressure is then required, as shown in Figure 2.1a.

The plateau region of the hydrogenation process is characterized by the equilibrium pressure p_{eq}, which is related to the enthalpy and entropy of reaction. However, the equilibrium pressure is not constant and may show hysteresis, meaning that the pressure measured during hydrogenation and dehydrogenation may differ. This behavior has been attributed to localized lattice defects and stress energy induced by the lattice expansion [75, 77]. The Van't Hoff equation can be used to describe the relationship between equilibrium pressure and temperature (see Equation 2.1), where p_0 is the standard pressure, ΔH is the enthalpy of reaction, ΔS is the entropy of reaction, and R is the ideal gas constant [78].

$$\ln \frac{p_{\mathrm{eq}}}{p_0} = -\frac{\Delta H}{RT} + \frac{\Delta S}{R} \tag{2.1}$$

The Van't Hoff plot, which is derived from Equation 2.1, allows for determining the enthalpy and entropy of reaction in the (de)hydrogenation process. By plotting $\ln\frac{p_{\mathrm{eq}}}{p_0}$ against $\frac{1}{T}$, a linear relationship is observed and the plot results in a straight line, as seen in Figure 2.1a (right part). The slope of the line represents the enthalpy of reaction (ΔH) and the intercept represents the entropy of reaction (ΔS). These thermodynamic parameters can be used to calculate the minimum temperature required for the (de)hydrogenation process to occur at a given pressure, without taking into account any kinetic restrictions. It is important to note that the (de)hydrogenation process in complex metal hydrides may involve multiple-step and side reactions, making it more complicated than the process in interstitial metal hydrides.

Unfortunately, one of the major challenges for metal hydrides is to strike the right balance between hydrogen storage capacity and operating conditions for the (de)hydrogenation process. The number of interstitial sites interstitial metal hydrides can provide is often limited, thereby

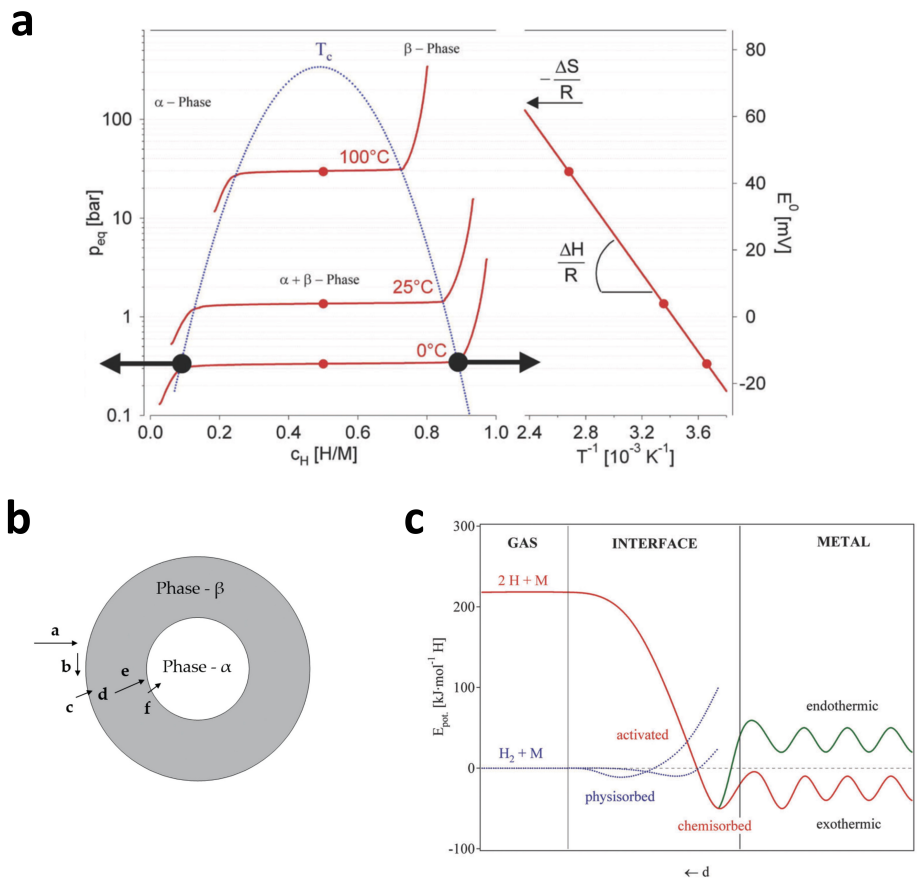

Figure 2.1.: (a) Pressure-Composite-Isotherms (PCIs) for metal hydrides at different temperatures, see the left part. Below the critical temperature T_c, a PCI curve can be divided into α phase, coexistence of α and β phases, and β phase . The pressure associated to the plateau at a certain temperature gives the corresponding equilibrium pressure. According to the Van't Hoff equation, a straight line can be plotted showing the linear relationship between $\ln p_{eq}$ and $\frac{1}{T}$, see the right part. In this way, the enthalpy and the entropy of reaction of the hydride system can be determined through measuring the slope and the intercept; (b) Schematic illustration of hydrogenation for metallic hydrides from step a through step f; (c) One-dimensional potential energy curve that describes the required potential energy throughout the dehygrogenation or hydrogenation process of metallic hydrides, corresponding to an endothermic or exothermic reaction, respectively. Figure courtesy [36, 74, 76].

impeding their hydrogen storage capacity. However, the (de)hydrogenation processes for interstitial metal hydrides can be carried out under milder temperature and pressure conditions due to the weaker ionic metal-hydrogen bond. Complex metal hydrides, on the other hand, can provide high gravimetric hydrogen storage capacities as they are lightweight and free of interstitial limitation. However, their (de)hydrogenation process often requires harsh conditions primarily due to covalent

bonding in hydrogen. To overcome these challenges, it is necessary to further develop advanced hydrogen storage materials that offer improved performance, see Section 2.3.

2.3. Reactive Hydride Composite (RHC)

Reilly et al. [12] first proposed the possibility of improving the thermodynamic properties of MgH_2 by alloying it with Cu. The idea of improving the intrinsic thermodynamics by synergistically lowering the overall reaction enthalpy while still preserving a high gravimetric hydrogen storage capacity was further developed by Chen *et al.*, Vajo *et al.*, and Barkhordarian *et al.* [13, 14, 15], with two or even more hydrides being mixed. This concept brought about the creation of reactive hydride composite (RHC), which includes $LiBH_4$-MgH_2 and $NaBH_4$-MgH_2 as representative examples, and which are also the target materials for this work.

The reactive hydride composite (RHC), which is defined by the combination of two or more different hydrides, is known to offer a promising solution for balancing the thermodynamic properties and the hydrogen storage capacity. Two promising RHC materials $LiBH_4$-MgH_2 and $NaBH_4$-MgH_2, which are also the focus of this work, are introduced in this section. Subsection 2.3.1 and 2.3.2 provide a comprehensive examination of the material properties of $LiBH_4$-MgH_2 and $NaBH_4$-MgH_2, respectively. In addition, the challenges and limitations of these materials for practical applications are thoroughly discussed.

2.3.1. Lithium-RHC $LiBH_4$-MgH_2

The gravimetric hydrogen storage capacity is a crucial parameter for evaluating the potential of a material for hydrogen storage. It remains one of the major limitations for practical applications of hydrogen storage materials. As discussed in the previous section, $LiBH_4$ has received significant attention due to its impressive gravimetric hydrogen storage capacity of up to 18.5 wt% and high volumetric hydrogen storage capacity of 0.121 kg H_2/l [71]. Up to 13.6 wt% of hydrogen is released through the reversible (de)hydrogenation process of $LiBH_4$, as illustrated in Reaction 2. The total capacity can go up to 18.5 wt% if the generated LiH undergoes further decomposition, while harsher conditions are required for the regeneration of $LiBH_4$.

$$LiBH_4 \rightleftharpoons LiH + B + \frac{3}{2}H_2 \qquad \{2\}$$

However, the high thermodynamic stability of $\mathbf{LiBH_4}$ necessitates harsh conditions for both the hydrogenation and dehydrogenation processes. The temperature required for dehydrogenation

was reported by Orimo *et al.* [79] using differential scanning calorimetry (DSC). According to their study, three peaks were determined in the differential scanning calorimetry (DSC) profile for $LiBH_4$ when $LiBH_4$ was annealed under atmospheric pressure. These peaks corresponded to the structural transition of $LiBH_4$ from orthorhombic to hexagonal (around 103 °C), melting (around 277 °C), and decomposition into LiH, B and H_2 (around 330-430 °C) [79, 80], respectively. Moreover, Mauron *et al.* determined the enthalpy of reaction ΔH being 74 kJ/mol and the entropy of reaction ΔS being 115 J/(K·mol) for $LiBH_4$, relying on the Van't Hoff equation (see Equation 2.1) [18]. A temperature T_{eq} of 370 °C is reached at standard pressure and 440 °C is reached under 0.4 MPa (applied pressure for this work) for dehydrogenation. It was also reported that the reaction of Equation 2 for hydrogenation could only be reversed under even harsher conditions, as observed in their temperature-programmed desorption (TPD) measurements [18]. Specifically, a temperature of 600 °C and a pressure of 15.5 MPa were required.

The abundance, low cost, and high hydrogen storage capacity of $\mathbf{MgH_2}$ make it a promising material for solid-state hydrogen storage. With a gravimetric capacity of 7.6 wt% and a volumetric capacity of 0.110 kg H_2/L, MgH_2 has the potential to play an important role in the development of practical hydrogen storage systems. However, one of the major challenges associated with MgH_2 is also the high thermodynamic stability, which results in the need for high temperatures to achieve the hydrogenation and dehydrogenation reactions. According to the Van't Hoff equation, the enthalpy of reaction for the (de)hydrogenation of MgH_2 is estimated to be around 75 kJ/mol, with an entropy of reaction in the range of 126 to 146 J/(K·mol) [17]. A temperature of approximately 278 °C is attained at atmospheric pressure, and approximately 320 °C is attained under 0.4 MPa.

To improve the performance in hydrogen storage for these materials, the mixture of $LiBH_4$ and MgH_2, which is $LiBH_4$-MgH_2 was emphatically studied in last 20 years [16], which delivers a hydrogen storage capacity of about 11.5 wt% while being thermodynamically destabilized. The reversible (de)hydrogenation process of this system is illustrated in Reaction 3. It should be noted that after dehydrogenation, one hydrogen atom is still retained by the generated LiH, which contributes to the reversibility of the Li-RHC system.

$$2\,LiBH_4 + MgH_2 \rightleftharpoons 2\,LiH + MgB_2 + 3\,H_2 \qquad \{3\}$$

The combination of $\mathbf{LiBH_4}$ and $\mathbf{MgH_2}$ has shown significant improvement in thermodynamics. According to the Van't Hoff plots in the study by Vajo *et al.*, the reversible (de)hydrogenation process of $LiBH_4$-MgH_2 has a remarkably reduced enthalpy of 40.5 kJ/mol and an entropy of 81.3 J/(K·mol), leading to an equilibrium temperature of 225 °C under atmospheric pressure [16]. This represents a significant decrease in the equilibrium temperature under atmospheric pressure

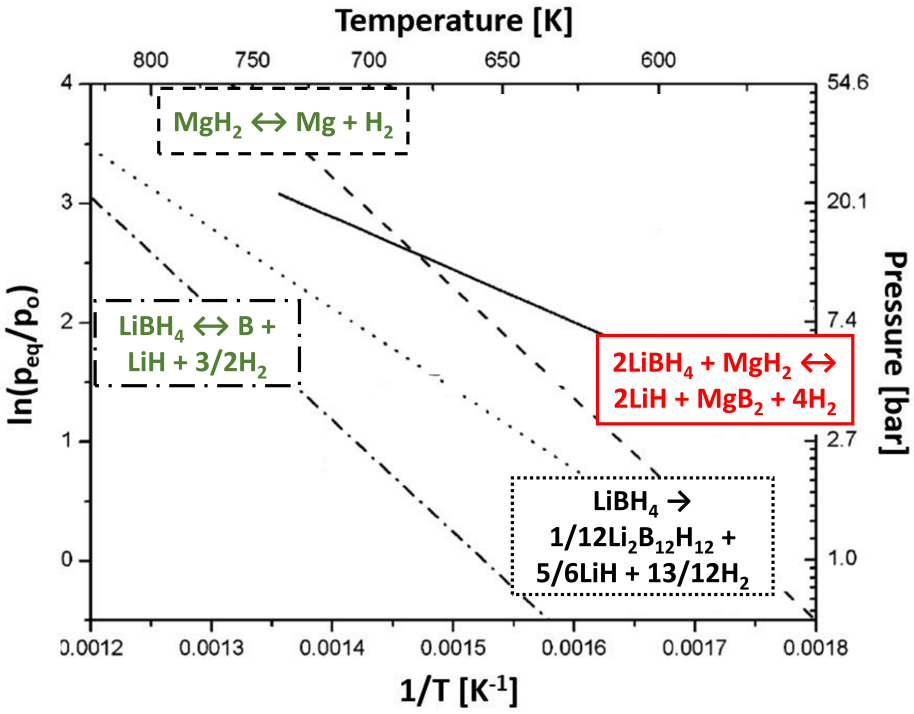

Figure 2.2.: The Van't Hoff plots of MgH_2[81], $LiBH_4$ [18, 82], $LiBH_4$-MgH_2 [16], revealing the relationship between the equilibrium pressure and the corresponding equilibrium temperature for the respective materials. Figure courtesy [83].

compared to individual materials, with $LiBH_4$ having an equilibrium temperature of 370 °C and MgH_2 having an equilibrium temperature of 278 °C under atmospheric pressure. This improvement is attributed to the exothermic formation of MgB_2 resulting from the reaction between $LiBH_4$ and Mg, which effectively lowers the enthalpy of reaction for the endothermic dehydrogenation process [84]. This is reflected in the much less steep slope observed for $LiBH_4$-MgH_2, in comparison to that of $LiBH_4$ and MgH_2, as illustrated in Figure 2.2.

Bösenberg *et al.* [19] proposed that the **hydrogenation** process of the $LiBH_4$-MgH_2 system occurs in a single step, as shown in Reaction 4. In contrast, the **dehydrogenation** process occurs in two steps, according to their findings from DSC and in-situ X-ray diffraction (XRD) measurements, as described in Reaction 5. This two-step process involves first the decomposition of MgH_2 into Mg and H_2, followed by a reaction between Mg and $LiBH_4$ to produce LiH, MgB_2, and H_2. This two-step dehydrogenation reaction can also be illustrated by the in-situ XRD experiments in Figure 2.3. At about 310 °C, the disappearance of the peaks of MgH_2 is observed, followed by the appearance of peaks of Mg, indicating the occurrence of the decomposition of MgH_2 into Mg and H_2. As the temperature is raised to about 400 °C, the peaks of MgB_2 start appearing, overlapping

with that of Mg. This indicates a slow progress of the second step of the dehydrogenation. Furthermore, at about 270 °C, the disappearance of the peaks of $LiBH_4$ is observed, which can be attributed to its melting behavior, considering the melting point of $LiBH_4$ being about 278 °C. In addition, the identification of LiCl in this instance was attributed to the reaction between $LiBH_4$ and the additive $3TiCl_3{\cdot}AlCl_3$, a discussion of which is provided in detail in Chapters 6.

One-step reaction:

$$2\,LiH + MgB_2 + 3\,H_2 \longrightarrow 2\,LiBH_4 + MgH_2 \quad \{4\}$$

Two-step reaction:

$$2\,LiBH_4 + MgH_2 \longrightarrow 2\,LiBH_4 + Mg + H_2 \longrightarrow 2\,LiH + MgB_2 + 3\,H_2 \quad \{5\}$$

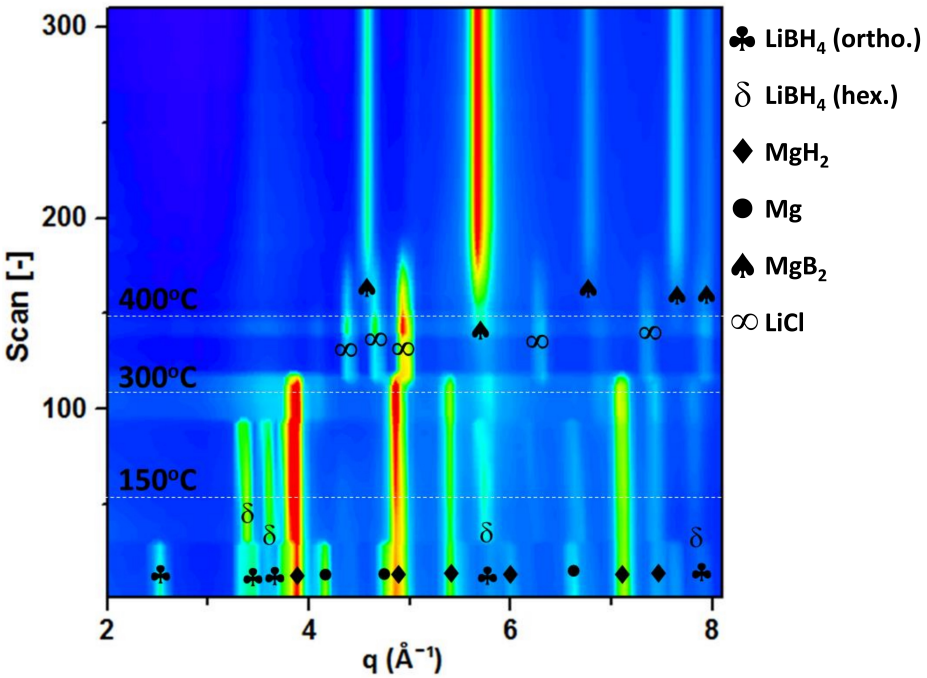

Figure 2.3.: In-situ synchrotron radiation powder X-ray diffraction for the dehydrogenation process of $LiBH_4$-MgH_2 with the additive $3TiCl_3{\cdot}AlCl_3$ from room temperature to 400 °C. The measurement was performed with a heating rate of 5 °C/min and under a hydrogen pressure of 0.3 MPa. Figure courtesy [85].

Although the equilibrium temperature for the dehydrogenation process of $LiBH_4$-MgH_2 is predicted at around 225 °C (at a pressure of 0.1 MPa) based on thermodynamic analysis,

dehydrogenation in practice requires higher temperatures and pressures. As demonstrated by the measurements depicted in Figure 2.4, a temperature of 400 °C and a pressure of 0.5 MPa H_2 were employed. It can be observed that even under these conditions, the dehydrogenation process takes more than 10 hours for the majority of the samples. The presence of a long incubation plateau, as depicted in the figure, is the primary factor contributing to the sluggish kinetics observed in most samples.

Previous research [19, 86] has established that the hydrogen release observed before and after the incubation plateau in Figure 2.4 can be attributed to the decomposition of MgH_2 (around 2.9 wt%H_2) and the reaction between $LiBH_4$ and Mg into LiH and MgB_2 (about 8.6 wt%H_2), respectively, as described in the two steps of Reaction 5. The lengthy incubation plateau observed in between is believed to be the result of slow nucleation of MgB_2. Thus, the sluggish nucleation of MgB_2 is deemed to be the primary factor hindering the dehydrogenation kinetics of $LiBH_4$-MgH_2. In this work, a detailed study of the microstructure of MgB_2 is conducted to illuminate the nucleation of MgB_2. This is motivated by the fact that the microstructure of MgB_2, which has implications for its nucleation process, has remained unclear until now.

It was discovered that the most effective methods for accelerating the dehydrogenation process are nanostructuring [87], nanoconfinement [88], and the use of transition metal additives [27, 89]. As demonstrated in Figure 2.4, ball milling preparation or the addition of additives significantly shortens the incubation plateau or even eliminates it, as illustrated in Figure 2.4.

The need for harsh conditions, such as a higher back pressure, in the dehydrogenation process of $LiBH_4$-MgH_2 is to mitigate the potential for side reactions that could negatively affect the reversibility and hydrogen storage capacity of this material. Studies by Yan *et al.* [90] and Kim *et al.* [86] have shown that under hydrogen pressures of less than 1.0 MPa, the formation of an intermediate compound $Li_2B_{12}H_{12}$ may occur during the dehydrogenation process. This intermediate compound is not reversible and can impact the hydrogen storage capacity and dehydrogenation kinetics of $LiBH_4$-MgH_2. To suppress the generation of this by-product and to promote the formation of MgB_2, a back pressure of 0.4 MPa H_2 is applied, based on other relevant studies [28, 85, 91]. Accordingly, although a small amount of $Li_2B_{12}H_{12}$ may still be generated under 0.4 MPa H_2, it is considered acceptable in terms of both the damage to hydrogen storage capacity and cycling of $LiBH_4$-MgH_2. Based on the Van't Hoff equation for the dehydrogenation of $LiBH_4$-MgH_2, a temperature higher than 307°C is required to attain an equilibrium pressure of 0.4 MPa H_2, as shown in Figure 2.2.

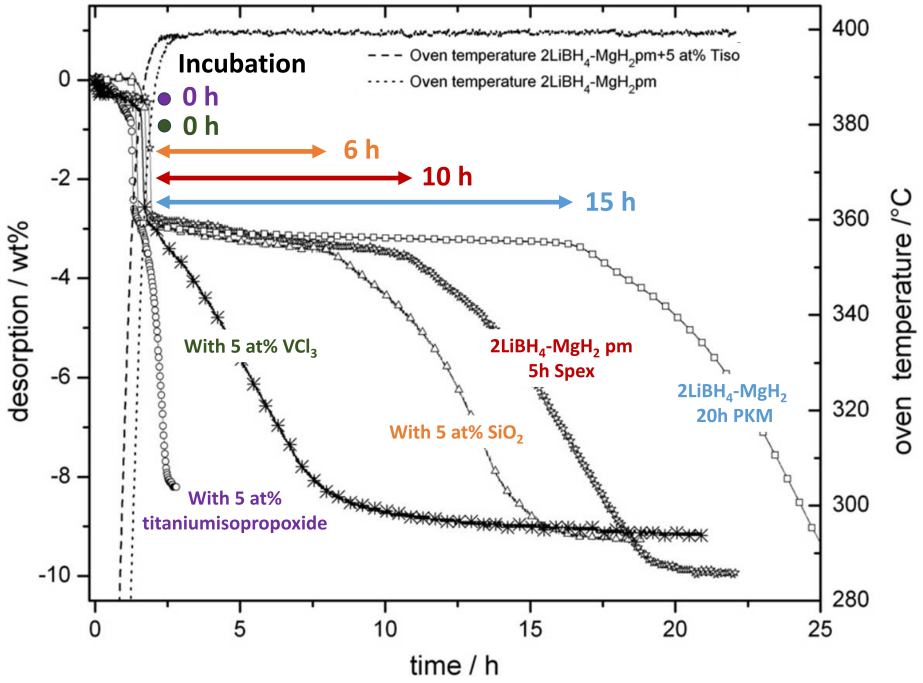

Figure 2.4.: The performance in dehydrogenation kinetics of $LiBH_4$-MgH_2 measured at 400°C under 0.5 MPa hydrogen pressure in a Sievert-type apparatus. These samples were prepared using various methods including additives and ball milling. PM stands for pre-milling, Spex for Spex Mixer Mill and PBM for planetary ball mill. Figure courtesy [19].

2.3.2. Sodium-RHC $NaBH_4$-MgH_2

In addition to $LiBH_4$-MgH_2, this work also address the reactive hydride composite $NaBH_4$-MgH_2. Since lithium and sodium are in the same group of elements, they are anticipated to have similar hydrogen storage properties. Indeed, $NaBH_4$ has a high hydrogen storage capacity of 10.8 wt% and a hydrogen density of 0.120 kg H_2/L [92]. On top of these properties, sodium is a much more abundant and cheaper material than lithium. The decomposition of $NaBH_4$ follows a different reaction path, as described in Reaction 6.

$$NaBH_4 \longrightarrow Na + B + 2\,H_2 \qquad \{6\}$$

In contrast to the decomposition of $LiBH_4$ (as shown in Reaction 2), the decomposition of $NaBH_4$ involves the simultaneous formation of Na. This is due to the lower thermodynamic stability of NaH compared to LiH (as the enthalpy of formation for NaH is -113 kJ/mol, while the enthalpy of formation for LiH is -233 kJ/mol) and the strong ionic bonds between Na^+ and BH_4^-

that contribute to the high stability of $NaBH_4$ [93, 94]. According to Van't Hoff plot analysis, the enthalpy and entropy of reaction for the decomposition of $NaBH_4$ are 108 kJ/mol and 133 J/(K·mol), respectively. These values correspond to a decomposition temperature of around 534 °C at atmospheric pressure (as shown in Reaction 6). Additionally, $NaBH_4$ has a melting point of approximately 400 °C, which is higher than the melting point of about 278 °C for $LiBH_4$ [95].

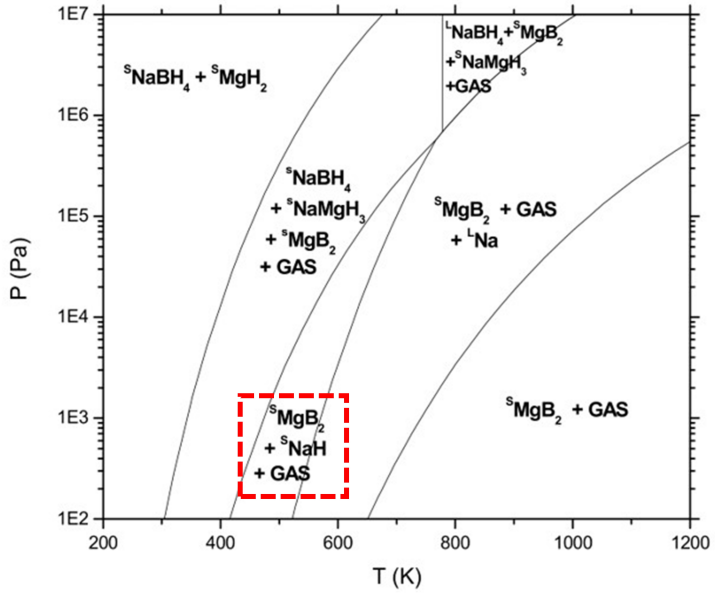

Figure 2.5.: The phase diagram of $NaBH_4$-MgH_2 with the highlighted state of interest. Figure courtesy [96].

Like the $LiBH_4$-MgH_2 system, it was proposed by Czujko *et al.* [97] that the $NaBH_4$-MgH_2 also undergoes a two-step dehydrogenation reaction (as indicated in Reaction 7), yielding a high theoretical hydrogen storage capacity of 7.8 wt%. The addition of MgH_2 serves to effectively lower the corresponding enthalpy of reaction ΔH to approximately 62 kJ/mol. Accordingly, the theoretical decomposition temperature was predicted to be 350 °C for $NaBH_4$-MgH_2 under atmospheric pressure [98, 99]. This can also be illustrated by the phase diagram of $NaBH_4$-MgH_2 as depicted in Figure 2.5. However, in practice, a higher temperature is usually reported to process this dehydrogenation reaction due to limitations in its kinetics.

$$2\,NaBH_4 + MgH_2 \longrightarrow 2\,NaBH_4 + Mg + H_2 \longrightarrow 2\,NaH + MgB_2 + 4\,H_2 \qquad \{7\}$$

$$2\,NaBH_4 + MgH_2 \longrightarrow 2\,NaBH_4 + Mg + H_2 \longrightarrow 2\,Na + MgB_2 + 5\,H_2 \qquad \{8\}$$

The thermal programmed desorption measurements conducted under static vacuum by Garroni et al. [98] showed that the dehydrogenation of MgH_2 started at around 330 °C, releasing approximately 1.8 wt% H_2, signaling full decomposition of MgH_2. As the temperature was increased to 450 °C, the reaction between $NaBH_4$ and Mg progressed slowly to complete, yielding a total hydrogen release of 9.0 wt%, which surpasses the theoretical hydrogen storage capacity of 7.8 wt% for Reaction 7. As shown in Figure 2.5, under these conditions, the decomposition of NaH is thermodynamically allowed. This excess hydrogen release thus can be attributed to the decomposition of NaH into Na and H_2 (as outlined in Reaction 8), which negatively affects the reversibility of the $NaBH_4$-MgH_2 system under the given temperature and pressure conditions for the hydrogenation process.

2.4. Kinetics of Hydride Formation and Decomposition

As previously noted, both $LiBH_4$-MgH_2 and $NaBH_4$-MgH_2 face challenges in releasing hydrogen at the desired temperature due to their slow kinetics. This section thus focuses on the fundamental principles of kinetics and the strategies to enhance kinetics in hydrogen storage materials.

2.4.1. Fundamentals of Kinetics

The overall reaction rate, represented by $\frac{d\alpha}{dt}$, in the sorption process for hydrogen storage materials is influenced by several factors, including temperature, pressure, and morphological changes occurring during (de)hydrogenation. Here, α denotes the fraction of hydrogen released, and t represents the elapsed reaction time. This overall reaction rate can be further expressed by Equation 2.2, where the reaction rate constant k is dependent on both temperature and pressure. The function $G(\alpha)$ encapsulates the intrinsic characteristics of the solid, encompassing factors such as defects, crystalline structure, and morphology [100, 101].

$$\frac{d\alpha}{dt} = k \cdot G(\alpha) \tag{2.2}$$

Equation 2.2 can also be rewritten as Equation 2.3, where $g(\alpha)$ is the integral form of gas-solid kinetic models, linking to the kinetic models shown in Table 2.3. This is also equivalent to the product of the reaction rate constant and time.

$$g(\alpha) = \int_0^{\alpha} \frac{d\alpha}{G(\alpha)} = k \cdot t, \tag{2.3}$$

The commonly used gas-solid kinetic models that describe the physical behavior of hydrogen storage materials can be broadly classified into three categories: nucleation and growth models, geometrical contraction models, and diffusion models. Table 2.3 provides an overview of the most commonly used kinetic models that describe the phase transformation of hydrogen storage materials. Geometrical contraction models are based on the assumption that the dehydrogenation and hydrogenation processes take place uniformly either outward or inward from the surface of the materials, with the shape or geometry of the materials, such as cylinder and ball, being the most critical factor. As a result, these models must be adapted accordingly to account for changes in the material's dimensionality [102]. The contracting volume (CV) model under this category is considered simple and relatively accurate, as it does not make any additional assumptions [103].

The diffusion models are typically applicable for diffusion-controlled reactions, with the diffusion process considered as the rate-limiting step for phase transformations [105]. Representative models in this category are based on the Jander [107] and Ginstling-Brounshtein (G-B) [108] equations, which are expressed in 2D and 3D forms, respectively, in Table 2.3.

The Johnson-Mehl-Avrami-Kolmogorov (JMAK) models are generally considered for depicting the phase transformation of hydrogen storage materials during (de)hydrogenation, encompassing the information about nucleation and growth [104]. For nucleation, two possible nucleation modes exist for the case of isothermal annealing: site-saturated and constant nucleation rate. The site-saturated mode assumes that all nucleation sites are exhausted in the early stage of phase transformations, and no additional nucleation sites will appear afterwards. On the other hand, the constant nucleation rate mode describes the continuous appearance of nucleation sites at a constant rate during phase transformations. As a result of these two different nucleation scenarios, the JMAK model has two original expressions, see Equations 2.4 and 2.5, respectively [109].

$$\alpha = 1 - \exp\left[-N_0 G_0^{\frac{d}{m}} \exp\left(\frac{-\frac{d}{m}\Delta E_{\mathrm{g}}}{RT}\right) t^{\frac{d}{m}}\right] \tag{2.4}$$

$$\alpha = 1 - \exp\left[-I_0 G_0^{\frac{d}{m}} \frac{1}{1+\frac{d}{m}} \exp\left(\frac{-\Delta E_{\mathrm{n}} - \frac{d}{m}\Delta E_{\mathrm{g}}}{RT}\right) t^{1+\frac{d}{m}}\right] \tag{2.5}$$

Table 2.3.: The frequently used kinetic models to describe the phase transformation of hydrogen storage materials, with α being the fraction of hydrogen released and n being the Avrami exponent [74, 104, 105, 106].

Kinetic Model	$g(\alpha) = k \times t =$
nucleation and growth model	
Johnson-Mehl-Avrami-Kolmogorov (JMAK)	$[-\ln(1-\alpha)]^{1/n}$; n - Avrami exponent
geometrical contraction model	
Two-dimensional growth of contracting volume (2D CV)	$1-(1-\alpha)^{1/2}$
Three-dimensional growth of contracting volume (3D CV)	$1-(1-\alpha)^{1/3}$
diffusion model	
Two-dimensional diffusion of Ginstling-Brounshtein equation (2D G-B)	$[(1-\alpha)\ln(1-\alpha)]+\alpha$
Three-dimensional diffusion of Ginstling-Brounshtein equation (3D G-B)	$1-\frac{2}{3}\alpha-(1-\alpha)^{2/3}$
Two-dimensional diffusion of Jander equation (2D Jander)	$(1-(1-\alpha)^{1/2})^2$
Three-dimensional diffusion of Jander equation (3D Jander)	$(1-(1-\alpha)^{1/3})^2$

In the above equations, N_0 denotes the number of nuclei, G_0 represents the intrinsic growth rate, d is the dimensionality of growth, m is the growth mode parameter ($m = 1$ corresponds to interface-controlled growth and $m = 2$ corresponds to diffusion-controlled growth). In interface-controlled growth, the phase transformation is primarily controlled by the growth of interfaces or boundaries between the parent phase and the newly forming phase. In diffusion-controlled growth, the phase transformation is controlled by the diffusion of atoms or molecules through the parent phase to the growth front of the new phase. ΔE_{g} is the activation energy of growth, ΔE_{n} is the activation energy of nucleation, and I_0 is the intrinsic nucleation rate constant.

By simplifying both Equation 2.4 and 2.5, we can obtain Equation 2.6, which is equivalent to the corresponding equation listed in Table 2.3.

$$\alpha = 1 - \exp\left(-kt^n\right) \tag{2.6}$$

The Avrami exponent, represented by n, serves as a crucial parameter in characterizing the kinetics of the phase transformation in hydrogen storage materials. It provides information on

the nucleation mode, the dimensionality of growth, and the growth mode, thereby serving as an important tool for understanding and optimizing the behavior of these materials [104, 109, 110]. To determine the Avrami exponent n, Equation 2.6 can be rewritten as Equation 2.7.

$$\ln[-\ln(1-\alpha)] = \mathrm{n}\ln(\mathrm{t}) + \mathrm{n}\ln(\mathrm{k}) \tag{2.7}$$

By plotting $\ln[-\ln(1-\alpha)]$ against $\ln(\mathrm{t})$ according to Equation 2.7, the Avrami exponent n can be immediately determined by the slope of the straight lines.

2.4.2. Strategies for Kinetic Improvement

To enhance the performance of hydrogen storage materials, several effective methods are currently being extensively researched, including nanostructuring through mechanical milling, nanoconfinement through the use of carbon scaffolds, and the addition of certain additives.

2.4.2.1. Nanostructuring

It is widely recognized that the properties of materials, including thermal, optical, mechanical, and magnetic properties, can significantly change when the size of the material reaches the nanoscale regime. A classic example is gold, which appears as a shiny, yellow metal in its bulk form, but turns red by absorbing green light when its particle size is smaller than 10 nm. Furthermore, the melting point of 2.5 nm gold particles is about 930 K, compared to its bulk value of 1336 K [111]. As the size decreases, a significant amount of magnetism also emerges [112]. These differences that result from changes in material size are generally attributed to the surface effect and to the quantum size effect [113].

A typical method for reducing the particle size of materials to the nanoscale regime is ball milling, as depicted in Figure 2.6, which has been shown to considerably enhance the sorption kinetics of hydrogen storage materials [21, 22, 115]. The improvement in kinetics is attributed to the prominent role played by surface contributions, defect contributions, and induced mechanical stress in altering the thermodynamics and kinetics of the metal-hydrogen systems.

The size effect also plays a crucial role in the hydrogen storage properties of materials [116, 117]. Research by Pundt *et al.* [57, 118] has shown that in small-sized metal-hydrogen (M-H) systems, hydrogen solubility is significantly different from that in bulk systems, leading to alterations in thermodynamics and kinetics during hydrogenation and dehydrogenation. They identified that surface contributions, such as the loss of symmetry for surface atoms, and defect

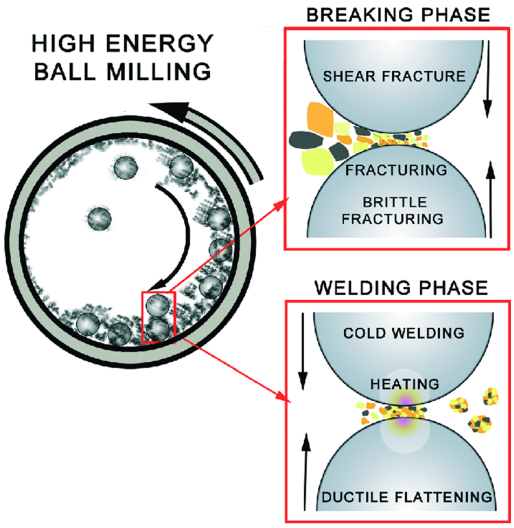

Figure 2.6.: Schematic illustration of ball milling. Figure courtesy [114].

contributions, such as dislocations, grain boundaries, and phase boundaries that facilitate hydrogen diffusion, play dominant roles in affecting the hydrogen storage properties of the systems. Additionally, induced mechanical stress also contributes to these effects.

2.4.2.2. Nanoconfinement

The technique of nanoconfinement has also proven to be effective in enhancing the sorption kinetics of hydrogen storage materials [23, 24, 119]. This approach typically involves using lightweight scaffold hosts, such as nanoscale carbon-based materials, which provide large surface areas and porosity to accommodate high loading of active materials. The improvement in kinetics is achieved by limiting the movement of the active materials within the pores [120], thus reducing the diffusion distance of the materials and increasing the reaction frequency. Additionally, nanoconfinement protects the materials from agglomeration during (de)hydrogenation, thereby improving the cyclability and reversibility of the hydrogen storage materials. Furthermore, this technique also provides benefits in terms of heat transport and mechanical stability. Nevertheless, the decrease in the volumetric density of hydrogen caused by the application of scaffold hosts should be taken into account for the hydrogen storage materials.

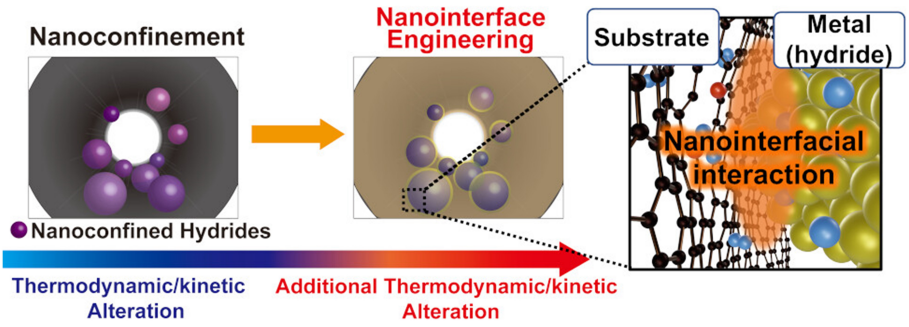

Figure 2.7.: Schematic illustration of nanoconfinement. Figure courtesy [121].

2.4.2.3. Additive

Additives are commonly used to enhance the kinetics of hydrogen uptake and release in hydrogen storage materials [122, 123]. One such example is the use of palladium (Pd) which is known to be one of the most effective additives. Pd can facilitate the dissociation of hydrogen molecules into atoms and also has low activation energy required for hydrogen diffusion, resulting in fast kinetics of hydrogen uptake and release. Zaluska *et al.* [116] reported that the hydrogen absorption kinetics in nanocrystalline magnesium with Pd as an additive was three times faster compared to without Pd.

For reactive hydride composites like $LiBH_4$-MgH_2 or $NaBH_4$-MgH_2, transition metal additives have been reported to play a crucial role in enhancing the kinetics. It was proposed by Bösenberg *et al.* [27] that transition metal borides, generated from the original transition metal additives, may act as heterogeneous nucleation sites that accelerate the formation of MgB_2. The additive selected for this study was $3TiCl_3 \cdot AlCl_3$ [28], chosen for its established capability to significantly enhance the dehydrogenation kinetics of $LiBH_4$-MgH_2 as well as its cost-effectiveness. It was suggested that the lattice misfit between transition metal borides and MgB_2 plays a dominant role in accelerating the heterogeneous nucleation. This idea is addressed in the present thesis.

2.4.3. Edge-to-Edge Matching Model

Given the importance of the lattice misfit, the edge-to-edge matching model proposed by Zhang and Kelly [124, 125, 126, 127] is applied for determining the lattice misfit between two phases. This model is based on the minimization of energy at the interfaces between the two phases and predicts the occurrence of heterogeneous nucleation based on their interatomic and interplanar

misfits, see Figure 2.8a. By considering the formation of phase A on phase B, the misfit along a particular crystalline direction can be calculated using Equation 2.8, which represents the difference between the d-spacings or lattice constants of the two phases. The model has been widely adopted in the field of materials science and has provided valuable insights into the heterogeneous nucleation process and the related lattice misfit between phases.

$$\text{misfit} = \frac{d_{\mathrm{B}} - d_{\mathrm{A}}}{d_{\mathrm{A}}} \tag{2.8}$$

The interatomic misfit between two phases is usually calculated using the lattice constants along the matching directions, $[u\,v\,w]_{\mathrm{A}}$ and $[u\,v\,w]_{\mathrm{B}}$, as shown in Figure 2.8b. The matching directions are chosen based on the linear atomic density and should correspond to close or nearly close-packed directions. The interplanar misfit, in terms of d-spacings, is determined between matching planes $(h\,k\,l)_{\mathrm{A}}$ and $(h\,k\,l)_{\mathrm{B}}$, which are also selected from close or nearly close-packed planes.

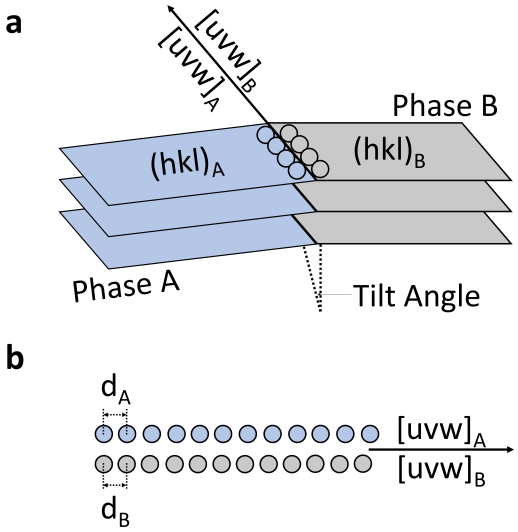

Figure 2.8.: (a) Schematic illustration of edge-to-edge matching model with phase A and phase B. The interatomic misfit is calculated with respect to $[u\,v\,w]_{\mathrm{A}}$, and $[u\,v\,w]_{\mathrm{B}}$. The interplanar misfit is determined based on the d-spacings of $(h\,k\,l)_{\mathrm{A}}$ and $(h\,k\,l)_{\mathrm{B}}$. The small tilt angle is for the refinement of the matching between the two phases; (b) Schematic illustration of interatomic misfit between phase A and b. The figure is modified from [124, 126].

As a general guideline, the interatomic misfit and the interplanar misfit between two phases should not exceed 10% and 6%, according to critical values established in the literature statistically [124]. On the other hand, minimizing the interatomic misfit is of higher priority from an energetic

perspective, even if the d-value misfit exceeds 6%. In such cases, the misfit can be refined by rotating the two phases about their matching directions [126]. The misfit between phases will be determined for the materials studied in this work in order to establish their crystalline orientation relationships.

3. Transmission Electron Microscopy

Due to a lack of sufficient knowledge regarding the relevant properties of reactive hydride composites at a nanoscale level, transmission electron microscopy (TEM) is considered as a versatile and effective solution for conducting nanoscale investigations. Therefore, understanding the fundamentals of the TEM techniques employed in this study is essential. The basics of a TEM system is introduced in Section 3.1, including the interaction between the electron beam and specimen, on which various TEM techniques are based. Electron diffraction is also an important tool especially in providing crystallographic information about materials, and the theory behind its experimental analysis is shortly described in Section 3.2. Conventional TEM, scanning TEM (STEM), and high-resolution TEM (HRTEM) are presented in Section 3.3 as intuitive ways to gather information about materials through their contrast. Energy-dispersive X-ray spectroscopy (EDXS) and electron energy loss spectroscopy (EELS) are widely used analytical electron microscopy methods in this work that provide insights into the material's chemistry, see Section 3.4. Finally, Section 3.5 presents electron tomography, which provides a three-dimensional view of the target material, helping to resolve ambiguities arising in 2D space.

3.1. Fundamentals of TEM

A transmission electron microscope consists of three main components: the illumination system, the objective system, and the imaging system, as shown in Figure 3.1. The illumination system is primarily composed of the electron source and the condenser lenses. The electron gun is the most critical component of the illumination system as it determines the coherence (temporal and spatial) of the electrons, which in turn affects the image resolution. Both TEMs Themis-Z and Themis-300 used in this study are equipped with field-emission guns (FEGs), which can generate a strong electrostatic field at the sharp tip of the gun to produce ultra-high energy electrons with good coherence and high brightness.

In a TEM column, the electron beam is manipulated using electromagnetic lenses. The illumination system consists of three condenser lenses, namely C1, C2, and C3, collaborating to regulate the electron beam. The C1 lens governs the spot size, determining the quantity of electrons

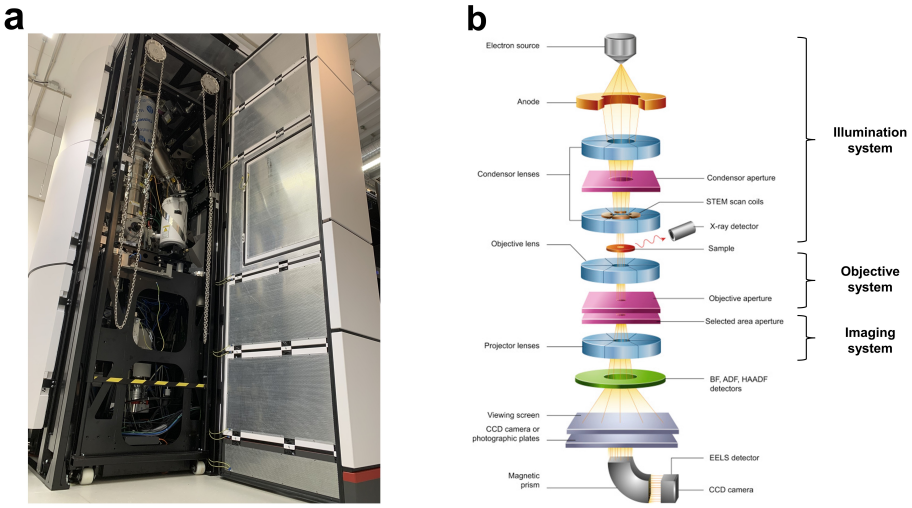

Figure 3.1.: (a) Transmission electron microscope Themis-Z 60-300 (Thermo Fisher Scientific Inc., USA) equipped with a monochromator and double aberration correctors (probe and image Cs correctors), located in INT at KIT; (b) The schematic diagram of TEM systems. The figure is modified from [128].

passing through the condenser aperture and influencing the intensity of the electron beam. The combination of C2 and C3 lens is essentially responsible for controlling the illumination area and the convergence angle of the electron beam. Positioned within the objective system, the objective lens is a crucial component for determining resolution by regulating image focus through the adjustment of its strength.

In the imaging system, the uppermost lens is known as the intermediate lens. By changing the intensity of the intermediate lens, one can switch between the diffraction mode and the imaging mode. The lenses below intermediate lens are known as the projection lenses. One can get the access to control the magnification for TEM images and the camera length for the diffraction patterns by tuning the intensity of the projection lenses. Furthermore, various cameras and detectors are accessible in TEM to collect different signals upon the beam-specimen interaction.

The TEM techniques applied in this work rely on various kinds of the interaction between the electron beam and a specimen. When the electron beam interacts with a specimen, the electrons are scattered by the specimen. This scattering process can be viewed as a series of particle interactions due to the wave-particle duality of electrons. The electrons that are scattered in a specific manner carry information about the internal structure and chemistry of the specimen. This makes electron scattering a fundamental aspect of all electron microscopy techniques.

In terms of the direction of electron scattering, it can be classified into forward scattered and back scattered electrons. Back scattered electrons are mainly used for imaging in scanning

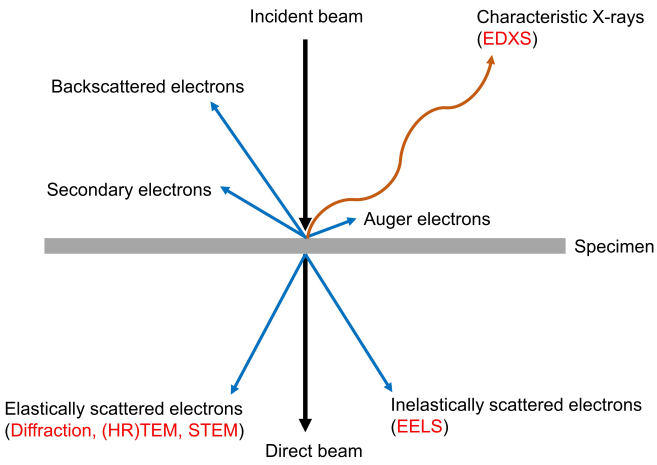

Figure 3.2.: Interaction between the incident electron beam and material results in different kinds of electron scattering and also other signals like X-rays. The related techniques applied in this work are highlighted in red.

electron microscopy (SEM) and will not be discussed in this work. On the other hand, forward scattered electrons that are transmitted through the specimen to form an image are of great interest in TEM. In addition to the scattering direction, elastic/inelastic and coherent/incoherent scattering need to be differentiated. Coherent scattering refers to a situation where there is no relative phase change between the scattered wavelets of electrons, while incoherent scattering is the opposite. Elastic and inelastic scattering describe whether scattering results in measurable energy loss or not, respectively. Furthermore, inelastic scattered electrons are always incoherent. The various forms of electron scattering and other signals generated by the beam-specimen interaction are illustrated in Figure 3.2. Additionally, the electron scattering can also describe the number of scattering events that occur within the specimen. It can be broadly divided into single scattering and multiple scattering, which is related to the probability of electron scattering as it passes near an atom.

3.2. Electron Diffraction

Electron diffraction is a powerful technique for determining the structural information of materials and is also frequently used in this work [129]. For crystalline materials, the diffraction pattern can be used to characterize their crystallographic properties, including the lattice parameters, space-group symmetry, and crystal identity. On the other hand, for amorphous materials, the

radial distribution function (RDF) can be applied to extract structural information such as the atomic spacing between bonded atoms [130].

$$n\lambda = 2d_{\mathrm{hkl}} \sin(\theta_B) \tag{3.1}$$

Bragg's law is a fundamental theory used to determine the angle of coherent scattering of waves from a crystal when constructive interference occurs, as described in Equation 3.1 [131]. When two parallel incident electron beams are scattered from two adjacent lattice planes of $(h\,k\,l)$, the path difference equals $2d_{\mathrm{hkl}} \sin(\theta_B)$, where θ_B is the scattering semi-angle of electrons and d_{hkl} is the d-spacing of plane $(h\,k\,l)$ when the Bragg condition is met. This means the scattered electron beams create constructive interference at θ_B. The path difference is required to be $n\lambda$, where n is an integer and λ refers to the wavelength of electrons, by definition. When considering the scattered-electron intensity in images and diffraction patterns, the atomic scattering factor is of great importance. It relies on the electron wavelength λ, the atomic number Z, and the scattering angle θ. In general, the atomic scattering factor decreases with smaller values of λ and Z, as well as larger values of θ. This work specifically focuses on light elements, namely H, Li, and B. Consequently, the scattered-electron intensity of the related materials, such as $\mathrm{LiBH_4}$ and LiH, is expected to be low in diffraction patterns. More details regarding electron diffraction can be obtained by reading [132, pg. 257].

3.3. Electron Imaging

Electron imaging is essential for this work, relying on the difference in intensity between adjacent regions, which is defined as image contrast. As the incident electron waves pass through the specimen, changes in their amplitude and phase affect image contrast. Two fundamental categories of image contrast are amplitude contrast and phase contrast. Amplitude contrast can be further classified into mass-thickness contrast and diffraction contrast. This section introduces mass-thickness contrast for TEM, Z-contrast for STEM based on incoherent elastic scattering, and phase contrast based on coherent elastic scattering for high-resolution TEM, all of which have been applied in this study.

3.3.1. TEM: Mass-Thickness Contrast

Electron microscopy employs two basic methods for forming amplitude-contrast images, namely bright-field (BF) and dark-field (DF) imaging [132]. The choice between these two methods depends on the selection of electrons by the objective aperture, which can either collect the

unscattered direct beam for BF imaging or only the scattered electrons for DF imaging. When the incident electron beam illuminates an area with a larger atomic number or a larger thickness, more electrons tend to be scattered, resulting in a darker appearance of the sample in BF imaging. In contrast, in DF imaging, the scattered electrons are used to form the image, resulting in a brighter appearance of the sample. To create sufficient mass-thickness contrast in an image, it is important to select the appropriate electrons.

3.3.2. STEM: Z-Contrast

Scanning transmission electron microscopy (STEM) uses a converged electron beam to scan the region of interest and create an image, and the resolution is determined by the size of the probe. The probe size can be significantly improved by using an aberration-corrected probe corrector. Unlike in transmission electron microscopy (TEM), where a single camera is used to acquire both bright-field (BF) and dark-field (DF) images, STEM has a set of annular detectors that capture electrons scattered at varying angles [133]:

- Bright-field (BF) detector: captures unscattered electrons
- Annular dark-field (ADF) detector: captures scattered electrons
- High-angle annular dark-field (HAADF) detector: captures electrons scattered at high angles

Similar to TEM, the intensity distribution in STEM BF images is influenced by both mass-thickness contrast and diffraction contrast. The ADF detector collects medium-angle scattered electrons, whereas the HAADF detector primarily collects large-angle scattered electrons. The utilization of a HAADF detector effectively avoids diffraction contrast arising from Bragg diffractions. This technique is also known as Z-contrast imaging, representing the variation in the atomic number (Z) of materials. Therefore, Z-contrast imaging facilitates the acquisition of atomic resolution of materials' geometric structure and reflects their elemental compositions to a certain extent.

Another powerful technique based on STEM and also performed in this work is 4D-STEM, which is in combination with electron diffraction. Regarding 4D-STEM, Simultaneous capturing of 2D diffraction patterns is achieved as a specimen is scanned by an electron probe in a 2D array, for each scanning pixel. This results in a 4-dimensional dataset that can provide information about the material's structure, composition, and 3D defect crystallography through virtual imaging, orientation mapping, strain mapping, and more [134]. Compared to parallel electron beams, convergent beams are used to acquire the diffraction pattern, which is related to the convergent angle of the probe.

3.3.3. HRTEM: Phase Contrast

A phase change occurs in the electron wave due to the electrostatic potential of the specimen when an electron traverses the specimen. The phase contrast in HRTEM images arises from the interference caused by electron waves with varied phases in the image plane [135, 136, 137, 138, 139, 140]. It is important to note that although both the phase and amplitude of an electron wave contain structural information of the specimen, only the amplitude can be recorded in reality. Fine-tuning the aberrations of a microscope, such as defocus, is thus required to convert the phase of the electron wave into amplitudes for gaining access to the structural information held in the electron wave's phase. The contribution made by the amplitudes obtained from the phase changes of diffracted electron waves to the HRTEM image is described by the phase-contrast transfer function (PCTF), see Equation 3.2.

$$\sin(\chi(\mathbf{q})) = \sin(\frac{1}{2}\pi C_{\mathrm{s}}\lambda^3\mathbf{q}^4 + \pi\lambda\Delta f\mathbf{q}^2) \tag{3.2}$$

In the equation, $\mathbf{q}$ denotes the spatial frequency, C_{s} denotes the spherical aberration coefficient, and Δf represents defocus. Given certain values of defocus and the spherical aberration coefficient, the PCTF changes with the spatial frequency.

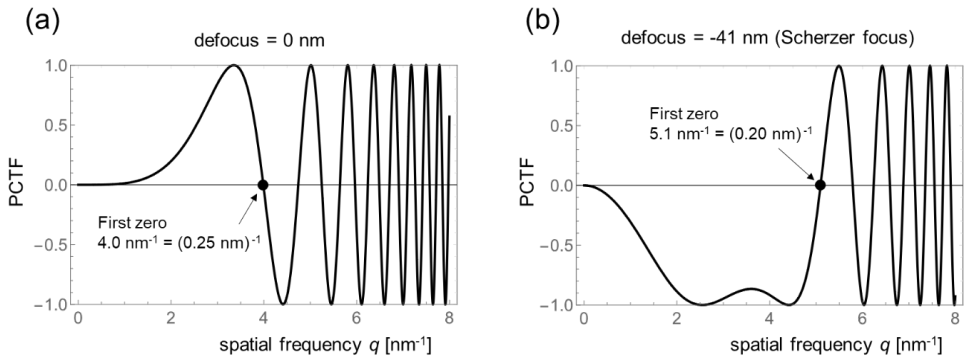

Figure 3.3.: Phase-contrast transfer function with an accelerating voltage of 200kV and C_s of 0.5 mm given defocus of 0 nm for (a) and defocus of -41 nm for (b). Figure courtesy [141].

Figure 3.3 presents the PCTF at two distinct defocus settings: 0 nm and the Scherzer focus df_{Sch}. The Scherzer focus [142, 143] is suggested as a suitable choice of defocus, which leads to a broad band of phase contrast transfer with zero crossing up to a relatively high spatial frequency, compared to other focus conditions. Up to this spatial frequency, the TEM phase contrast image can be regarded as a faithful representation of the projected potential in a thin specimen. The

Scherzer focus can be practically defined by the corresponding PCTF containing a local minimum ($= \sin(-2/3\pi)$), and it is formulated in Equation 3.3. The reciprocal of the spatial resolution at the first zero cross of PCTF under Scherzer focus condition is defined as point resolution d_{Sch}, which gives $d_{\mathrm{Sch}} = 0.66 \left(C_S \lambda^3\right)^{\frac{1}{4}}$.

$$df_{\mathrm{Sch}} = -\sqrt{\frac{4}{3} C_S \lambda} \tag{3.3}$$

Beyond the point resolution, the structural information can still be transferred but is intensively modulated by the phase shift and damped by an envelope function [144], which describes the effect of spatial and temporal coherence, due to chromatic aberration of the objective lens, the converged electron beam, etc., on the information transfer. The spatial frequency, at which the amplitude of the envelope function effectively diminishes to e^{-2}, is defined as the information limit, serving as another indicator of resolution. In this work, the crystal structure of the investigated materials was also studied using HRTEM to gain insights. More details regarding HRTEM can be obtained by reading [137].

3.4. Analytical Electron Microscopy

EDXS and EELS are widely used spectroscopic methods in TEM for elemental analysis and chemical characterization. The fundamental principle underlying these methods is the unique electronic structure of each element, resulting in a characteristic electromagnetic emission spectrum. By analyzing the characteristic energy lost from the incident electron beam or the characteristic X-rays generated during an inelastic beam-specimen interaction, it is possible to identify the elements present in the specimen.

3.4.1. Energy-Dispersive X-ray Spectroscopy (EDXS)

The interaction between the incident electron beam and a specimen creates a core hole by activating a core electron, which is then refilled by an electron from an outer, higher-energy shell. This process releases energy in the form of X-rays [145]. The analysis of the emitted characteristic X-rays from a specimen is known as Energy-Dispersive X-ray Spectroscopy (EDXS) [146].

Combining with STEM, spectrum imaging (SI) can be used to acquire a data cube storing detailed spatial and spectroscopy information, including EDXS and EELS, as illustrated in Figure 3.4. Similar to 4D-STEM, spectra are recorded simultaneously for each pixel as the STEM probe

is rastered on the specimen. This enables the extraction of typical elemental information and the creation of corresponding quantitative images, which are also relevant for this work.

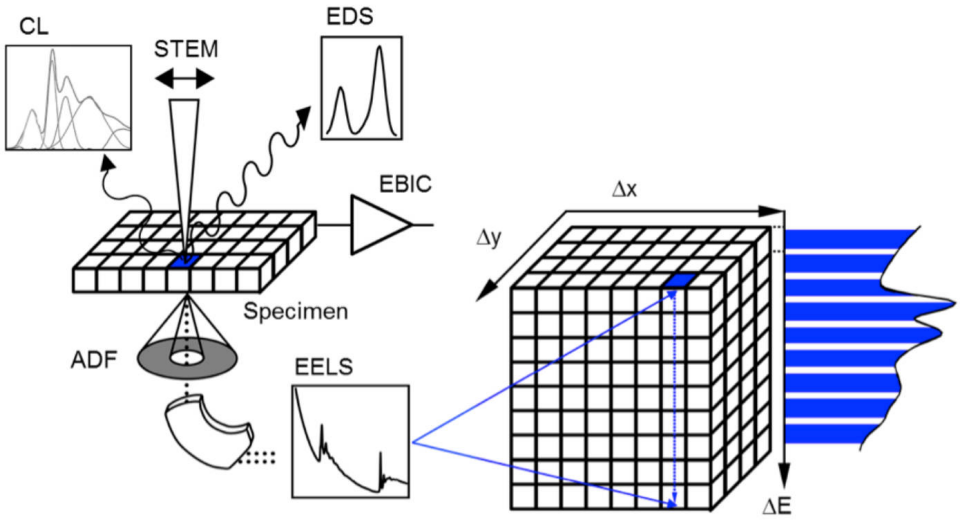

Figure 3.4.: Schematic Illustration of STEM spectrum imaging. The EDXS and EELS spectra are acquired as the STEM probe is systematically rastered on a specimen, collecting a data cube storing both spatial and spectroscopy information. Figure courtesy [147].

Quantitative X-ray analysis is based on the Cliff-Lorimer technique [148, 149], as shown in Equation 3.4.

$$\frac{C_{\mathrm{A}}}{C_{\mathrm{B}}} = k_{\mathrm{AB}} \frac{I_{\mathrm{A}}}{I_{\mathrm{B}}} \tag{3.4}$$

The equation given shows that the concentration ratio of elements A and B in a specimen is proportional to the ratio of the measured X-ray intensities, with the proportionality constant being the Cliff-Lorimer factor k_{AB}, which depends on the atomic number, absorption, and fluorescence of X-rays within the specimen [132]. The weight percentages of elements A and B in the specimen are denoted by c_{A} and c_{B}, respectively, while I_{A} and I_{B} represent the measured intensities of the characteristic X-rays emitted from the specimen for elements A and B.

PCA (Principal Component Analysis) is a method used to transform high-dimensional datasets into a more manageable yet still informative form. This is achieved by identifying the principal components, which are linear combinations of the original variables that capture the maximum variance in the data. By doing so, PCA simplifies the dataset while retaining essential information. In this study, PCA is employed to denoise the high-dimensional dataset.

Despite being extensively utilized, EDXS is subject to some practical limitations. Due to the low energy of X-rays emitted by light elements, there is a high probability of X-ray absorption within the sample, making these X-rays undetectable by detectors. Consequently, it is generally not recommended to determine light elements (atomic number Z < 6) using EDXS. The elements H, Li, and B in the materials $LiBH_4$-MgH_2 and $NaBH_4$-MgH_2 studied in this work thus cannot be detected and analyzed by EDXS as a result. Therefore, the inclusion of EELS is necessary for this study. More details regarding EDXS can be obtained by reading [132, pg. 639].

3.4.2. Electron Energy Loss Spectroscopy (EELS)

The analysis of the energy distribution of electrons that have passed through a specimen is known as electron energy-loss spectroscopy (EELS). During this process, the electrons may have experienced either no energy loss or inelastic collisions, typically of electron-electron nature, see Figure 3.4. The observable edges in an EELS spectrum directly relate to the electron shells of an atom, delivering a lot of details on material chemistry and electronic structure, including band gap, dielectric properties, and bonding state. EELS offers excellent energy resolution, typically down to 1 eV and can be even close to 0.1 eV using an electron-beam monochromator. Although EELS is theoretically capable of detecting light elements like H, Li, and B, it usually requires a thinner specimen compared to EDXS, limiting its practical applications in some cases.

An EELS spectrum comprises two main regions: the low-loss region (<50 eV) and the core-loss region (>50 eV), as illustrated in Figure 3.5. The most prominent feature in the low-loss region is the intense zero-loss peak, primarily created by forward-scattered electrons with no energy loss, and quasi-elastically scattered electrons with minimal energy loss. Subsequent to the zero-loss peak, plasmon region becomes apparent, arising from the excitation of multiple bulk and surface plasmons within the sample. These plasmons are generated by the oscillation of the loosely bound electrons in the sample. Additionally, peaks representing plural scattering are significant. They can be utilized to eliminate the background resulting from plural scattering and recover the single scattering distribution through deconvolution, particularly beneficial for EELS elemental quantification [151].

In a core-loss spectrum, the features of interest are called an edge, as shown in Figure 3.5. An atom can be ionized when the transferred energy is above the critical ionization energy of a certain orbital. The ionization cross section reaches its maximum value when the transferred energy is exactly equal to the critical ionization energy. The ionization-loss electrons therefore show an energy distribution, where the probability is highest at the critical ionization energy and decreases slowly as the transferred energy exceeds the critical value [132, pg. 715-721].

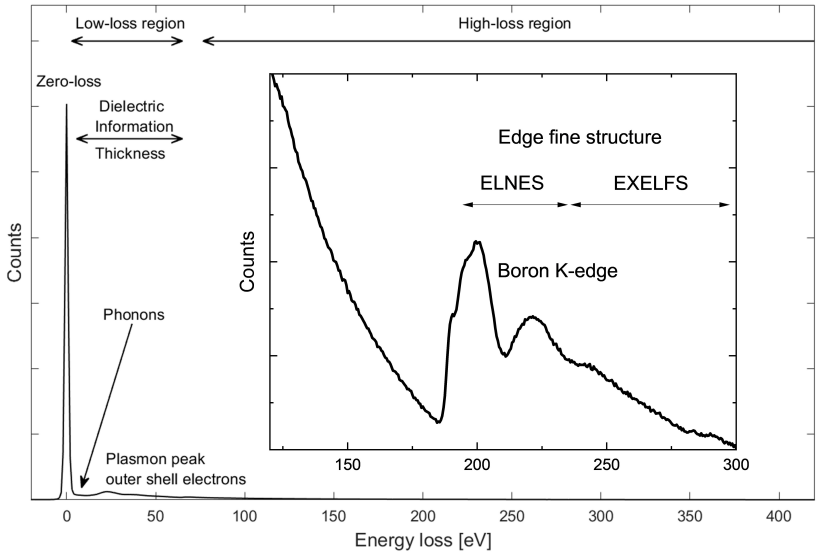

Figure 3.5.: An example of an EELS spectrum presents an overview of the different excitation sources including the zero loss peak and the plasmon peak in low-loss region, and the ionization edges with the fine structures in core-loss region. Figure courtesy [150].

The background modeling for EELS elemental mapping is illustrated in Figure 3.6. Typically, a background fit window Γ is selected with a width of 10-20% of the edge onset energy E_{k}. The background model is then fit, extrapolated, and subtracted using the power law model, which is the most commonly used background model for elemental mapping. Finally, the signal intensity I_{k} is obtained by subtracting the background intensity I_{b} using the background model, providing information on the distribution of elements.

Furthermore, given the excellent energy resolution of EELS, the fine structures around the ionization edge onset can also be resolved, as shown in Figure 3.5. These fine structures, known as energy-loss near-edge structure (ELNES) and extended energy-loss fine structure (EXELFS), reflect the energy distribution of the unfilled states above the Fermi energy. ELNES is confined to a few tens of eV past the edge onset, while EXELFS is confined to several hundred eV past the edge onset. As the density of states (DOS) is extremely sensitive to changes in the bonding or the valence state of an atom, ELNES and EXELFS can be used to study the electronic structure [153] and the nearest-neighbor atomic structure [154] of a specimen by analyzing the offset and shape of these fine structures. More details regarding EELS can be obtained by reading [132, pg. 679].

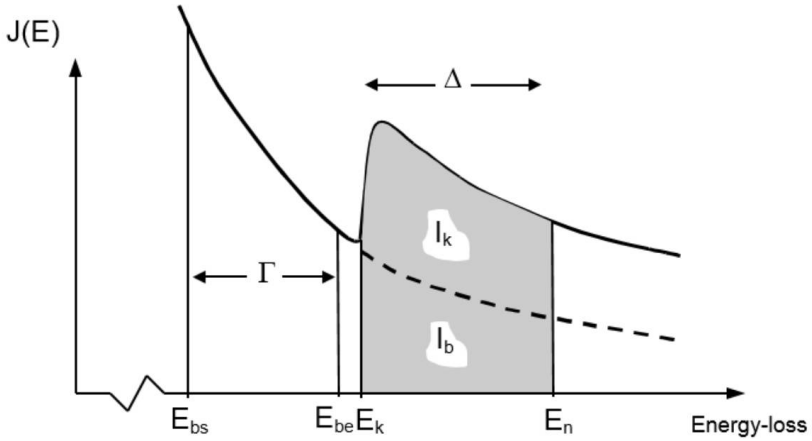

Figure 3.6.: Background modeling of EELS. Figure courtesy [152].

3.5. Electron Tomography

Although the previous sections detail a variety of TEM techniques available for material characterization, misunderstanding material characteristics may still occur as these methods are confined to a two-dimensional space. With the reconstruction of two-dimensional projections, electron tomography offers 3D structural information on materials.

The feasibility of tomographic reconstruction is supported by the mathematical concept of the Radon transform, which is expressed in Equation 3.5. In this equation, $f(x, y)$ represents a two-dimensional object with an unknown density defined in a certain Cartesian system on x and y. $L(\theta, t)$ stands for a line function that is defined in a polar coordinate system and the line is through the object f. In the scenario of tomography, the object function describes the specimen under investigation. The line function describes the relative position of a detector to the object, where θ refers to the tilt angle of the detector and t denotes the position of pixels of the detector. The Radon transform of f, $\mathcal{R}f(\theta, t)$, creates a sinogram, which is a sum of the linear projections of the object f with respect to the line L, when the detector is constantly rotating around the object and recording projections [155].

$$\mathcal{R}f(\theta, t) = \int_{L(\theta,t)} f(x, y)ds \tag{3.5}$$

It should be noted that the Radon transform has constructed the connection between a real object and its projections. Given the linear projection data, the inverse of the Radon transform can theoretically allow the reconstruction of the original object. However, practically solving such an

inverse problem is not feasible, as the number of parameters that need to be determined is much larger than the number of projections that can be practically acquired.

$$\begin{pmatrix} w_{1,1} & & w_{1,n} \\ \vdots & \cdots & \vdots \\ w_{m,1} & & w_{m,n} \end{pmatrix} \begin{pmatrix} x_1 \\ \vdots \\ x_n \end{pmatrix} = \begin{pmatrix} p_1 \\ \vdots \\ p_m \end{pmatrix} \tag{3.6}$$

$$\mathbf{X}^* = \underset{X}{arg\,min} \|\mathbf{P} - \mathbf{W}\mathbf{X}\| \tag{3.7}$$

The projection data (sinogram) $\mathbf{P} \in \mathbb{R}^m$ can be expressed as the inner product of an unknown object $\mathbf{X} \in \mathbb{R}^n$ and a projection operator $\mathbf{W} \in \mathbb{R}^{m \times n}$ with respect to a series of tilt angles, as shown in Equation 3.6. In this equation, n has a size of k^2, being the size of the reconstructed object (2D) with a dimension of $k \cdot k$. m is equal to $k \cdot h$ and stands for the size of the corresponding sinogram, with h being the number of applied tilt angles. The task then becomes solving Equation 3.6, with both $\mathbf{W}$ (determined by the applied tilt angle and the applied image dimension) and $\mathbf{P}$ (collected from the experiments) already known. However, since the number of applied projection angles h is usually much smaller than the selected dimension k for the reconstructed object, $\mathbf{W}$ is a non-invertible matrix and it is not possible to solve the equation using the inverse of $\mathbf{W}$.

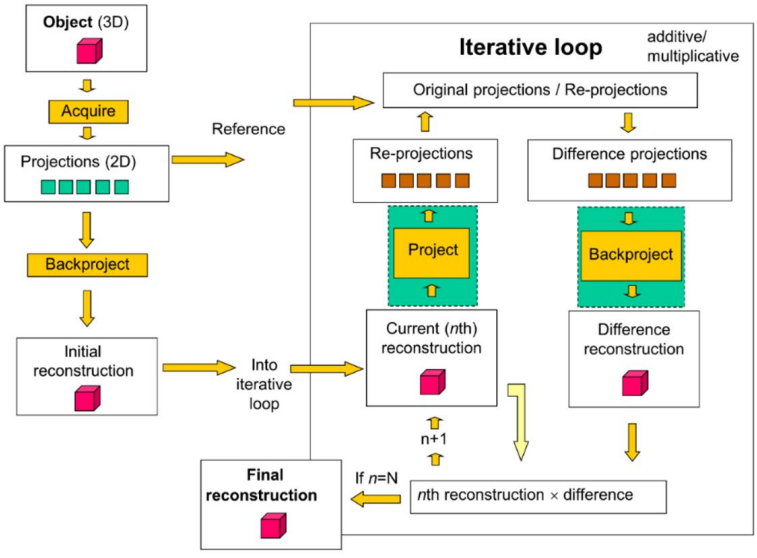

Figure 3.7.: Schematic illustration of the work flow of SIRT. Figure courtesy of P. Midgley from University of Cambridge.

To solve the tomographic reconstruction problem more efficiently, the algorithm simultaneous iterative reconstruction technique [156] is widely used, which was also applied in this work for reconstruction. Figure 3.7 illustrates the iterative process of how SIRT works [157]. In each iterative loop, the reconstructed object is used to produce a series of projections using the same tilt angles as those used in the experiment. The computed projections are then subtracted from the experimental projections to generate a series of difference projections (residuals), which are used to create a difference reconstruction by back-projection methods [158]. The (n+1)*th* reconstructed object can be acquired for the next iterative loop by multiplication (or addition) of the difference projections and the n*th* reconstructed object. The final result of reconstruction $\mathbf{X}^*$ is determined by minimizing the difference between $\mathbf{P}$ and $\mathbf{WX}$, as shown in Equation 3.7. Further experimental details about the tomography applied in this study can be found in Section 4.4.

4. Experimental

This chapter provides a detailed description of the experimental procedures for sample preparation, X-ray diffraction (XRD), kinetics measurements, and TEM-based measurements. It also covers the relevant instruments, software, and analysis methods used in these experiments. In general, the sample preparation, X-ray diffraction (XRD) measurements, and kinetics measurements were carried out at Helmholtz-Zentrum Hereon in Geesthacht, by Yuanyuan Shang. Subsequently, the materials were transported to the Institute of Nanotechnology (INT) at Karlsruhe Institute of Technology (KIT) for TEM experiments.

4.1. Preparation of RHC Systems

The powder materials used in this work were obtained from commercial companies for sample preparation. The purity levels and manufacturers of these materials are outlined in Table 4.1.

Table 4.1.: The overview of the powder materials for sample preparation in terms of purity and manufacturer.

Powder Material	Purity	Manufacturer
$LiBH_4$	95 %	Rockwood Lithium
$NaBH_4$	98 %	Sigma-Aldrich
MgH_2	95 %	Rockwood Lithium
LiH	95 %	Sigma-Aldrich
MgB_2	99 %	Alfa Aesar
$3TiCl_3 \cdot AlCl_3$	76 -78 % ($TiCl_3$)	Fisher Scientific

To achieve optimal mixing and dispersion of the powder materials, ball milling was employed for the sample preparation in this work. The sample preparation process was conducted using a Spex 8000 M Mixer Mill at room temperature and atmospheric pressure, with a total duration of 400 minutes. Stainless steel vials and balls with a diameter of 10 mm were used for the milling, with a ball-to-powder ratio of 20:1. For each sample, the stainless-steel vial was charged with 3 g of raw

materials, including additives when necessary. The starting materials are mixed according to their stoichiometric ratio of reaction, as shown in Table 4.2. The determination of the corresponding additive content is based on the mole value of the Mg-containing material, specifically either MgH_2 or MgB_2 in this study. The entire milling process including the material handling was conducted in a MBraun Unilab glovebox under a continuously purified Ar atmosphere with H_2O and O_2 levels maintained below 1 ppm.

Table 4.2.: Overview of the samples prepared for XRD, kinetics, and TEM-based measurements, including information about the starting material, the actual state and the amount of additive included in each sample.

Starting Material	Mass [g]	State	Additive Content [mol% $3TiCl_3 \cdot AlCl_3$]	Additive Mass [g]
$2LiBH_4 + MgH_2$	3	as-milled	0	0
$2LiBH_4 + MgH_2$	3	incubated desorbed@400 °C (between 1st and 2rd step)	0	0
$2LiBH_4 + MgH_2$	3	incompletely desorbed@400 °C (during 2rd step)	0	0
$2LiBH_4 + MgH_2$	3	desorbed@400 °C	0	0
$2LiBH_4 + MgH_2$	2.76	desorbed@400 °C	1	0.24
$2LiBH_4 + MgH_2$	2.11	desorbed@400 °C	5	0.89
$2LiBH_4 + MgH_2$	1.62	desorbed@400 °C	10	1.38
$2LiBH_4 + MgH_2$	1.11	desorbed@400 °C	20	1.89
$2LiBH_4 + MgH_2$	3	desorbed@420 °C	0	0
$2LiH + MgB_2$	3	as-milled	0	0
$2LiH + MgB_2$	3	10-cycled	0	0
$2NaBH_4 + MgH_2$	3	as-milled	0	0
$2NaBH_4 + MgH_2$	3	desorbed@450 °C	0	0

All the samples prepared for a series of experiments including XRD, kinetics, and TEM-based measurements, relevant to this work, are listed in Table 4.2. Varying states of $LiBH_4$-MgH_2 during the dehydrogenation process, additive $3TiCl_3 \cdot AlCl_3$ content, annealing temperature for dehydrogenation, cycling effect and varying RHC systems constitute the variables under investigation.

4.2. X-ray Diffraction (XRD)

XRD is a non-destructive technique for material characterization that relies on the constructive interference of monochromatic X-rays and the (atomic and molecular) structure of materials. Similar to electron diffraction, XRD is also based on Bragg's law. The primary difference between the two techniques is the source of radiation, X-rays with a wavelength range of 10-0.01 nm for XRD and electrons at 3.70 pm, 2.51 pm, and 1.96 pm for 100 keV, 200 keV, and 300 keV, respectively, for electron diffraction. The XRD experiments were conducted using a diffractometer (model D8 Discover, Bruker Corporation) equipped with a Cu K_α X-ray source (λ = 1.54184 Å) and a 2D VANTEC detector. The diffractometer operated at 50 kV and 1000 mA and collected diffraction patterns in the 2θ range from 10° to 90° with $\Delta 2\theta$ of 10°. Each step had an exposure time of 400 seconds. To prevent material oxidation, specimens were packed onto a sample holder and sealed with an airtight dome made of poly (methyl methacrylate) (PMMA). The entire process was conducted in a MBraun Unilab glovebox under a continuously purified Ar flow (O_2 and H_2O levels < 0.5 ppm).

In general, XRD analysis can provide a global overview of the materials present in the respective samples. Materials such as $LiBH_4$ (orthorhombic), LiH (cubic), MgH_2 (tetragonal), Mg (hexagonal), MgB_2 (hexagonal), $NaBH_4$ (cubic), NaH (cubic), and the materials related to the additive are expected to be identified. The relevant reflection parameters of these materials can be found in Appendix A. However, it is important to note that due to limited resolution, XRD analysis might not be successful in identifying materials present in small sizes.

4.3. Kinetics Measurement

The kinetics measurement is based on gas volumetry, where the gain or loss of material is determined by monitoring the change in gas pressure within a given volume. The measurements of both dehydrogenation and hydrogenation kinetics were carried out using a home-built Sievert's-type apparatus, as depicted in Figure 4.1. A stainless-steel sample holder was used in the measuring

apparatus, and the sample size used for the measurement was approximately 170 mg. The conditions consisting of temperature, pressure, and temperature rate applied to respective materials for hydrogenation and dehydrogenation are provided in Table 4.3. Volumetric changes in hydrogen release were subsequently monitored by the measurements conducted under given temperature and pressure conditions. Once each target temperature was reached, the materials were maintained under isothermal conditions until the H_2 release/uptake curve reached a plateau.

Table 4.3.: The applied conditions for the kinetics measurement for respective materials.

Reaction Type	Starting Material	Temperature [°C]	H_2 Pressure [MPa]	Temperature Rate [°C/min]
Dehydrogenation	$LiBH_4$-MgH_2	400/420	0.4	10
Hydrogenation	LiH-MgB_2	350	3	10
Dehydrogenation	$NaBH_4$-MgH_2	400/430/450	0.015	3

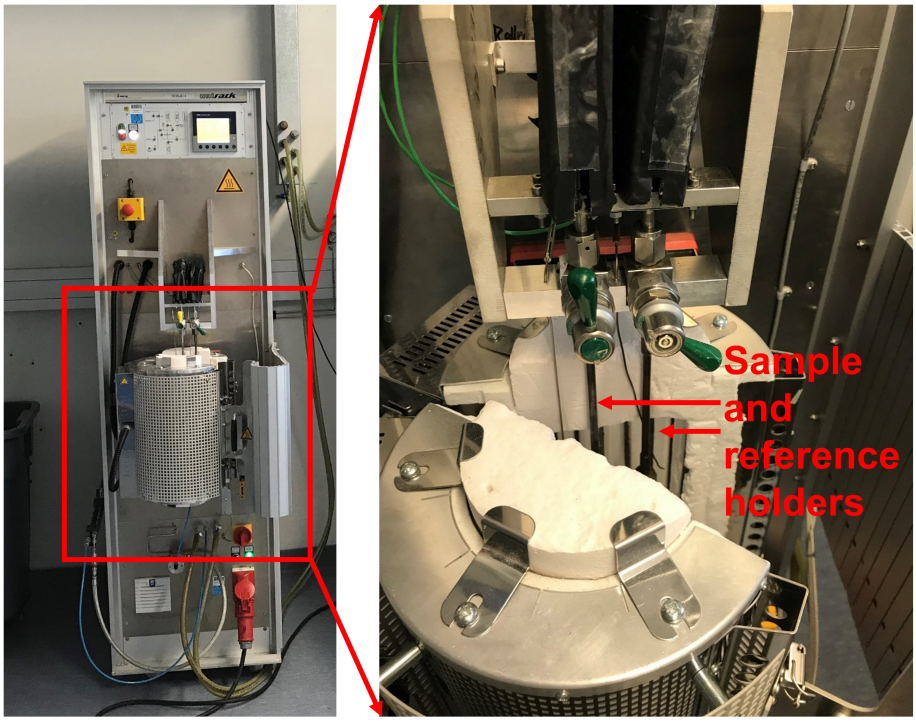

Figure 4.1.: Home-built Sievert's-type apparatus for kinetics measurement.

The hydrogen content is measured relying on a sample holder and a reference holder, as illustrated in Figure 4.1. The pressure difference between the sample and reference holders, both under identical temperature and pressure conditions and of identical design, is determined for measuring the hydrogen content. As the hydrogenation or dehydrogenation processes occur, a pressure change in the sample holder compared to that in the reference holder occurs. The hydrogen content by weight percent is then derived from the pressure difference using the ideal gas law, as shown in Equation 4.1.

$$\Delta PV = n_{H_2} RT \tag{4.1}$$

In this equation, the pressure difference between the sample holder and the reference holder is represented by ΔP. The volume of a sample holder, which varies among different sample holders, is denoted as V. R denotes the ideal gas constant, whereas T represents the actual temperature. Furthermore, the mole value of H_2, represented by n_{H_2}, is utilized to determine the hydrogen uptake/release.

4.4. Microstructural and Phase Analysis by TEM

The TEM experiments were carried out using the transmission electron microscopes Themis-Z (monochromated and aberration corrected for both STEM and TEM) and Themis-300 (aberration corrected for STEM) operated at 300 kV. These microscopes are accessible via KNMF***i***, a Helmholtz user facility. In general, the presented results of STEM tomography were acquired using Themis-300, while the rest of TEM results were acquired using Themis-Z.

Due to the air-sensitivity of the materials, TEM specimens were prepared in an argon atmosphere inside a glovebox (GS ALPHA X-Line, GS GLOVEBOX Systemtechnik) with O_2 and H_2O levels below 0.5 ppm. To prepare the TEM specimens, the ball-milled powder was dispersed in toluene and then ultra-sonicated for 1 minute before being distributed onto TEM grids. Lacey carbon-coated gold TEM grids (S166-A3-V, Plano), lacey carbon-coated copper TEM grids (S166-3, Plano), and holey carbon-coated copper TEM grids (S147-2, Plano) were used, except for experiments using the in-situ gas system, for which electronic chips (ETA-33AA-10 & EAB-33W-10, Protochips) were used.

As shown in Figure 4.2, the holders applied for this work include: a vacuum transfer holder (Model 648, AMETEK Gatan), see Figure 4.2a; an advanced tomography holder (Model 2020, E.A. Fischione Instruments), see Figure 4.2b; an in-situ heating holder (Model 2020, AMETEK Gatan), see Figure 4.2c; an environmental gas cell system (Atmosphere, Protochips), see Figure

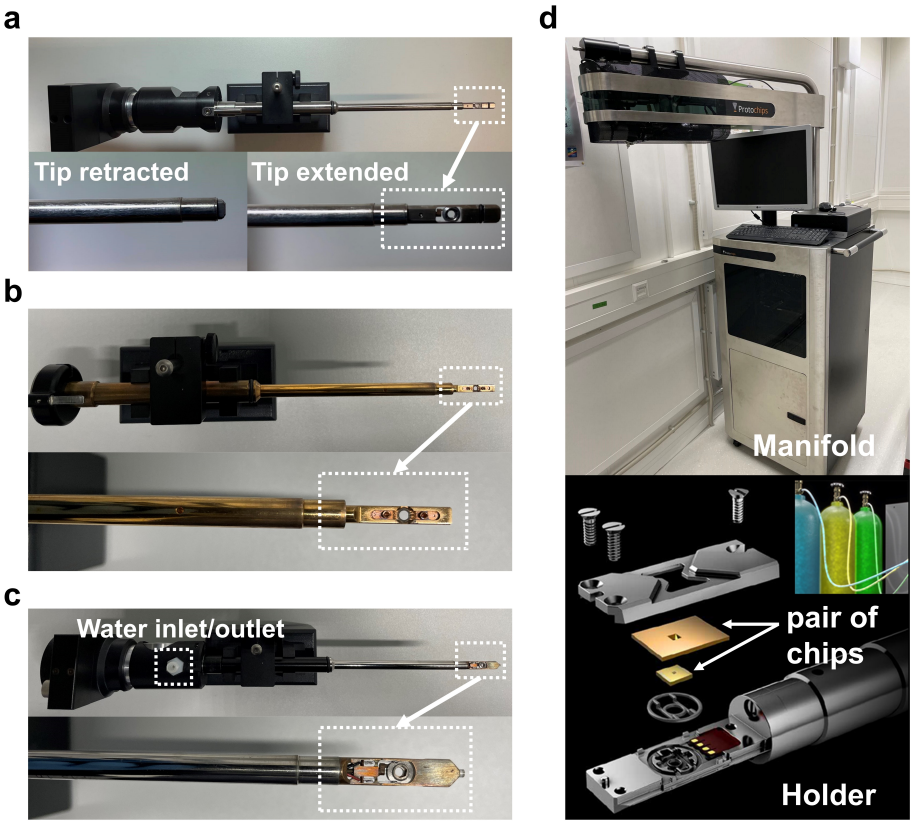

Figure 4.2.: Different TEM holders used at KNMFi for this work: (a) Vacuum transfer holder; (b) Tomography holder; (c) In-situ heating holder; (d) In-situ gas system: manifold and holder. Figure (lower) courtesy from Protochips Inc.

4.2d. Since the materials studied in this work are air-sensitive, the vacuum transfer holder is used for a majority of the experiments. By retracting the holder tip, the loaded TEM grid can be protected and isolated from the atmosphere during transfer from the glovebox to the microscopes (see Figure 4.2a). The tomography holder, which allows for high tilt angles, is used to collect tomographic data (see Figure 4.2b). The in-situ heating holder is used for annealing experiments and provides precise temperature control using a bulk furnace and a water-cooled specimen rod (see Figure 4.2c). The maximal heating temperature is up to 800 °C. As shown in Figure 4.2d, the environmental gas cell system consists of a manifold (controller of the system) and a holder. Unlike other conventional TEM holders, this atmosphere assembly requires two dedicatedly produced E-chips (silicon carbide), which are in varied configurations. A small space can be generated between the two E-chips, which will then be filled with different gases. The maximal pressure and temperature that can be achieved using this system are 0.1 MPa and 1000 °C, respectively.

The vacuum transfer holder was used to conduct the following TEM experiments. TEM bright-field images were acquired to gain an overview of the materials' distribution (see Subsection 3.3.1), while HRTEM images (see Subsection 3.3.3) and selected area electron diffraction (SAED) patterns were obtained to ascertain the materials' crystalline structure (see Section 3.2). A OneView camera (AMETEK Gatan) was used for all these acquisitions. The related analyses were performed using software, including Digital Microscopy (AMETEK Gatan), Vesta (open-source), and Diamond (Crystal Impact). Scanning TEM (STEM) images were obtained to determine the respective material distribution by comparing it with EDXS elemental maps (see Subsection 3.3.2). A high-angle annular dark-field (HAADF) detector was utilized for acquisition, and the software Velox (Thermo Fisher Scientific) was used for analysis. Energy-dispersive X-ray spectroscopy (EDXS) spectrum-imaging (SI) was employed to acquire elemental information about the materials, particularly for regions with large thickness, using a Super-X windowless EDX detector (Thermo Fisher Scientific) for acquisition and Velox for analysis (see Subsection 3.4.1). The empirical model was adopted for spectral background correction. For quantification, the absorption correction was performed by using a sample thickness of 100 nm and the density of 1.5, 2.6, or 3.6 g/cm^3 for Mg-related materials in the respective cases, with Brown-Powell used for the ionization cross-section model. All the EDXS elemental maps are shown based on the net (background corrected and fit) intensity. To enhance the signal-to-noise ratio of the quantitative analysis, PCA was also applied to some cases, executed in Digital Microscopy. Electron energy-loss spectroscopy (EELS) SI was carried out using a Continuum 970 HighRes imaging filter (GIF) (AMETEK Gatan) to perform the qualitative analysis for regions of smaller thickness and boron identification (see Subsection 3.4.2). Background modeling was conducted in Digital Microscopy for the qualitative analysis. 4D-STEM measurements were carried out in μ-probe mode using the OneView camera and Digital Microscopy, where the collected dataset provided spatial and crystalline information about the materials at the same time.

To acquire the 3D structural information about materials, electron tomography was performed in STEM mode using the tomography holder (see Section 3.5). This involved the acquisition of projections at a series of tilt angles, the alignment of tilt series, the reconstruction and visualization of the acquired data. The collection of projections is the same as that of recording TEM or STEM images at different α tilt angles. However, due to a limited tilt range for TEM, elongation artifacts may occur and deteriorate the reconstruction quality. In practice, it is usually not possible to obtain projections at high angles (normally >80° and <-80°), which is due to the geometry of the sample and the sample holder. To minimize these artifacts and improve the quality of reconstruction, the reconstruction for this work is based on sufficient projections covering at least 0 to ±70° of the tilt range. Furthermore, it is essential to ensure that the imaging bias and offset are consistent and signal over-saturation is prevented to maintain linearity between recorded image intensities and projection angles. Successful reconstruction in electron tomography requires that this crucial

prerequisite is met. The alignment of tilt series is a necessary step in electron tomography to rectify spatial shifts between successive projections and potential imperfect rotation axes that may impair reconstruction quality. Cross-correlation combined with tilt axis adjustment and fiducial marker tracking were executed for tilt axis adjustment using open-source software IMOD [159]. The aligned data were then reconstructed using SIRT in Inspect3D (Thermo Fisher Scientific) with a iteration number of 100 applied to prevent degradation of the reconstruction. Post-processing, such as surface rendering, volume rendering, and segmentation, was also applied for better visualization. Finally, ImageJ (open-source) and Avizo 2020.2 (Thermo Fisher Scientific) were utilized for the visualization purpose.

In addition to ex-situ TEM experiments, more information about the materials can be obtained through in-situ TEM experiments, which is also important for this work. It was previously reported that the dehydrogenation of $NaBH_4$-MgH_2 can occur under the pressure less than 0.1 MPa, while only the pressure larger than 0.1 MPa allows for the dehydrogenation of $LiBH_4$. Since the in-situ gas system allows for a maximal pressure of 0.1 MPa, $NaBH_4$-MgH_2 was selected for in-situ investigation, rather than $LiBH_4$-MgH_2. For the respective measurement, the temperature was increased from room temperature at a certain rate after reaching the target pressure. To further understand the behavior of $NaBH_4$-MgH_2 at a high temperature, in-situ annealing investigation was also carried out using the in-situ heating holder. The data collected from the respective in-situ experiments were analyzed using the corresponding software introduced above.

5. Results

The relevant results pertaining to both lithium and sodium reactive hydride composites (Li-RHCs and Na-RHCs) are presented in this chapter. Section 5.1 and Section 5.2 focus on the study of MgB_2 formation for Li-RHCs, with emphasis on its microstructure. In Section 5.3, both ex-situ and in-situ experiments were conducted for Na-RHCs to obtain a deeper understanding. To provide clarity and simplicity, the relevant parameters for each experiment will be provided in the figure captions using the abbreviations listed in Table 5.1. The material preparation, kinetics measurements (gas volumetric), and XRD analyses, described in this chapter, were carried out by Yuanyuan Shang at Hereon. Data analysis and visualization of electron tomography were supported by Xiaohui Huang at KIT. It is important to note that some of the results have been published in the papers [160, 161].

Table 5.1.: Abbreviation list of applied parameters for TEM experiments.

Param.	Screen Current	Exposure Time	Dwell Time	Pixel Size	Camera Length	Convergence Angle
Abbr.	SC	ET	DT	PS	CL	CA

5.1. MgB_2 Nucleation in Li-RHC and Additive Effect

In this section, a comparative analysis was conducted on $LiBH_4$-MgH_2 samples, both without and with additives, aiming to attain a comprehensive understanding of the accelerated nucleation process, as introduced in Section 2.4.2.3. Different states of $LiBH_4$-MgH_2 without additives, including as-milled, incubated, incompletely-desorbed, and (completely) desorbed during the dehydrogenation process, were investigated through TEM techniques, along with XRD and kinetics measurements for the corresponding samples. The selected additive utilized for this study is $3TiCl_3{\cdot}AlCl_3$, considering its practical cost-effectiveness [28]. To enhance the additive's effect

and enable more effective data analysis using TEM, an overdose of 10 mol% and 20 mol% $3TiCl_3 \cdot AlCl_3$ was applied to $LiBH_4$-MgH_2 in different states.

5.1.1. Kinetics Measurement

The dehydrogenation process of $LiBH_4$-MgH_2 is depicted in Figure 5.1. The change in hydrogen content for $LiBH_4$-MgH_2 without additives is represented by the black line, while different states during dehydrogenation, including as-milled, incubated, incompletely-desorbed, and desorbed, are denoted by the timestamps A to D, respectively. The purple line indicates the change in hydrogen content for $LiBH_4$-MgH_2 with 10 mol% $3TiCl_3 \cdot AlCl_3$. The temperature change is represented by the red curve in Figure 5.1. Both samples underwent similar annealing conditions, with a heating rate of 10 °C/min from room temperature to 400 °C under a hydrogen atmosphere at a pressure of 0.4 MPa. Once the annealing temperature was reached, the materials were held at isothermal conditions until the completion of the dehydrogenation process.

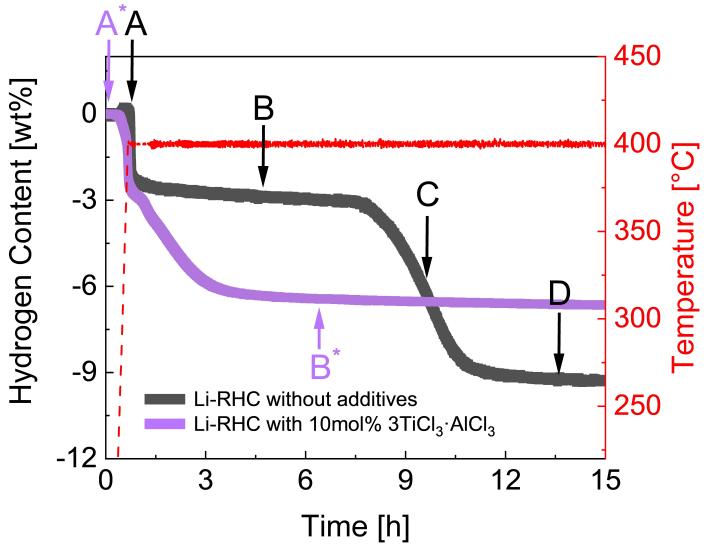

Figure 5.1.: Kinetics measurement conducted during the dehydrogenation of $LiBH_4$-MgH_2 without additives (black line) and $LiBH_4$-MgH_2 with 10 mol% $3TiCl_3 \cdot AlCl_3$ (purple line) under a temperature of 400 °C (red line) and a rate of 10 °C/min, and at a pressure of 0.4 MPa. The different states of the sample $LiBH_4$-MgH_2 without additives during dehydrogenation are represented by the timestamp A, B, C and D. Despite the reduction in hydrogen storage capacity, it is noteworthy that the dehydrogenation kinetics was significantly improved by the addition of additives, resulting in a reduction of the total duration from approximately 11 hours to 3 hours. The different states of the sample $LiBH_4$-MgH_2 with additives during dehydrogenation are represented by the timestamp A^* and B^*. The kinetics measurements were performed by Yuanyuan Shang at Hereon. Figure courtesy of [162].

As shown in Figure 5.1, the various states of the sample without additives throughout the dehydrogenation process are indicated by the labels A to D on the black line. The labels employed in this study are defined as follows: Label A corresponds to the as-milled state, reflecting the hydrogenated state of Li-RHC immediately after ball milling. Label B characterizes the incubated state where the decomposition of MgH_2 is complete, but substantial advancement in the reaction between Mg and $LiBH_4$ has not yet been observed. Label C is assigned to the state during the second phase of extensive hydrogen release, indicating significant progress in the reaction between Mg and $LiBH_4$. Label D signifies the state where the dehydrogenation process has been concluded. For the sample with 10 mol% $3TiCl_3{\cdot}AlCl_3$, the different states of interest are labeled as A^* and B^*. The A^* label corresponds to the as-milled state, and the B^* label represents the state where the dehydrogenation process has been completed.

In general, Figure 5.1 demonstrates that the dehydrogenation process had a duration of approximately 11 hours for $LiBH_4$-MgH_2 without additives (black curve), while it was reduced to approximately 3 hours for $LiBH_4$-MgH_2 with additives (purple curve). As the temperature increased from room temperature to around 300 °C, both samples released about 3 wt% H_2, signifying the decomposition of MgH_2 into Mg and H_2. Subsequently, a significant incubation plateau was observed in the absence of additives. During this period of over 6 hours, there was almost no release of hydrogen, indicating that the dehydrogenation process for $LiBH_4$-MgH_2 was interrupted after the decomposition of MgH_2. This interruption was followed by a substantial release of H_2 as a result of the reaction between $LiBH_4$ and Mg. In general, the dehydrogenation process extended to a duration of up to 11 hours. In contrast, as explained in Subsection 2.3.1, the addition of additives resulted in a significant reduction in the width of the incubation plateau. This reduction indicates that the reaction between $LiBH_4$ and Mg was accelerated, attributed to the accelerated nucleation of MgB_2.

Furthermore, the dehydrogenation of the sample without additives resulted in a hydrogen yield of less than 10 wt%, which falls short of the expected theoretical value of 11.5 wt%. The inadequate yield could be attributed to several factors, such as the partial oxidation of $LiBH_4$ and/or MgH_2, the low purity of the raw materials provided by the suppliers, or the inhomogeneous dispersion of reactants during the ball milling process. On the other hand, the sample with additives exhibited an even lower yield of only about 6 wt% H_2. This can primarily be attributed to the inclusion of an overdose of additives, which is detrimental to the theoretical hydrogen storage capacity. In this case, the intentional high dose of 10 mol% $3TiCl_3{\cdot}AlCl_3$ is chosen to enhance the effect of the additive, leading to an observable change in the morphology of MgB_2.

5.1.2. Li-RHC without Additive

5.1.2.1. As-Milled State

The sample of as-milled $LiBH_4$-MgH_2 without additives was depicted in Figure 5.2. This sample corresponded to the timestamp A in Figure 5.1. An XRD spectrum for the sample is shown in Figure 5.2a, while a HAADF-STEM image in a region of interest is presented in Figure 5.2b. An electron diffraction pattern acquired locally in the same region as Figure 5.2b is displayed in Figure 5.2c, and the corresponding EDXS elemental map of Mg and O for the same region is shown in Figure 5.2d. In addition, the atomic fraction of Mg and O by EDXS quantification is presented in Table 5.2.

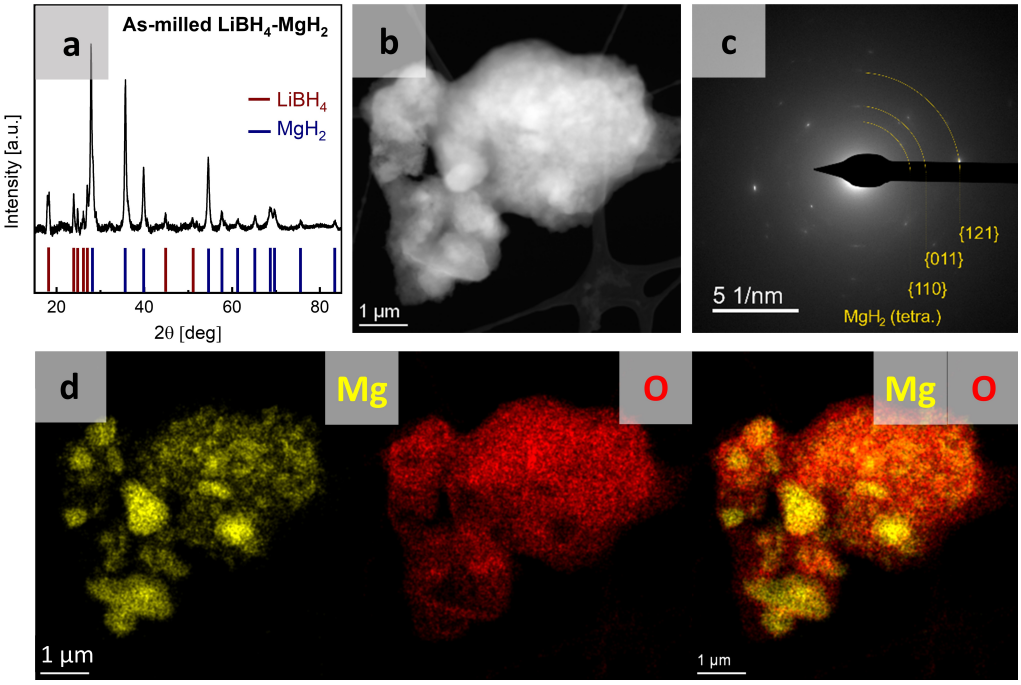

Figure 5.2.: As-milled $LiBH_4$-MgH_2 without additives: (a) a XRD spectrum; (b) a HAADF-STEM image; (c) a diffraction pattern acquired in the corresponding region using a SC of 500 pA and a ET of 8s; (d) EDXS elemental maps of Mg (K-line) and O (K-line) for the same region, generated by integrating 176 frames with a SC of 58 pA, a DT of 12 μs, a PS of 13.15 nm, a CL of 91 mm, and a CA of 30 mrad. MgH_2 was identified by both XRD and electron diffraction, while $LiBH_4$ was only identified by XRD, which is presumably attributed to the oxidation of $LiBH_4$. The XRD measurements and phase analyses were performed by Yuanyuan Shang at Hereon. Figure courtesy of [162].

Based on the XRD spectrum shown in Figure 5.2a, $LiBH_4$ and MgH_2 could be identified. The HAADF-STEM image in Figure 5.2b shows a region of interest for the sample. The corresponding locally acquired diffraction pattern of this region confirms the existence of MgH_2, as illustrated in Figure 5.2c. In contrast, $LiBH_4$ was not identified by the electron diffraction. To determine the size and distribution of MgH_2 crystals, an EDXS elemental map of Mg was acquired, shown in Figure 5.2d. In order to account for the air sensitivity of the sample [163] and the oxygen existing in the TEM column, the inclusion of an EDXS elemental map of O as a reference for samples in this work may be helpful. The EDXS mapping indicated the presence of Mg-containing grains with a diameter of up to tens of hundred nanometers. In addition, these Mg-containing grains were surrounded by O-containing materials. It is also noted that no correlation between the distribution of Mg and O was observed. This suggests that the oxidation of Mg is almost negligible. With this information, MgH_2 can be considered as the only Mg-containing material in this case. The EDXS map of Mg can therefore indicate the distribution of MgH_2.

A quantitative EDXS analysis presented in Table 5.2 revealed that the atomic fraction of O is more than twice that of Mg in this region. The excessive amount of oxygen present in this region may be related to the other material of the sample, $LiBH_4$, suggesting the oxidation of $LiBH_4$. This may explain the absence of crystal information about $LiBH_4$ in the electron diffraction pattern. The oxidation of $LiBH_4$ can be attributed to residual oxygen in the TEM column or during transport from Helmholtz-Zentrum Hereon to Karlsruhe Institute of Technology. The absence of $LiBH_4$ has also been reported in previous studies, with challenges arising in characterizing light borohydride compounds using TEM techniques [89, 164]. It has been suggested that the oxidation products of the $LiBH_4$ phase consist of boron oxide-like species, which possess an amorphous structure and therefore cannot be identified through electron diffraction.

Table 5.2.: EDXS quantitative analysis conducted on as-milled $LiBH_4$-MgH_2 without additives.

Element	Family	Atomic Fraction [at%]
O	K	71.5 ± 4.1
Mg	K	28.5 ± 4.1

5.1.2.2. Incubated State

To determine the phases after the first dehydrogenation step, the sample of incubated $LiBH_4$-MgH_2 without additives was studied, as shown in Figure 5.3. This sample state corresponds to timestamp B in Figure 5.1, which represents the midpoint of the wide plateau region. It occurs after the complete decomposition of MgH_2 into Mg and H_2, but before the significant advancement

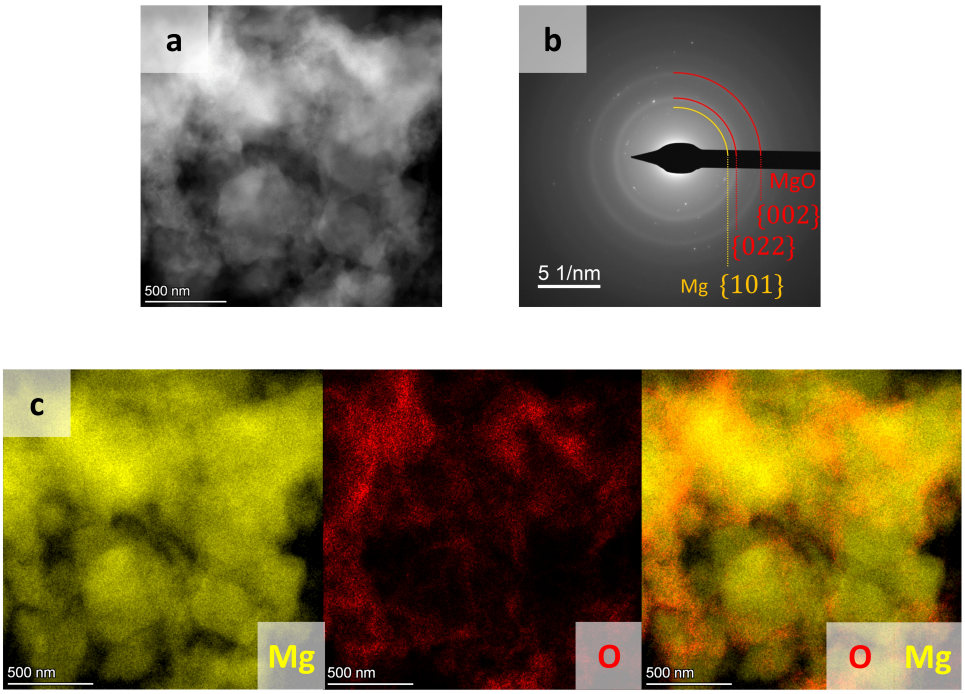

Figure 5.3.: Incubated $LiBH_4$-MgH_2 without additives: (a) a HAADF-STEM image; (b) a diffraction pattern acquired in the corresponding region using a SC of 500 pA and a ET of 4s; (c) EDXS elemental maps of Mg (K-line) and O (K-line) for the same region, generated by integrating 176 frames with a SC of 58 pA, a DT of 12 μs, a PS of 13.15 nm, a CL of 91 mm, and a CA of 30 mrad. It is illustrated that the generated Mg grains generally have a size of several hundred nanometers, while oxidation simultaneously occurred on their surface layers.

of the reaction between $LiBH_4$ and Mg. Figure 5.3a presents a HAADF-STEM image recorded in a region of interest, while Figure 5.3b shows an electron diffraction pattern acquired locally in the same region. Figure 5.3c displays the corresponding EDXS elemental map of Mg and O for the same region.

The size, distribution and morphology of materials in the sample after the first step of dehydrogenation of $LiBH_4$-MgH_2 is depicted in the HAADF-STEM image in Figure 5.3a. Based on the diffraction pattern in Figure 5.3b, Mg and MgO could be identified. Again, $LiBH_4$ remained undetected via electron diffraction. This is most likely also due to oxidation. The identification of MgO in this case indicates partial oxidation of Mg. This can be observed by the presence of orange regions in the mixed map of Mg and O in Figure 5.3c. To differentiate between the distribution of Mg and MgO, EDXS mapping was carried out, as displayed in Figure 5.3c. The correlation between the distribution of Mg and O is subtle and primarily limited to the outermost region of the Mg grains. Considering the blurry rings observed for MgO in the diffraction pattern, it is highly probable that the oxidation of Mg occurred primarily on the outer layer of the Mg

grains. Similarly, akin to the preceding Section 5.1.2.1, the scale of Mg grains corresponds to that of MgH_2 grains, characterized by a diameter of several hundred nanometers.

5.1.2.3. Desorbed State

The sample of desorbed $LiBH_4$-MgH_2 plays a crucial role in comprehending the mechanism of nucleation and growth of MgB_2, as demonstrated in Figure 5.4. This sample is represented in Figure 5.1 at timestamp D, indicating the completion of the entire dehydrogenation process that generates both MgB_2 and LiH. Figure 5.4a depicts the XRD spectrum of the entire sample. Figure 5.4b illustrates a HAADF-STEM image captured from a region of interest, and Figure 5.4c displays the corresponding electron diffraction pattern. Figure 5.4d shows the EDXS elemental map of Mg and O for the selected area in Figure 5.4b. Additionally, the atomic fraction of Mg and O obtained from the EDXS quantification for the same region is outlined in Table 5.3.

Two compounds, MgB_2 and LiH, generated during the dehydrogenation process were identified in the XRD spectrum shown in Figure 5.4a. The HAADF-STEM image in Figure 5.4b exhibits a significant microstructural feature where the crystals' spatial orientation is parallel, as indicated by the parallel dashed lines. These crystals were typical in this case, whereas they were not observed in the earlier stages, suggesting that they form during the dehydrogenation process of $LiBH_4$-MgH_2. A local diffraction pattern was acquired, as shown in Figure 5.4c, to identify the crystals present in this region. The diffraction pattern confirms the existence of MgB_2 in a hexagonal closed packed (hcp) structure (P6m/mm, No. 191). However, LiH was not detected, despite being previously identified by XRD. This may be attributed to the sensitivity of LiH to air and electron beam [166, 167]. Previous studies have reported the high instability (oxidation and decomposition) of LiH under electron beam irradiation [89].

Table 5.3.: EDXS quantitative analysis conducted on desorbed $LiBH_4$-MgH_2 without additives.

Element	Family	Atomic Fraction [at%]
O	K	19.6 ± 2.9
Mg	K	80.4 ± 2.9

Although these parallel-oriented crystals are likely to be MgB_2, further confirmation is required to validate the identification of these crystals. Therefore, EDXS mapping was conducted in the selected area in Figure 5.4b, as depicted in Figure 5.4d. It was found that the contrast of these crystals observed in the HAADF-STEM image matches the contrast provided by magnesium, as shown in its EDXS elemental map. To consider the potential oxidation of materials during the

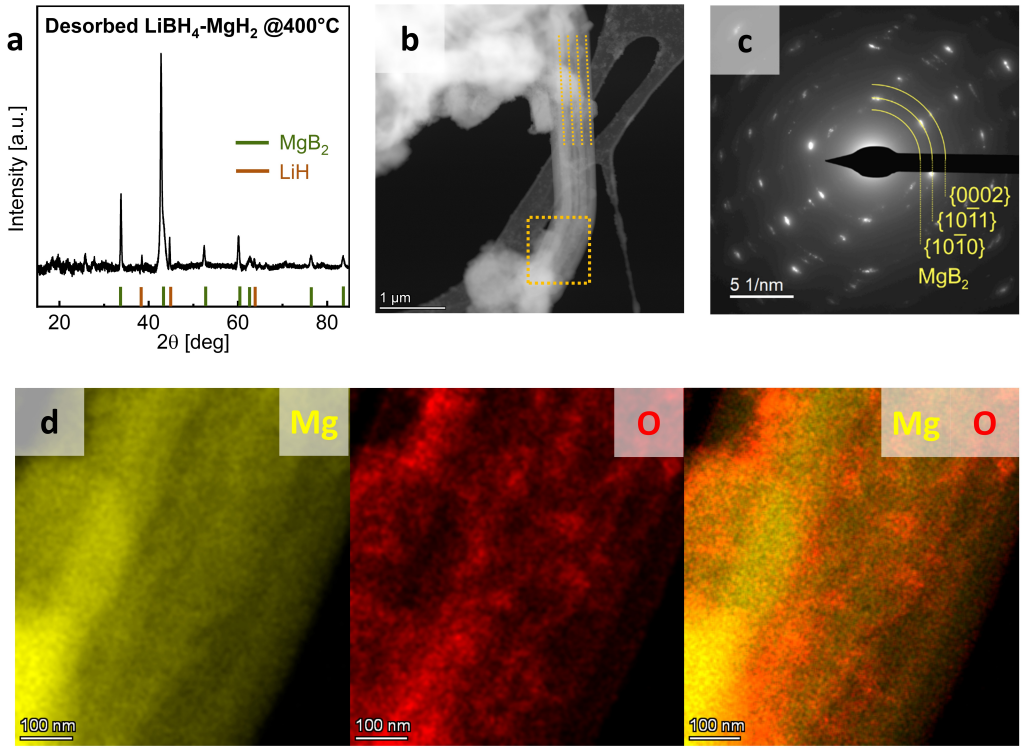

Figure 5.4.: Desorbed $LiBH_4$-MgH_2 without additives: (a) XRD analysis; (b) a HAADF-STEM image; (c) a diffraction pattern acquired in the corresponding region using a SC of 500 pA and a ET of 2s; (d) EDXS elemental maps of Mg (K-line) and O (K-line) for the same region, generated by integrating 472 frames with a SC of 180 pA, a DT of 30 μs, a PS of 2.32 nm, a CL of 91 mm, and a CA of 30 mrad. The identification of the spatially parallel-oriented crystals as MgB_2 was determined, as indicated by the parallel dashed lines. The XRD measurements and phase analyses were performed by Yuanyuan Shang at Hereon. Figure courtesy of [165].

dehydrogenation process, the EDXS elemental map of O was included. The overlapped EDX elemental map of O and Mg reveals a few areas with orange contrast, indicating an equivalent distribution of both elements in these specific regions. However, the persistence of the parallel feature in yellow (Mg map in 5.4c) and the absence of MgO detection through electron diffraction lead to the inference that there is no correlation between Mg and O in this particular region. In other words, the slight oxidation of Mg can be disregarded. Given that MgB_2 is the only Mg-containing crystal, these parallel-oriented crystals were assigned to be MgB_2. Additionally, the EDXS quantification in Table 5.3 reveals a noticeable amount of oxygen still present in the surrounding area of MgB_2. Taking into account the oxidation of LiH, the EDXS map of O can potentially indicate the distribution of LiH.

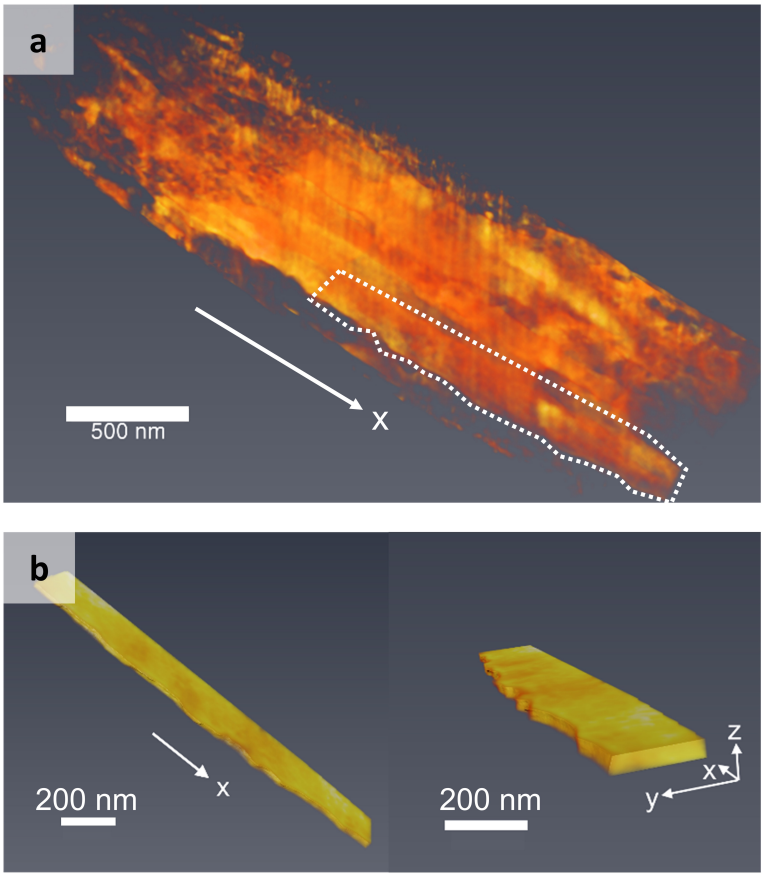

Figure 5.5.: Desorbed $LiBH_4$-MgH_2 without additives: (a) a volume rendering obtained from the tomographic reconstruction of MgB_2 crystals using a SC of 186 pA, a DT of 5 μs, a PS of 1.64 nm, a CL of 91 mm, a CA of 8.6 mrad, and a tilt range from -72° to 78° at a tilt step of 2°. The alignment of the tilt series was performed using 10 nm gold colloidal particles as fiducial markers and the reconstruction algorithm employed is SIRT with 100 iterations. (b) a volume rendering of the highlighted piece of MgB_2 crystals in subfigure a, illustrated in different directions. It was observed that generated MgB_2 crystals have a rectangular bar-shaped morphology and predominantly grow with the same spatial orientation. Figure courtesy of [165].

To achieve a more comprehensive understanding of MgB_2 morphology and minimize the ambiguities raised in 2D space, STEM tomography was conducted. A volume rendering of the parallel-oriented MgB_2 crystals was reconstructed from the HAADF-STEM tomographic data, as shown in Figure 5.5a. Figure 5.5b displays a single piece of the parallel-oriented MgB_2 crystals viewed from different angles. It was observed that the parallel-oriented MgB_2 crystals possess a flat rectangular bar-shaped morphology, with an aspect ratio of several tens for the basal plane in relation to the x-direction and y-direction. In other words, the anisotropic growth behavior

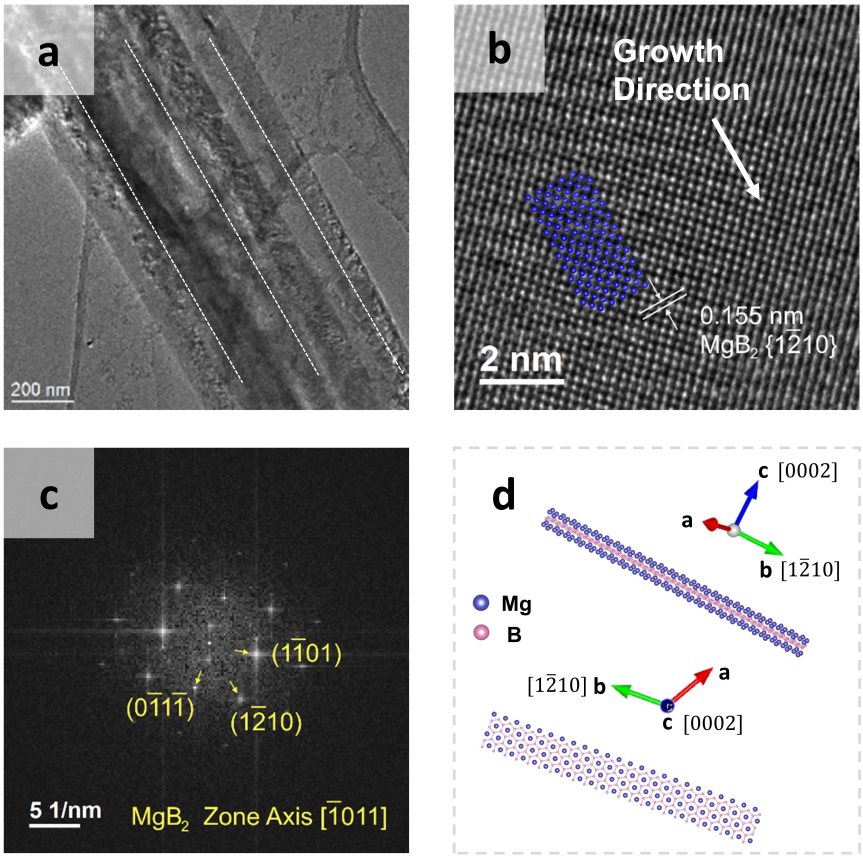

Figure 5.6.: Desorbed $LiBH_4$-MgH_2 without additives: (a) a TEM BF image showing the parallelism of the generated MgB_2 crystals; (b) a HRTEM image recoreded in the local area of subfigure a; (c) the corresponding FFT of the HRTEM image; (d) a schematic illustration depicting the crystal orientations of a rectangular MgB_2 bar. With respect to the rectangular bar-shaped morphology, the crystal orientations of MgB_2 crystals were determined to be $\langle 1\,0\,\bar{1}\,0 \rangle$ for the moderate growth, $\langle 1\,\bar{2}\,1\,0 \rangle$ for the predominant growth and $\langle 0\,0\,0\,2 \rangle$ for the restricted growth. Figure courtesy of [165].

for MgB_2 was significant, with predominant growth in the x-direction, moderate growth in the y-direction, and limited growth in the z-direction.

The crystal orientation for the predominant growth of the observed bar-shaped MgB_2 crystals was determined using HRTEM. An overview image of some parallel-oriented MgB_2 crystals was acquired through TEM bright-field imaging, as shown in Figure 5.6a. The white dashed lines in the image highlight the predominant growth direction. The HRTEM image in Figure 5.6b was captured from the edge area of these crystals. The corresponding Fast Fourier Transform (FFT)

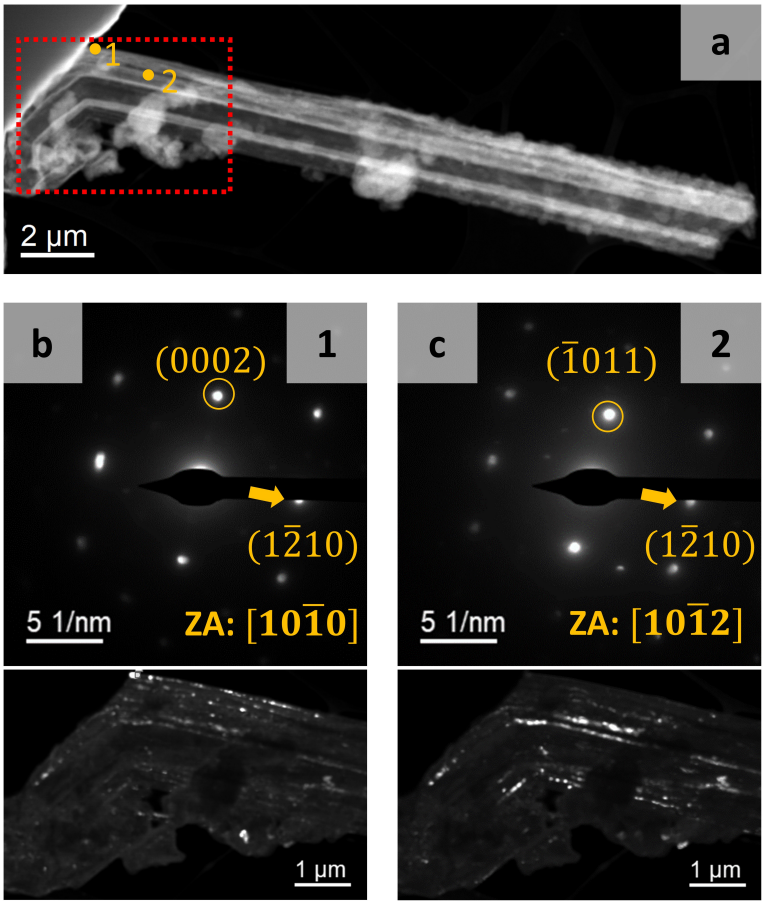

Figure 5.7.: Desorbed $LiBH_4$-MgH_2 without additives: (a) a HAADF-STEM image showing the region of interest for 4D-STEM analysis. The dataset of 4D-STEM was collected in the selected area highlighted by red dashed line using a SC of 500 pA, a DT of 13 ms, a PS of 14.80 nm, a CL of 720 mm, and a CA of 1.1 mrad; (b-c) diffraction patterns acquired in the highlighted areas 1 and 2 in subfigure a (the upper row), with the corresponding virtual images mapped by the selected diffraction spots $(0\,0\,0\,2)$ and $(\bar{1}\,0\,1\,1)$ in the respective diffraction patterns (the lower row). It was confirmed that the MgB_2 crystals grow predominantly not only in the same spatial direction, but also in the same crystal orientation, indicating heterogeneous nucleation for MgB_2 crystals. Figure courtesy of [162].

shown in Figure 5.6c was analyzed to determine the crystal orientation. It was found that the crystal orientation with respect to the predominant growth direction (x-direction) is $\langle 1\,\bar{2}\,1\,0\rangle_{MgB_2}$.

According to Lee et al. [168], a growth constraint was observed for MgB_2 along the c-axis $\langle 0\,0\,0\,2\rangle_{MgB_2}$. The limited growth depicted in Figure 5.5b is likely due to this constraint. Therefore, the z-direction in Figure 5.5b represents the c-axis of MgB_2 crystals, specifically the crystal orientation $\langle 0\,0\,0\,2\rangle_{MgB_2}$. With the determined crystal orientations for the x-direction and

z-direction, the crystal orientation for the moderate growth (y-direction in Figure 5.5b), which is perpendicular to $\langle 1\,\bar{2}\,1\,0\rangle_{MgB_2}$ (x-direction) and $\langle 0\,0\,0\,2\rangle_{MgB_2}$ (z-direction), can be determined. A rectangular bar-shaped schematic representation of MgB_2 in Figure 5.6d illustrates dominant growth orienting in $[1\,\bar{2}\,1\,0]_{MgB_2}$ (b-axis) and restricted growth orienting in $[0\,0\,0\,2]_{MgB_2}$ (c-axis). Therefore, the crystal orientation for moderate growth was determined to be $\langle 1\,0\,\bar{1}\,0\rangle_{MgB_2}$.

In order to investigate whether all MgB_2 crystals are predominantly grown along the same crystal orientation, specifically $\langle 1\,\bar{2}\,1\,0\rangle_{MgB_2}$, a 4D-STEM analysis was conducted. The region highlighted by the red dashed square in Figure 5.7a represents the area chosen for 4D-STEM acquisition. Figure 5.7b-c display the diffraction patterns for the selected areas 1-2 in Figure 5.7a, along with the corresponding virtual images that were generated by mapping the selected reflections.

The obtained diffraction patterns with different zone axes confirmed that all the spatially parallel-oriented crystals were identified as MgB_2. The distribution of MgB_2 crystals was then virtually mapped by selecting the reflections $(0\,0\,0\,2)$ and $(\bar{1}\,0\,1\,1)$ in the respective diffraction patterns. The parallel arrangement of the crystals, as observed in the virtual images, provided further validation of the identification of MgB_2. The corresponding crystal orientations, determined to be $\langle 1\,\bar{2}\,1\,0\rangle_{MgB_2}$ in relation to the predominant growth observed in Figure 5.7a, were found to be consistent. This suggests that not only do the MgB_2 crystals grow in the same spatial direction predominantly, but they also possess the same crystal orientation, specifically $\langle 1\,\bar{2}\,1\,0\rangle_{MgB_2}$. Moreover, the parallelism observed among these MgB_2 crystals indicates the occurrence of heterogeneous nucleation on the same nucleation center. Thus, it is crucial to determine the nucleation center for these parallel-oriented MgB_2 crystals. This will be investigated in the subsequent section.

5.1.2.4. Incompletely-Desorbed State

The sample of incompletely-desorbed $LiBH_4$-MgH_2 was studied to determine the nucleation center responsible for the formation of parallel bar-shaped MgB_2 crystals, as depicted in Figure 5.8. This sample corresponds to timestamp C in Figure 5.1, representing the point prior to the completion of the dehydrogenation process. The XRD spectrum obtained for the sample is shown in Figure 5.8a. Figure 5.8b displays a HAADF-STEM image captured in a region of interest. Additionally, the corresponding elemental map of Mg and O for the same region is presented in Figure 5.8c.

The XRD spectrum in Figure 5.8a reveals the identification of $LiBH_4$, Mg, MgB_2, and LiH. According to Reaction 5 of the two-step dehydrogenation process, MgB_2 and LiH are the resulting products from the reaction between $LiBH_4$ and Mg, indicating the ongoing progress

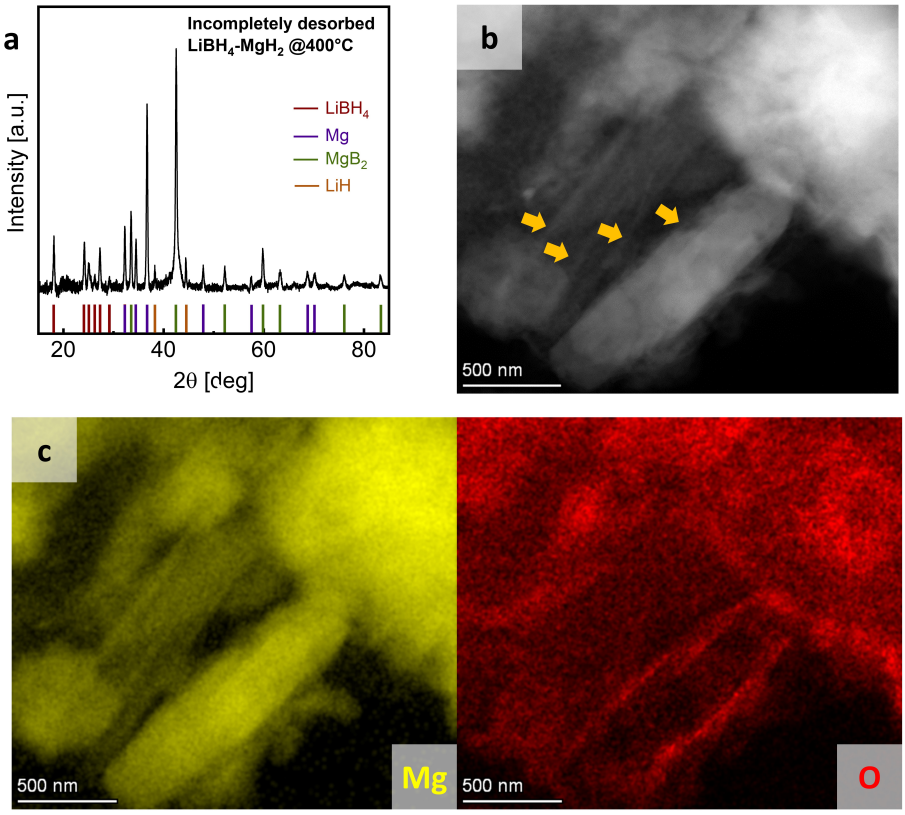

Figure 5.8.: Incompletely-desorbed $LiBH_4$-MgH_2 without additives: (a) XRD analysis; (b) a HAADF-STEM image; (c) EDXS elemental maps of Mg (K-line) and O (K-line) for the same region, generated by integrating 190 frames with a SC of 160 pA, a DT of 20 μs, a PS of 4.50 nm, a CL of 91 mm, and a CA of 30 mrad. At this stage, parallel-oriented crystals were observed, which can be either MgB_2 or Mg. The XRD measurements and phase analyses were performed by Yuanyuan Shang at Hereon.

of this reaction. The presence of $LiBH_4$ and Mg verifies that the reaction has not yet reached completion. Parallel-oriented crystals were observed in the HAADF-STEM image in Figure 5.8b, as indicated by the arrows. To identify these crystals, EDXS mapping was carried out. The distribution of element Mg and O is shown in Figure 5.8c. As a result, these observed parallel-oriented crystals were confirmed to be Mg-containing crystals, according to the EDXS map of Mg. In addition, considering the low intensity of O in the corresponding region as observed in the EDXS map, it is possible to eliminate the possibility of these Mg-containing crystals being MgO.

In order to identify the Mg-containing crystals, 4D-STEM analysis was conducted on the same area, as depicted in Figure 5.9. The HAADF-STEM image of this area is shown in Figure 5.9a. The diffraction patterns acquired from selected areas 1-7 in Figure 5.9a are presented in

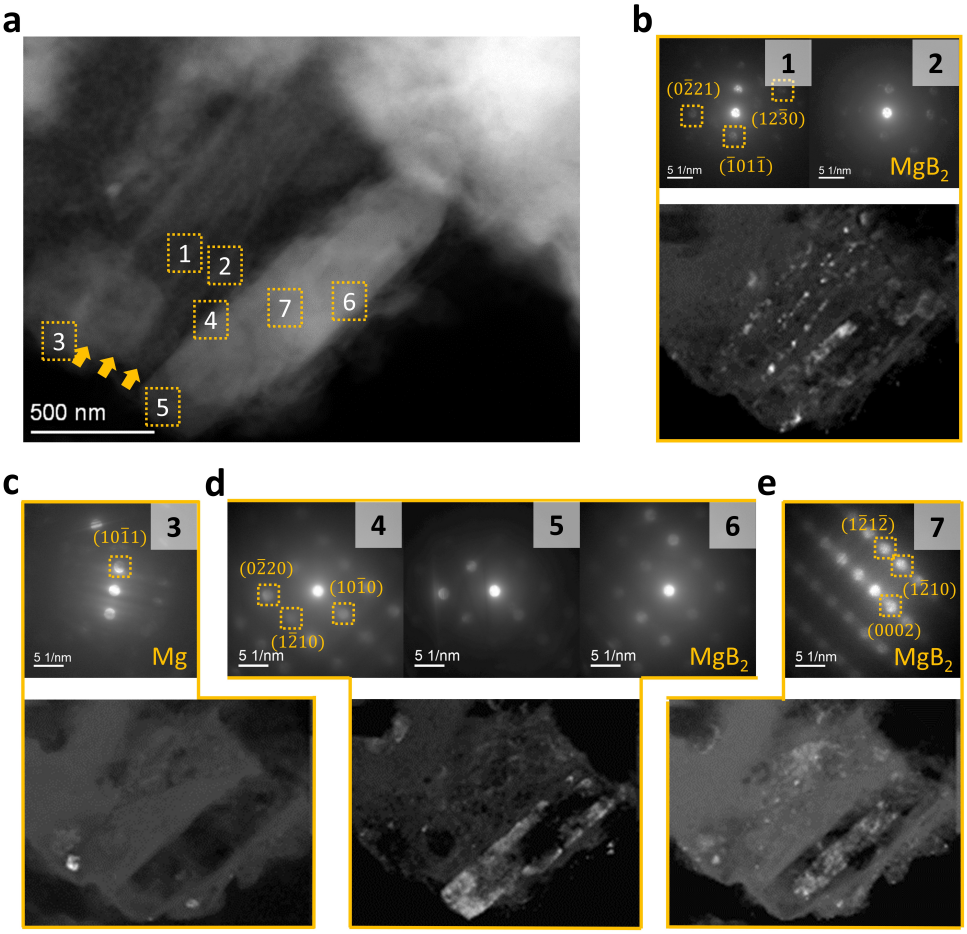

Figure 5.9.: Incompletely-desorbed $LiBH_4$-MgH_2 without additives: (a) a HAADF-STEM image showing the region for acquiring a 4D-STEM dataset using a SC of 50 pA, a DT of 100 ms, a PS of 10.3 nm, a CL of 580 mm, and a CA of 1.54 mrad; (b) identical diffraction patterns from the selected areas 1 and 2 in subfigure a identified the presence of MgB_2. The virtual image was constructed based on the diffraction spots $(0\,\bar{2}\,2\,1)$, $(\bar{1}\,0\,1\,\bar{1})$, and $(1\,2\,\bar{3}\,0)$; (c) a diffraction pattern acquired from the selected area 3 in subfigure a identified Mg. The virtual image was obtained using the diffraction spot $(\bar{1}\,0\,1\,\bar{1})$; (d) identical diffraction patterns from the selected areas 4-6 in subfigure a revealed the presence of MgB_2. The corresponding distribution of MgB_2 was inversely mapped by selecting the diffraction spots $(0\,\bar{2}\,2\,1)$, $(1\,0\,\bar{1}\,0)$, and $(1\,\bar{2}\,1\,0)$; (e) a diffraction pattern acquired from the selected area 7 in subfigure a identified MgB_2. The corresponding distribution of MgB_2 was mapped by selecting the diffraction spots $(1\,\bar{2}\,1\,\bar{2})$, $(0\,0\,0\,2)$, and $(1\,\bar{2}\,1\,0)$. Mg grains were identified as the nucleation centers for the heterogeneous nucleation of the parallel bar-shaped MgB_2 crystals.

Figures 5.9b-e, respectively. It can be observed that the diffraction patterns obtained from areas 1 and 2, which identified MgB_2, are identical. This suggests that the parallel-oriented MgB_2 crystals have the same crystal orientations. The corresponding distribution of MgB_2 is inversely

mapped by selecting the diffraction spots $(0\,\bar{2}\,2\,1)$, $(\bar{1}\,0\,1\,\bar{1})$, and $(1\,2\,\bar{3}\,0)$ in both diffraction patterns, confirming the parallelism of these MgB_2 crystals. Moreover, the diffraction pattern from the selected area 3 in Figure 5.9a identifies the presence of Mg, as shown in Figure 5.9c. The corresponding virtual image for Mg is then mapped by selecting the diffraction spot $(1\,0\,\bar{1}\,1)$. The relative positioning of MgB_2 and Mg indicates that the parallel-oriented MgB_2 crystals may grow on the Mg grains. Thus, it is suggested that the Mg grains serve as the nucleation centers for the heterogeneous nucleation of MgB_2 crystals.

Furthermore, it appears that the parallel-oriented MgB_2 crystals observed in Figure 5.9b are connected at the bottom, as indicated by the arrows in Figure 5.9a. To examine this, diffraction patterns were acquired from selected areas 4-7. As shown in Figure 5.9d, the diffraction patterns obtained from areas 4, 5, and 6, which identified MgB_2, are identical. Based on the corresponding virtual image created using the diffraction spots $(1\,\bar{2}\,1\,\bar{2})$, $(0\,0\,0\,2)$, and $(1\,\bar{2}\,1\,0)$, two parallel-oriented MgB_2 crystals were observed in areas 4 and 6, connected at the bottom in area 5. Their primary growth orientations, which are vertical to their connected position, were determined to be $(1\,\bar{2}\,1\,0)$. This is consistent with the observation in Figure 5.7. Additionally, the MgB_2 crystal identified in area 7 exhibits the same primary growth orientation along $(1\,\bar{2}\,1\,0)$, but with a different zone axis, as shown in Figure 5.9e.

5.1.3. Li-RHC with Additive

As previously demonstrated, a significant decrease in the plateau width was achieved through the addition of $3TiCl_3{\cdot}AlCl_3$, as depicted in Figure 5.1. Consequently, this additive was chosen to continue the investigation into its impact on the nucleation and growth of MgB_2. To facilitate the observation and analysis of TEM, excessive concentrations of 10 mol% $3TiCl_3{\cdot}AlCl_3$ and even 20 mol% $3TiCl_3{\cdot}AlCl_3$ were utilized.

5.1.3.1. As-Milled State

The as-milled $LiBH_4$-MgH_2 sample with 10 mol% $3TiCl_3{\cdot}AlCl_3$, referred to as label A* in Figure 5.1, served as a baseline for the further investigation of other samples, as depicted in Figure 5.10. The XRD spectrum for the entire sample is shown in Figure 5.10a. A HAADF-STEM image from a region of interest within the sample is displayed in Figure 5.10b. In addition, Figure 5.10c presents an electron diffraction pattern acquired from the same area. The corresponding EDXS elemental maps of Mg, O, Al, Ti, and Cl are presented in Figure 5.10d.

Upon analyzing the XRD spectrum in Figure 5.10a, the expected presence of $LiBH_4$ and MgH_2 in the as-milled sample of $LiBH_4$-MgH_2 was confirmed. Unexpectedly, the existence

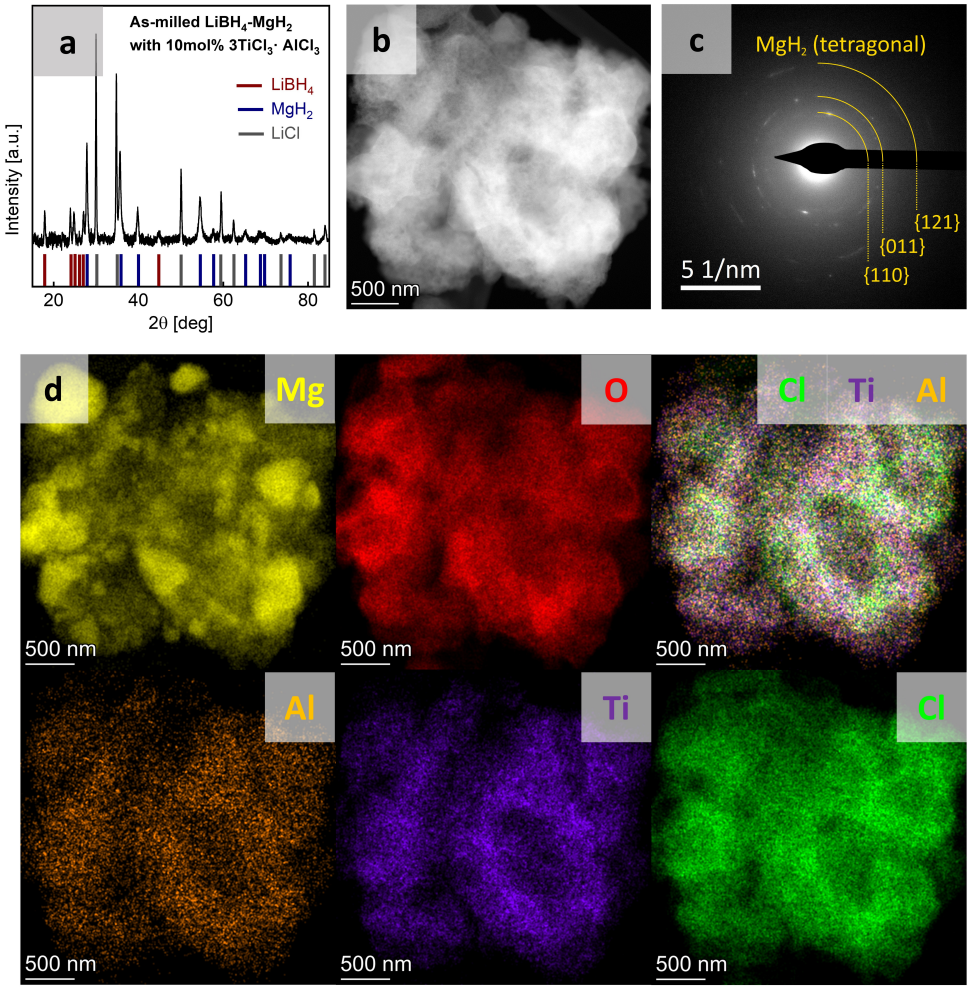

Figure 5.10.: As-milled $LiBH_4$-MgH_2 with 10 mol% $3TiCl_3{\cdot}AlCl_3$: (a) XRD analysis; (b) a HAADF-STEM image; (c) a diffraction pattern acquired in the corresponding region using a SC of 500 pA and an ET of 8 s; (d) EDXS elemental maps of Mg (K-line), O (K-line), Al (K-line), Ti (K-line), and Cl (K-line) for the same region, generated by integrating 566 frames with a SC of 121 pA, a DT of 13 μs, a PS of 4.63 nm, a CL of 91 mm, and a CA of 30 mrad. A reaction may had occurred between $LiBH_4$ and $3TiCl_3{\cdot}AlCl_3$, as evidenced by the identification of LiCl and the uncorrelated distribution among Al, Ti, and Cl before dehydrogenation. The XRD measurements and phase analyses were performed by Yuanyuan Shang at Hereon.

of LiCl crystals was detected. The detection of LiCl in the XRD spectrum suggests a possible reaction between $LiBH_4$ and $3TiCl_3{\cdot}AlCl_3$, as Li is known to exist only in $LiBH_4$ and Cl was exclusively present in $3TiCl_3{\cdot}AlCl_3$. The size, distribution and morphology of materials in the sample were revealed in the HAADF-STEM image depicted in Figure 5.10b. The corresponding diffraction pattern, shown in Figure 5.10c, confirmed the presence of MgH_2 in the local region.

In contrast, both $LiBH_4$ and $LiCl$ were not detected by the electron diffraction. The absence of $LiBH_4$ can be attributed to the degradation caused by the electron beam or to its oxidation, which may occur due to the residual oxygen content present in the TEM column. The inability to detect $LiCl$ may be due to the small size of the $LiCl$ crystals, preventing them from being resolved through electron diffraction in the local region.

EDXS mapping was conducted on the same region shown in Figure 5.10d to obtain the elemental distribution of Mg, O, Al, Ti, and Cl. As illustrated in the EDXS elemental map of Mg, the distribution of the large grains (displayed in yellow) is not correlated with any other elements in this case. Therefore, the distribution of MgH_2 grains, which were observed to be several-hundred nanometers in size, can be represented by these large grains in the EDXS elemental map of Mg. Additionally, the EDXS elemental map of O can indicate the distribution of oxidized $LiBH_4$ if it has undergone oxidation. As the sample contains $3TiCl_3{\cdot}AlCl_3$, the EDXS elemental maps for Al, Ti, and Cl were also included. As observed in the overlapped EDXS map of Cl, Ti, and Al, the distinct colors (purple, green, and orange) are individually visible. This indicates a lack of correlation among the distribution of Al, Ti, and Cl, suggesting the decomposition of the additive $3TiCl_3{\cdot}AlCl_3$. This observation is consistent with the identification of $LiCl$ through XRD analysis and serves as evidence for a reaction most probably between the additive $3TiCl_3{\cdot}AlCl_3$ and $LiBH_4$.

5.1.3.2. Desorbed State

The sample of desorbed $LiBH_4$-MgH_2 with 10 mol% $3TiCl_3{\cdot}AlCl_3$ is referred as Label B* in Figure 5.1 and is depicted in Figure 5.11. The XRD spectrum for the entire sample is presented in Figure 5.11a. Figure 5.11b exhibits a HAADF-STEM image that was acquired from a region of interest within the sample, while the corresponding electron diffraction pattern acquired from the same area is displayed in Figure 5.11c. Additionally, EDXS mapping was performed to demonstrate the distribution of the relevant elements Mg, O, Al, Ti, and Cl, as shown in Figure 5.11d.

According to the XRD spectrum displayed in Figure 5.11a, LiH, MgB_2 and $LiCl$ were detected in the sample of desorbed $LiBH_4$-MgH_2. Similar to the previous case involving the as-milled $LiBH_4$-MgH_2, the detection of $LiCl$ was still present after dehydrogenation. Regarding the morphology of materials in the sample, the presence of parallel-oriented crystals, which were not observed before dehydrogenation, is illustrated in Figure 5.11b through the HAADF-STEM image. Similarly, the electron diffraction pattern obtained for the same local region exclusively identified MgB_2. The absence of LiH in the diffraction pattern is likely due to oxidation, while the lack of detection of $LiCl$ can be attributed to the small size of the crystals.

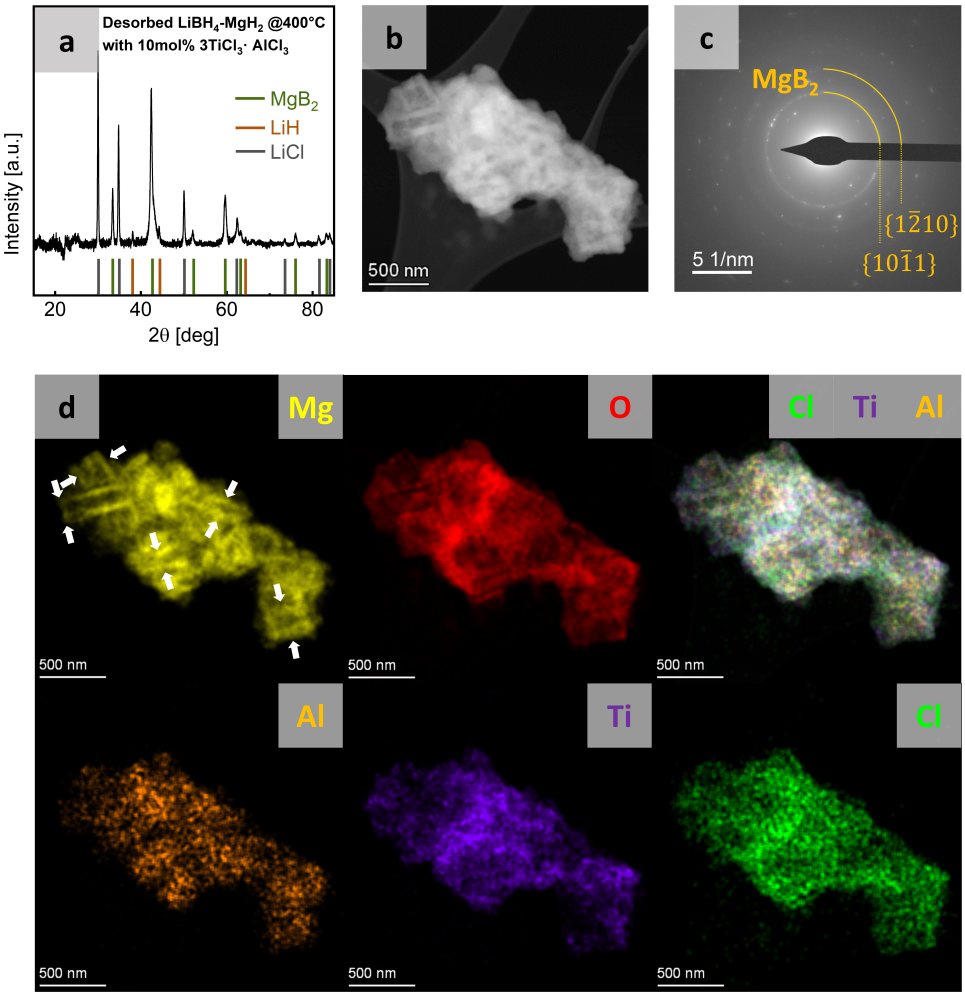

Figure 5.11.: Desorbed $LiBH_4$-MgH_2 with 10 mol% $3TiCl_3{\cdot}AlCl_3$: (a) XRD analysis; (b) a HAADF-STEM image; (c) a diffraction pattern acquired in the corresponding region using a SC of 500 pA and an ET of 8 s; (d) EDXS elemental maps of Mg, O, Al, Ti, and Cl for the same region, generated from integrating 566 frames with a SC of 121 pA, a DT of 13 μs, a PS of 4.63 nm, a CL of 91 mm, and a CA of 30 mrad. The observed parallel-oriented crystals in a smaller size compared to the cases without additives were identified to be MgB_2 crystals. The XRD measurements and phase analyses were performed by Yuanyuan Shang at Hereon. Figure courtesy of [162].

As demonstrated by the EDXS mapping in Figure 5.6d, the distribution of the observed parallel-oriented crystals is found to be aligned with the EDXS map of Mg, as indicated by the arrows. In contrast, there is no correlation observed between the distribution of these parallel-oriented crystals of Mg-containing materials and other elements. Since the only Mg-containing crystal identified through electron diffraction is MgB_2, these parallel-oriented crystals have been

identified as MgB_2. Additionally, based on the respective EDXS elemental maps of Al, Ti, and Cl, no correlation has been observed among the distributions of these elements. Further confirmation is provided by the EDXS quantification presented in Table 5.4. It is evident that the atomic ratio of Al, Ti, and Cl in the local area is approximately 1:2:1, which differs from the initial ratio of 1:3:12 for $3TiCl_3{\cdot}AlCl_3$. Therefore, it is deemed that other materials containing Ti or Al are formed, apart from LiCl, as products of the reaction between $LiBH_4$ and $3TiCl_3{\cdot}AlCl_3$.

Table 5.4.: EDXS quantitative analysis conducted on desorbed $LiBH_4$-MgH_2 with 10 mol% $3TiCl_3{\cdot}AlCl_3$.

Element	Family	Atomic Fraction [at%]
O	K	54.8 ± 4.6
Mg	K	41.4 ± 4.9
Al	K	0.9 ± 0.2
Ti	K	2.1 ± 0.5
Cl	K	0.8 ± 0.2

The morphology of MgB_2 crystals, which may be affected by the addition of $3TiCl_3{\cdot}AlCl_3$, was determined through STEM tomography, as shown in Figure 5.12. During the acquisition process of STEM tomography, an EDXS map of Mg was collected at each tilt angle. The reconstruction of tomography was then based on the collection of these EDXS elemental maps of Mg. Figure 5.12a displays the reconstructed tomographic images with respect to x-, y- and z-directions. The selected piece of MgB_2 crystal highlighted by the squares in Figure 5.12a was picked out for more detailed investigation, as depicted in Figure 5.12b. The crystal structure of MgB_2 with the zone axis $[0\,0\,0\,2]_{MgB_2}$ is schematically illustrated in Figure 5.12c.

In this case, a flat hexagonal platelet-shaped morphology was observed for the MgB_2 crystals, with an aspect ratio of approximately 1 for the basal plane, which is in relation to z- and y-directions. It should be noted that the MgB_2 morphology observed this time differs from the previous case without additives, where rectangular bar-shaped MgB_2 crystals were observed, as shown in Figure 5.5. The thickness of these platelet-shaped MgB_2 crystals was determined to be below 50 nm along the x-direction, as shown in Figure 5.12a. Furthermore, the basal plane can be immediately determined as $\{0\,0\,0\,2\}_{MgB_2}$ by comparing it (Figure 5.12b) with the schematic illustration (Figure 5.12c), considering the crystal structure of hexagonal close-packed (hcp) for MgB_2. In this manner, the six-fold symmetrical surface planes can also be indexed, which are considered to be the primary prism plane $\{1\,0\,\bar{1}\,0\}_{MgB_2}$ or the second prism plane $\{1\,\bar{2}\,1\,0\}_{MgB_2}$.

For a more in-depth investigation of the hexagonal platelet-shaped MgB_2 crystals with a parallel arrangement, EDXS mapping at a higher spatial resolution was conducted, as presented

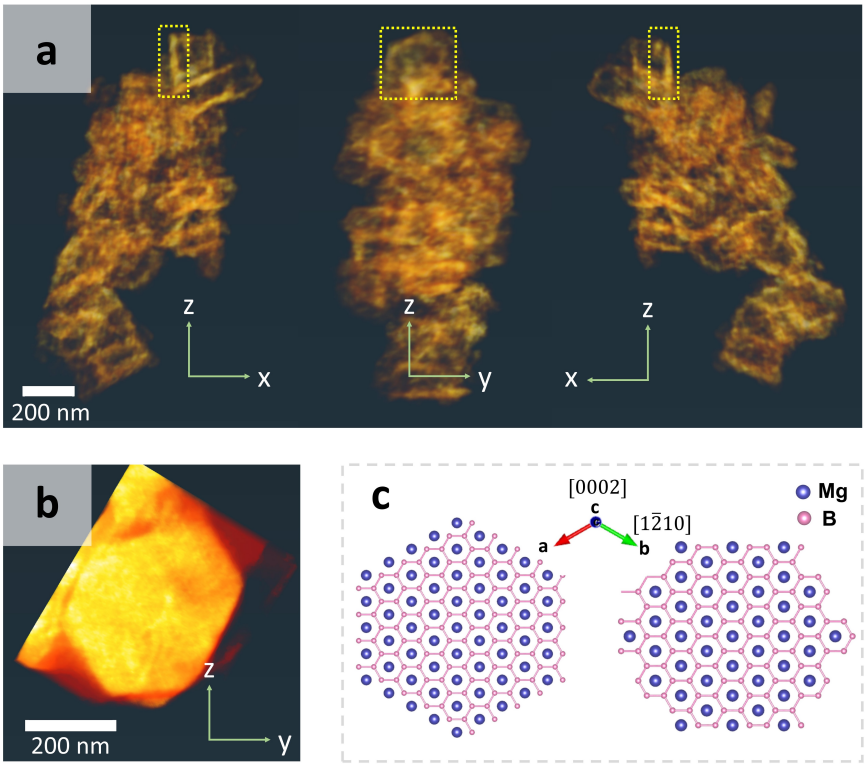

Figure 5.12.: Desorbed $LiBH_4$-MgH_2 with 10 mol% $3TiCl_3 \cdot AlCl_3$: (a) tomographic images extracted from the reconstructed dataset of EDXS map of Mg (K-lines). Each Mg map was generated by integrating 566 frames at each tilt angle with a SC of 90 pA, a DT of 12 μs, a PS of 9.26 nm, a CL of 91 mm, a CA of 8.6 mrad. The tilt angle ranges from -66° to 69° at a step of 3°. The tilt series was aligned by cross-correlation, and the reconstruction algorithm employed is SIRT with 100 iterations; (b) a 3D visualization of the highlighted MgB_2 crystal in subfigure a; (c) a schematic illustration of the crystal orientations of a hexagonal MgB_2 platelet. A hexagonal platelet-shaped morphology was observed for the MgB_2 crystals, when $3TiCl_3 \cdot AlCl_3$ is present. Figure courtesy of [162].

in Figure 5.13a. Based on the EDXS elemental map of Mg, it can be observed that the two parallel crystals are also connected at the bottom, as indicated by the arrows in Mg map of Figure 5.13a. This is consistent with the observation in Figure 5.9d. Ti-containing particles are evenly dispersed over the MgB_2 crystals, as shown in the Ti map of Figure 5.13a. Oxygen appears to be only present as a coating on the surface of MgB_2. The crystal orientations of these crystals were determined using 4D-STEM analysis, as displayed in Figure 5.13b. The diffraction patterns acquired from areas 1-5 in Figure 5.13a are identical, confirming the connection and identical crystal orientation of these two MgB_2 crystals. Importantly, in contrast to the primary growth direction $\{1\,\bar{2}\,1\,0\}$ observed for the bar-shaped MgB_2 crystals related to Mg in Subsections 5.1.2.3 and 5.1.2.4, the crystal orientation perpendicular to the connection position is determined to be

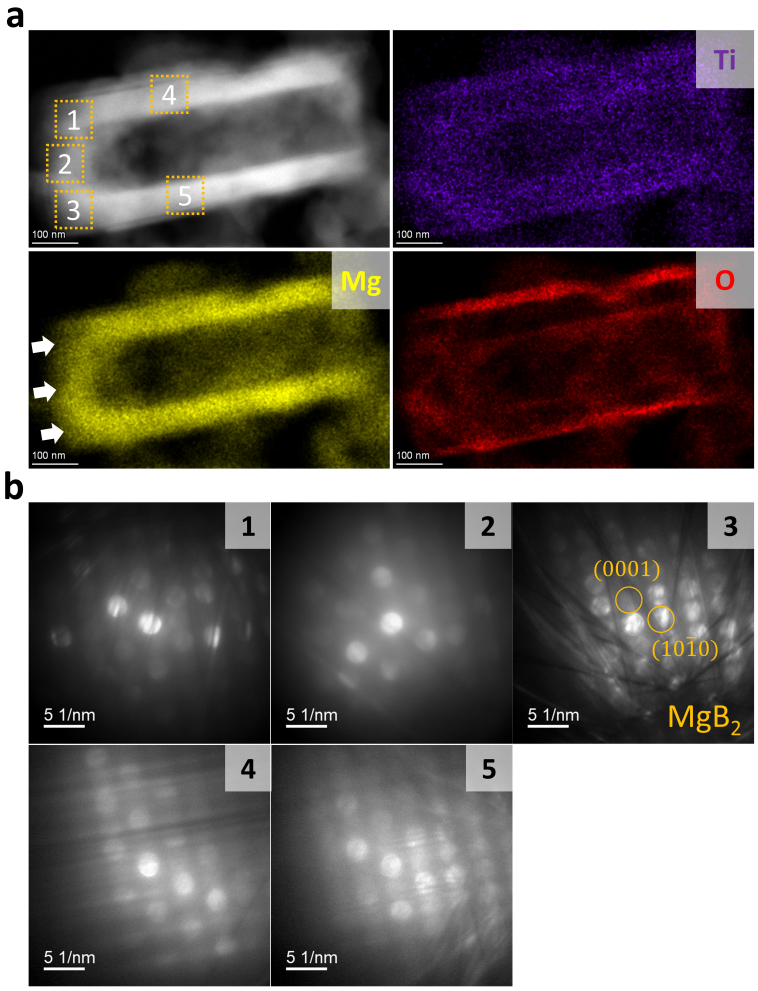

Figure 5.13.: Desorbed $LiBH_4$-MgH_2 with 10 mol% $3TiCl_3 \cdot AlCl_3$: (a) a HAADF-STEM image with the corresponding EDXS elemental maps of Mg, O, and Ti for parallel-oriented crystals, generated from integrating 486 frames with a SC of 160 pA, a DT of 10 μs, a PS of 1.58 nm, a CL of 91 mm, and a CA of 30 mrad. (b) 4D-STEM analysis performed for the same region using a SC of 50 pA, a DT of 100 ms, a PS of 3.9 nm, a CL of 580 mm, and a CA of 1.54 mrad. Identical diffraction patterns were acquired in the selected areas 1-5 in subfigure a, which identified MgB_2.

$\{1\,0\,\bar{1}\,0\}$ for the platelet-shaped MgB_2 crystals related to additives observed here. This finding suggests a crystallographic change in the nucleation and growth characteristics of MgB_2 induced by the presence of additives.

As the addition of $3TiCl_3 \cdot AlCl_3$ led to the formation of a new morphology as well as the crystallographic variation for MgB_2 crystals, the presence of another nucleation center can be

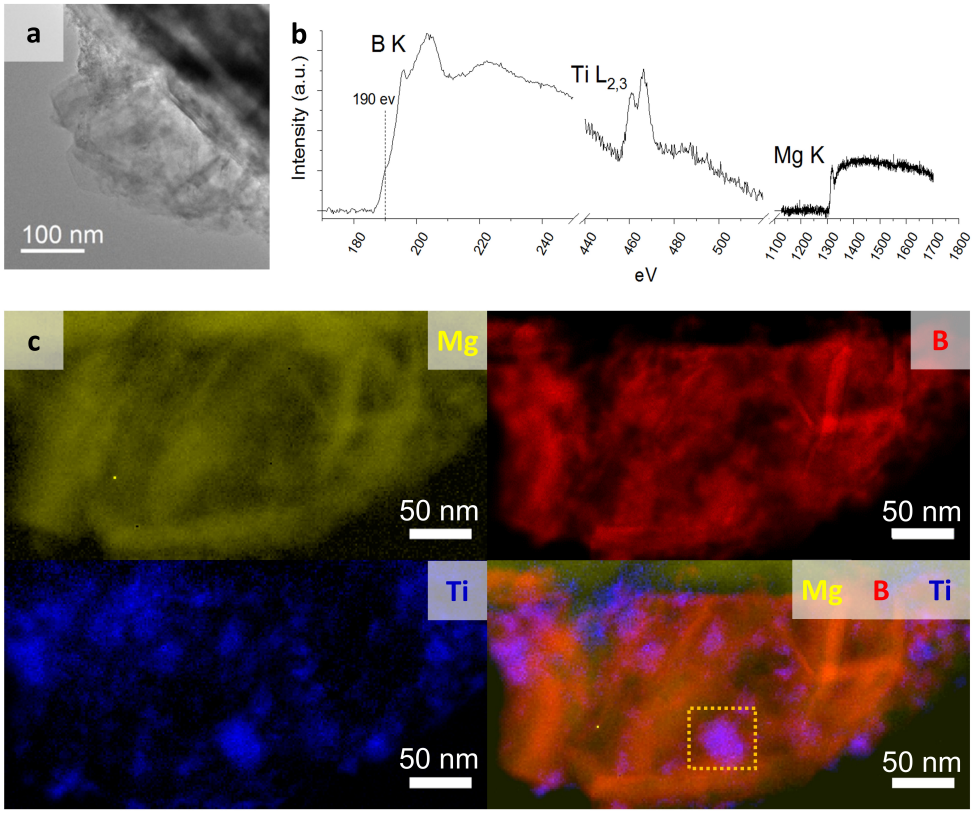

Figure 5.14.: Desorbed $LiBH_4$-MgH_2 with 20 mol% $3TiCl_3 \cdot AlCl_3$: (a) a TEM bright-field image showing the region of interest for EELS mapping; (b) a EELS spectrum showing background-removed Mg K-edge, B K-edge, and Ti $L_{2,3}$-edge; (c) the corresponding EELS elemental maps of Mg, B, and Ti for the same region. The dual mode was utilized for the acquisition using a PS of 1.6 nm, an ET of 0.02 s for high-loss spectrum and 0.005 s for low-loss spectrum, a SC of 145 pA, a CL of 30 mm, a CA of 21.5 mrad and a collection angle of 40 mrad. The dispersion of 0.3 ev/Ch was applied, resulting in a measured energy spread of 2.0 eV. A distributional correlation between boron and titanium was observed, indicating the generation of TiB_2. Figure courtesy of [165].

expected. This new nucleation center was presumed to be a product of the reaction between $3TiCl_3 \cdot AlCl_3$ and $LiBH_4$. To identify this nucleation center, an even higher additive content of 20 mol% $3TiCl_3 \cdot AlCl_3$ was employed. In this case, EELS was utilized instead of EDXS, as EELS allows for the identification of light elements, including boron (B), as shown in Figure 5.14. Figure 5.14a displays the region of interest for EELS mapping in a TEM bright-field image. The EELS spectrum in Figure 5.14b exhibits the background-removed Mg K-edge, B K-edge, and Ti $L_{2,3}$-edge, acquired within the same region. The corresponding EELS elemental maps of Mg, B, and Ti are shown in Figure 5.14c.

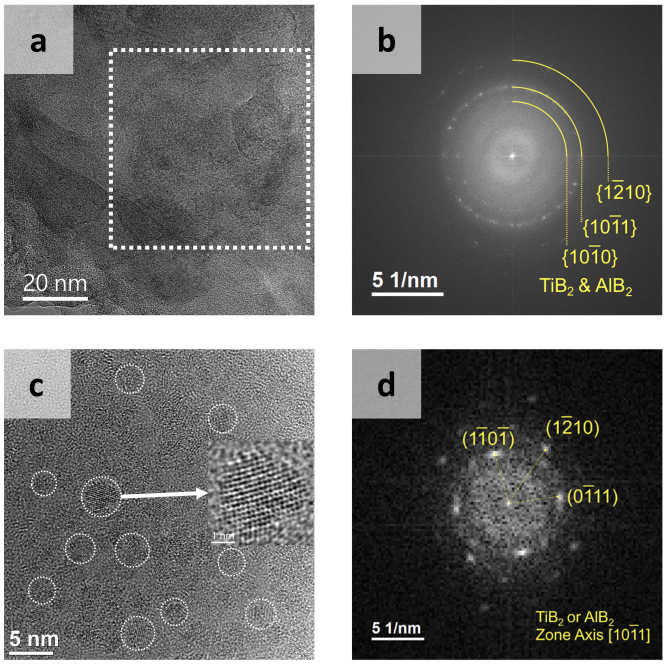

Figure 5.15.: Desorbed $LiBH_4$-MgH_2 with 20 mol% $3TiCl_3 \cdot AlCl_3$: (a) a HRTEM image for the area highlighted in Figure 5.14c; (b) FFT of the highlighted area in subfigure a; As-milled $LiBH_4$-MgH_2 with 20 mol% $3TiCl_3 \cdot AlCl_3$: (c) a HRTEM image of a TiB_2 (or AlB_2) nanoparticles; (d) FFT of the zoomed-in particle in subfigure c. The generation of TiB_2 (and AlB_2) nanoparticles was verified. Figure courtesy of [165].

Based on the EELS mapping, a correlation between the distribution of Mg and B can be determined, confirming the presence of MgB_2 in this region. The pre-peak observed at approximately 190 eV for the B K-edge in the EELS spectrum of Figure 5.14b indicates the high and unfilled p-like density of states of boron, confirming the bonding between Mg and B. Hence, the grains (in orange) depicted in Figure 5.14c represent the distribution of MgB_2. Additionally, a correlation between the distribution of Ti and B was also observed. This is evident from the observation of the purple agglomerates shown in Figure 5.14c, obtained by combining the Boron map in red and the Titanium map in blue. In addition, when comparing the Ti edges in Figure 5.14b with the Ti edges of TiO_2 in Figure A1, the different white-line peaks rule out the oxidation of Ti.

To identify the material containing both Ti and B, HRTEM was employed, as shown in Figure 5.15. The area highlighted by the square in Figure 5.14c was subjected to HRTEM investigation, as shown in Figure 5.15a. The corresponding FFT of the highlighted region in Figure 5.15a is presented in Figure 5.15b. Consequently, the nanoparticles observed in the HRTEM image were identified as TiB_2. It is presumed that AlB_2 may also be present in the same region. However,

due to the fact that both AlB_2 and TiB_2 share the same space group (P6m/mm, No.191) and nearly identical lattice constants, and given the unavailability of the EELS spectrum for Al, AlB_2 cannot be distinguished from TiB_2 in this case.

TiB_2 (and AlB_2) nanoparticles were also observed prior to the dehydrogenation process. Figure 5.15c presents a HRTEM image of $LiBH_4$-MgH_2 with 20 mol% in the as-milled state, revealing the observation of many nanoparticles with an average size of about 3 nm. According to the corresponding FFT of the zoomed-in particle shown in Figure 5.15c, TiB_2 (and possibly AlB_2) was identified, as illustrated in 5.15d. This finding suggests that TiB_2 (and AlB_2) nanoparticles had already formed during the ball milling process. This is further supported by the identification of $LiCl$ through XRD after the ball milling process and prior to dehydrogenation, as illustrated in Figure 5.10a and c.

5.2. MgB_2 Formation for Li-RHC under Different Conditions

In this section, the study will focus on the impact of different variables on the growth of MgB_2 and the kinetics of (de)hydrogenation. The results of kinetics measurements conducted by Yuanyuan Shang at Hereon will be presented in Subsection 5.2.1. The variables of interest, namely additive content, annealing temperature, and cycling effect, will be analyzed in Subsections 5.2.2 through 5.2.4.

5.2.1. Kinetics Measurement

In Figure 5.16, the hydrogen release of Li-RHCs samples in different states during their respective dehydrogenation processes is illustrated. The presented curves depict the hydrogen release of $LiBH_4$-MgH_2 with 1 mol% $3TiCl_3{\cdot}AlCl_3$ desorbed at 400 °C, $LiBH_4$-MgH_2 with 5 mol% $3TiCl_3{\cdot}AlCl_3$ desorbed at 400 °C, $LiBH_4$-MgH_2 without additives desorbed at 420 °C, and LiH-MgB_2 without additives after 10 cycles with a dehydrogenation temperature of 400 °C. Throughout the dehydrogenation process, a hydrogen atmosphere of 0.4 MPa was consistently maintained, with a temperature rate of 10 °C/min. Only the hydrogen release for the 10*th* dehydrogenation of the 10-cycled LiH-MgB_2 is shown in Figure 5.16 for comparison. The hydrogen release curve of $LiBH_4$-MgH_2 without additives desorbed at 400 °C is presented as a reference.

Similar to the previous case of desorbed $LiBH_4$-MgH_2 with 10 mol% $3TiCl_3{\cdot}AlCl_3$ shown in Figure 5.1, the addition of 1 or 5 mol% $3TiCl_3{\cdot}AlCl_3$ also resulted in the elimination of the incubation plateau, as shown in Figure 5.16. This indicates an acceleration in the heterogeneous nucleation of MgB_2 crystals. The reduction in hydrogen storage capacity can be attributed to the presence of additives. Increasing the annealing temperature from 400 °C to 420 °C significantly reduced the duration of the incubation plateau from about 8 hours to about 5 hours, although it has not been completely eliminated. This suggests that the constrained nucleation of MgB_2 based on Mg was partially alleviated at a higher annealing temperature. Remarkably, the elimination of the incubation plateau was also observed during the 10*th* dehydrogenation of the 10-cycled LiH-MgB_2 (as shown by the blue curve in Figure 5.16), even in the absence of additives and without the application of a higher annealing temperature.

To understand the cycling effect for Li-RHC, Figure 5.17a and b depict all the hydrogenation and dehydrogenation processes of the 10 cycles for the sample of LiH-MgB_2 without additives. The hydrogenation procedure was carried out at 350 °C with a temperature rate of 10 °C/min under a hydrogen atmosphere of 3 MPa, whereas the dehydrogenation process was conducted at 400

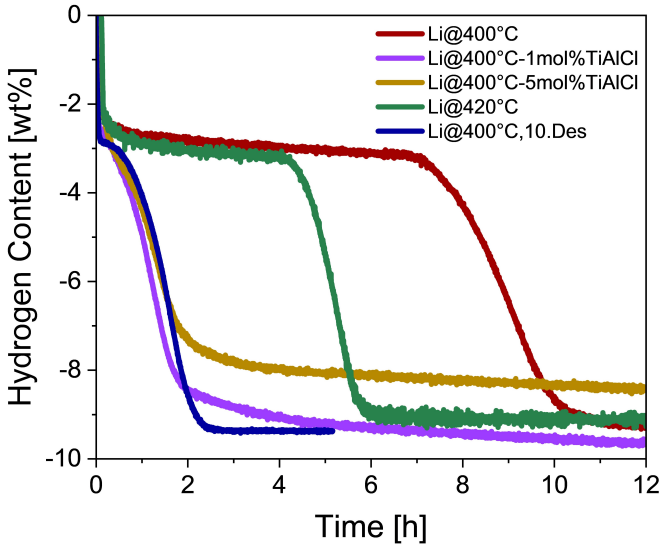

Figure 5.16.: Kinetics measurements conducted during the dehydrogenation of Li-RHCs in different states, suggesting that the kinetics can be tuned by different variables. The kinetics measurements were performed by Yuanyuan Shang at Hereon. Figure courtesy of [162].

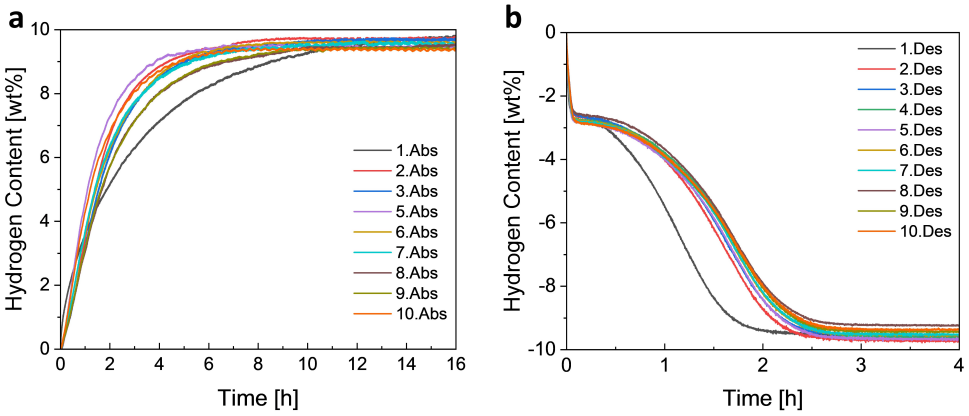

Figure 5.17.: Kinetics measurements during: (a) hydrogenation process for the first 10 cycles of LiH-MgB_2 without additives; (b) dehydrogenation process for the first 10 cycles of LiH-MgB_2 without additives. Although no additives were present, no incubation plateau was observed for dehydrogenation during cycling, suggesting a significant acceleration in MgB_2 nucleation. The kinetics measurements were performed by Yuanyuan Shang at Hereon.

°C with a temperature rate of 10 °C/min under a hydrogen atmosphere of 0.4 MPa. Notably, the 4*th* hydrogenation was not shown in Figure 5.17a due to a technical error during data acquisition. A consistent and stable performance in hydrogen uptake and release was observed throughout

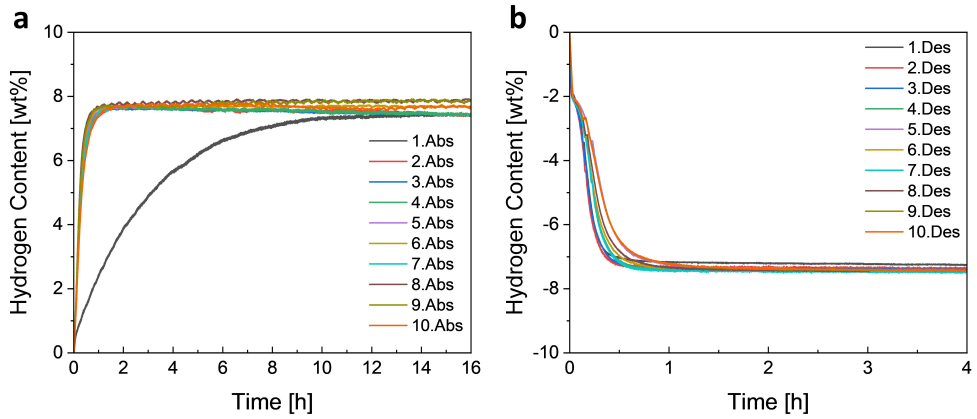

Figure 5.18.: Kinetics measurements during: (a) hydrogenation process for the first 10 cycles of LiH-MgB_2 with 5 mol% $3TiCl_3{\cdot}AlCl_3$; (b) dehydrogenation process for the first 10 cycles of LiH-MgB_2 with 5 mol% $3TiCl_3{\cdot}AlCl_3$. A further improvement in both hydrogenation and dehydrogenation kinetics during cycling was observed by adding additives. The kinetics measurements were performed by Yuanyuan Shang at Hereon.

the entire cycling process, with only slight variations in the slope, particularly during the initial absorption and desorption stages. However, the yield of hydrogen uptake/release remained below 10 wt%, despite the theoretical hydrogen storage capacity being approximately 11.5 wt%. This indicates that the reaction between MgB_2 and LiH has not been completed, implying that some residual MgB_2 and LiH may still be present after each hydrogenation process. Furthermore, no incubation plateau was observed for all the 10 hydrogenation and dehydrogenation processes. In general, it took around 2 hours to release approximately 90% of the hydrogen from the materials, while it took around 4 hours to absorb about 90% of hydrogen. The dehydrogenation kinetics measurement of the cycled $LiBH_4$-MgH_2 contrasts with that of the as-milled $LiBH_4$-MgH_2, as depicted in Figure 5.1, where a plateau width of over 6 hours has been observed.

To investigate the additive effect during cycling, the sample of LiH-MgB_2 with 5 mol% $3TiCl_3{\cdot}AlCl_3$ was subjected to 10 cycles using the same operating conditions as the previous case. The hydrogenation and dehydrogenation processes are illustrated in Figure 5.18a and b. It should be noted that the hydrogen storage capacity, on average, decreases to approximately 8 wt% during the cycling process. This decrease is primarily attributed to the incorporation of additives. On the other hand, the presence of additives was found to have a significant impact on the kinetics of both hydrogenation and dehydrogenation. In general, the time required to achieve 90% hydrogen uptake decreased from approximately 4 hours to less than 1 hour during hydrogenation, while the time required to release 90% of hydrogen decreased from about 2 hours to less than half an hour during dehydrogenation with the introduction of additives. Furthermore, as illustrated in Figure

5.18a, the trajectory of hydrogen uptake demonstrated enhanced consistency for each cycle when additives were introduced, as opposed to the earlier case without additives (Figure 5.17a).

5.2.2. Effect of Additive Content

In contrast to the previously applied 10 mol% $3TiCl_3 \cdot AlCl_3$, smaller additive contents of 1 and 5 mol% $3TiCl_3 \cdot AlCl_3$ were also employed to investigate the influence of the additive content on the size, distribution and morphology of the generated MgB_2 crystals.

5.2.2.1. Addition of 1 mol% Additives

The sample of desorbed $LiBH_4$-MgH_2 with 1 mol% $3TiCl_3 \cdot AlCl_3$ is illustrated in Figure 5.19. The XRD spectrum for the sample is shown in Figure 5.19a. A HAADF-STEM image in a region of interest is presented in Figure 5.19b, while the corresponding electron diffraction pattern acquired locally is displayed in Figure 5.19c. Furthermore, Figure 5.19d shows the corresponding EDXS elemental map depicting the distribution of Mg, O, Ti, and Cl in the same region.

Based on the XRD spectrum, the presence of LiH and MgB_2 was identified, which are the products generated from the dehydrogenation process of $LiBH_4$-MgH_2. Additionally, the detection of $LiCl$ can be attributed to the reaction between $LiBH_4$ and $3TiCl_3 \cdot AlCl_3$, as discussed in Section 5.1.3.2. However, there were also some unknown peaks observed in the XRD pattern. Since these peaks were not observed in desorbed $LiBH_4$-MgH_2 without additives (Figure 5.4a) or desorbed $LiBH_4$-MgH_2 with 10 mol% $3TiCl_3 \cdot AlCl_3$ (Figure 5.11a), they are presumed to be impurities from the raw materials. Regarding the microstructure of the sample, parallel-oriented crystals were observed, as depicted in the HAADF-STEM image in Figure 5.19b. The presence of MgB_2 in the local region was confirmed through electron diffraction, as shown in Figure 5.19c. For further characterization, EDXS elemental maps of Mg, O, Ti, and Cl were acquired for this region, as illustrated in Figure 5.19d. Considering the parallel features displayed in the EDXS elemental map of Mg, it is evident that there was no correlation observed between Mg and other elements. Given that MgB_2 was the only crystal containing Mg determined in this region, the parallel-oriented crystals were attributed to be MgB_2. Moreover, the presence of O in the surrounding area may be attributed to the oxidation of LiH as explained previously in Section 5.1.2.3. Inclusion of EDXS elemental maps of Ti and Cl were also done in this case to confirm the presence of additives or additive-related materials, e.g. TiB_2, in the vicinity of MgB_2 crystals.

For further examination, the parallel-oriented MgB_2 crystals highlighted by the yellow square in Figure 5.19b were selected for STEM tomographic analysis. The two parallel-oriented MgB_2 crystals were then reconstructed and highlighted in blue, as depicted in Figure 5.20. Both the side

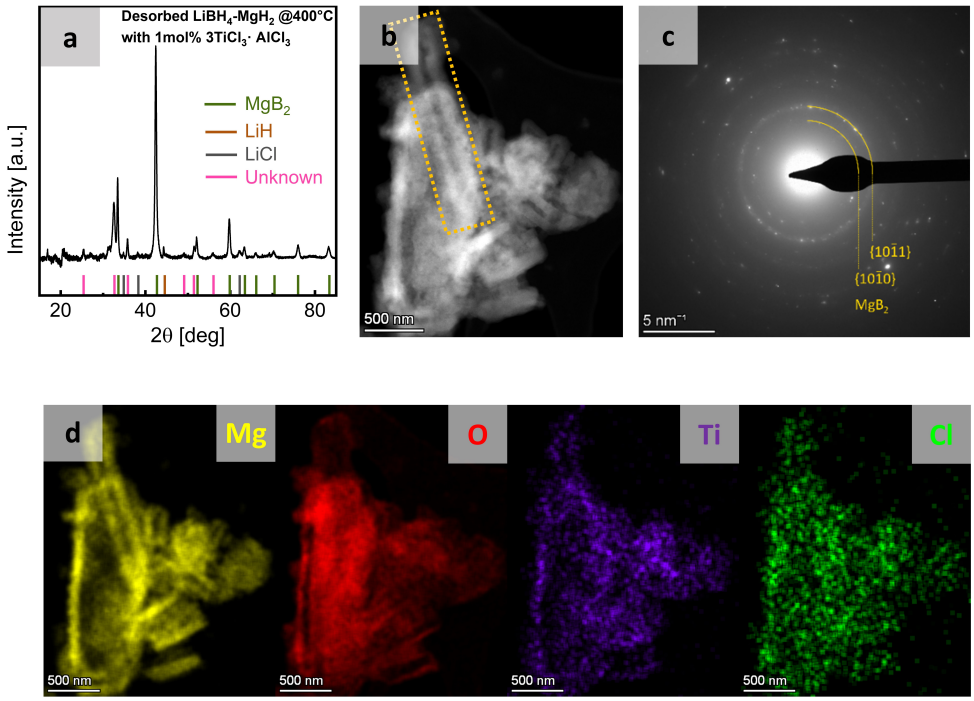

Figure 5.19.: Desorbed $LiBH_4$-MgH_2 with 1 mol% $3TiCl_3{\cdot}AlCl_3$: (a) XRD analysis; (b) a HAADF-STEM image; (c) the corresponding diffraction pattern using a SC of 500 pA and an ET of 8 s; (d) EDXS elemental maps of Mg (K-line), O (K-line), Ti (K-line), and Cl (K-line) for the same region generated by integrating 956 frames using a SC of 144 pA, a DT of 10 μs, a PS of 6.57 nm, a CL of 91 mm, and a CA of 30 mrad. Parallel-oriented MgB_2 crystals were observed for the sample with 1 mol% $3TiCl_3{\cdot}AlCl_3$. The XRD measurements and phase analyses were performed by Yuanyuan Shang at Hereon. Figure courtesy of [162].

view and the top view of the crystals were provided. It can be observed that these two MgB_2 crystals exhibit a rectangular bar-shaped morphology. The size of these MgB_2 crystals was up to several micrometers along the x-direction, with an aspect ratio much larger than 1 for the basal plane in relation to x- and y-direction. According to the prior knowledge gathered from Section 5.1.2, this morphology resulted from the heterogeneous nucleation of MgB_2 on Mg grains.

Furthermore, the microstructure of another region in the sample was also investigated, as presented in Figure 5.21. Figure 5.21a displays a HAADF-STEM image, while Figure 5.21b shows the corresponding EDXS map of Mg. Based on the EDXS map of Mg, the observed parallel-oriented crystals in the HAADF-STEM image can be identified as MgB_2. These MgB_2 crystals typically have a much smaller size, ranging in several hundred nanometers. They are comparable to the ones observed in the sample of desorbed $LiBH_4$-MgH_2 with 10 mol% $3TiCl_3{\cdot}AlCl_3$ (see Figure 5.11), suggesting a platelet-shaped morphology for these MgB_2 crystals.

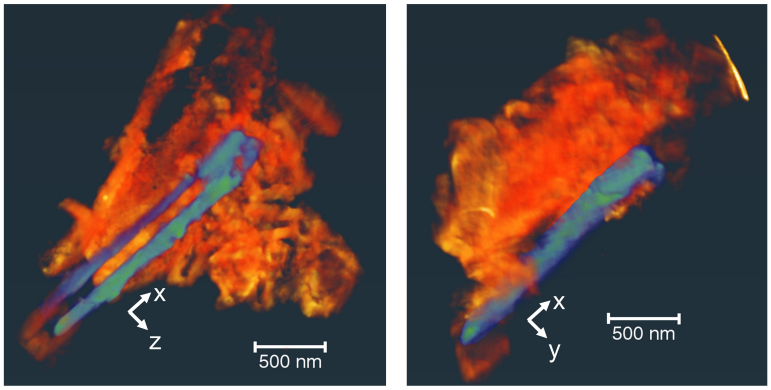

Figure 5.20.: Desorbed $LiBH_4$-MgH_2 with 1 mol% $3TiCl_3 \cdot AlCl_3$: tomographic images from the reconstructed data displayed in different directions. The acquisition was performed using a tilt series from -70° to 70° at a tilt step of 2° with a SC of 144 pA, a DT of 5 μs, a PS of 1.64 nm, a CL of 91 mm, and a CA of 8.6 mrad. The tilt series was then aligned using cross-correlation, and the applied reconstruction algorithm was SIRT with 100 iterations. It shows that rectangular bar-shaped MgB_2 crystals were still observed with 1 mol% $3TiCl_3 \cdot AlCl_3$. Figure courtesy of [162].

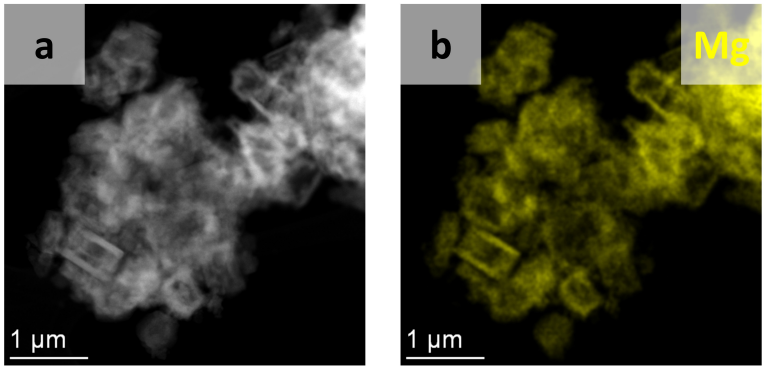

Figure 5.21.: Desorbed $LiBH_4$-MgH_2 with 1 mol% $3TiCl_3 \cdot AlCl_3$: (a) a STEM image acquired in another region; (b) the corresponding EDXS elemental map of Mg using the same parameters for acquisition as Figure 5.19d. It shows that the platelet-shaped MgB_2 crystals were also observed. Figure courtesy of [162].

5.2.2.2. Addition of 5 mol% Additives

The sample of desorbed $LiBH_4$-MgH_2 with 5 mol% $3TiCl_3 \cdot AlCl_3$ was examined, as depicted in Figure 5.22. The XRD spectrum for the entire sample is presented in Figure 5.22a. A HAADF-STEM image recorded in a region of interest is shown in Figure 5.22b. The corresponding electron diffraction pattern acquired locally is displayed in Figure 5.22c. Furthermore, Figure 5.22d exhibits the EDXS elemental map of Mg, O, Ti, and Cl acquired in the region highlighted by the red square in Figure 5.22b.

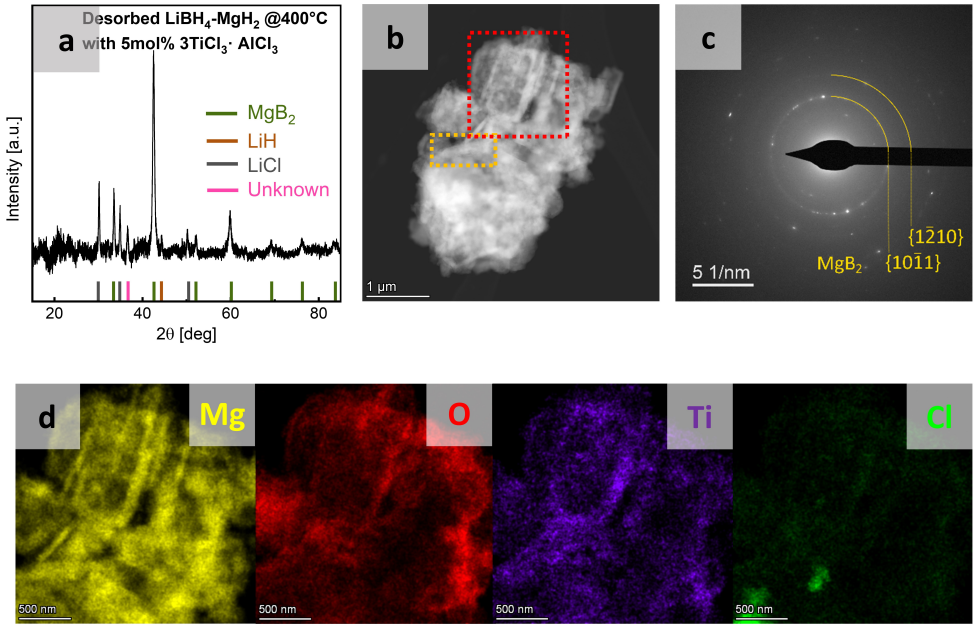

Figure 5.22.: Desorbed $LiBH_4$-MgH_2 with 5 mol% $3TiCl_3 \cdot AlCl_3$: (a) XRD analysis; (b) a HAADF-STEM image; (c) the corresponding diffraction pattern acquired using a SC of 500 pA and an ET of 8 s; (d) EDXS elemental maps of Mg (K-line), O (K-line), Ti (K-line), and Cl (K-line) for the corresponding region in subfigure a, generated by integrating 204 frames, using a SC of 114 pA, a DT of 13 μs, a PS of 4.63 nm, and a CL of 91 mm, and a CA of 30 mrad. It shows that the observed parallel-oriented crystals were identified as MgB_2. The XRD measurements and phase analyses were performed by Yuanyuan Shang at Hereon. Figure courtesy of [162].

Based on the XRD spectrum in Figure 5.22a, the generation of MgB_2 and LiH from the dehydrogenation of $LiBH_4$-MgH_2 was confirmed. The detection of LiCl was attributed to the reaction between $LiBH_4$ and $3TiCl_3 \cdot AlCl_3$. However, some unknown peaks were also detected, which could potentially be attributed to impurities from the raw materials. Parallel-oriented crystals, as depicted in Figure 5.22b, were observed in the HAADF-STEM image. The confirmation of the existence of MgB_2 in the localized region was obtained through electron diffraction, as shown in Figure 5.22c. EDXS mapping was conducted in the region highlighted by the red square in Figure 5.22b, as shown in Figure 5.22d. The correlation between the EDXS elemental map of Mg and the distribution of the parallel-oriented crystals indicated that these crystals represented MgB_2. The detection of oxygen in the surrounding area is again attributed to oxidized LiH, see Section 5.1.2.3. Additionally, almost no correlation was found between the distribution of Ti (purple) and Cl (green) based on their respective EDXS elemental maps. Consequently, the EDXS elemental map of Ti is regarded to correspond to the distribution of TiB_2, while the map of Cl is regarded to correspond to the distribution of LiCl.

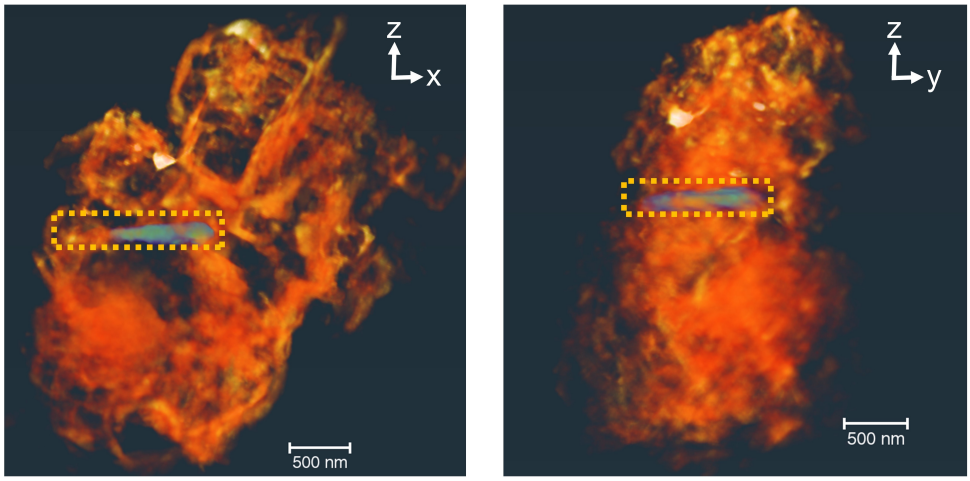

Figure 5.23.: Desorbed $LiBH_4$-MgH_2 with 5 mol% $3TiCl_3 \cdot AlCl_3$: tomographic images from the reconstructed data displayed in different directions. The applied parameters for acquisition include a SC of 114 pA, a DT of 4 μs, a PS of 2.32 nm, a CL of 91 mm, a CA of 8.6 mrad, and a tilt range from -74° to 76° at a tilt step of 2°. The tilt series was aligned by cross-correlation, and the reconstruction utilized SIRT with 100 iterations as the algorithm. The observed parallel-oriented MgB_2 crystals have a platelet-shaped morphology. Figure courtesy of [162].

For further characterization, STEM tomography was conducted for the corresponding region. Figure 5.23 displays the tomographic images taken along different axes. The MgB_2 crystal, which is highlighted by the yellow square in Figure 5.22a, is displayed in blue in Figure 5.23 for further examination. Tilting 90 degrees around the z-axis, the widths of the observed MgB_2 crystal along the x-axis and y-axis were found to be approximately equal. In contrast, the observed thickness along the z-axis was significantly smaller than the other two dimensions. This suggests a platelet-shaped morphology for MgB_2, with an aspect ratio of approximately 1 for the basal plane in relation to the x- and y-direction. Thus, this morphology is considered to be a consequence of the heterogeneous nucleation of MgB_2 on TiB_2 nanoparticles. Additionally, no bar-shaped MgB_2 crystals were observed in this case.

5.2.3. Effect of Temperature

The influence of the applied annealing temperature on the dehydrogenation kinetics is another variable of interest. As shown in Figure 5.16, an increase in temperature from 400 °C to 420 °C resulted in a significant reduction in the duration of the incubation plateau. This observation indicates an acceleration of the nucleation process for MgB_2. Therefore, it is also crucial to investigate the microstructure of the MgB_2 crystals in the $LiBH_4$-MgH_2 sample desorbed at

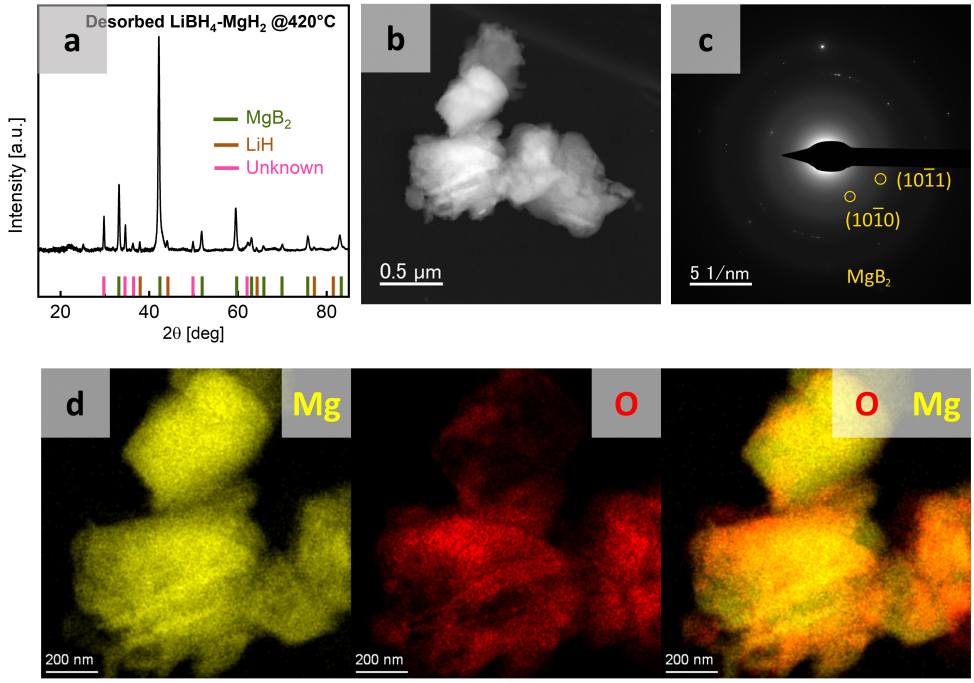

Figure 5.24.: $LiBH_4$-MgH_2 desorbed at 420 °C without additives: (a) XRD analysis; (b) a HAADF-STEM image; (c) a diffraction pattern acquired in the corresponding area using a SC of 500 pA and an ET of 32 s; (d) EDXS elemental maps of Mg (K-line) and O (K-line) acquired for the corresponding region in subfigure a, generated by integrating 844 frames with a SC of 146 pA, a DT of 10 μs, a PS of 2.32 nm, a CL of 91 mm, and a CA of 30 mrad. Parallel-oriented MgB_2 crystals were observed after dehydrogenating at 420 °C. The XRD measurements and phase analyses were performed by Yuanyuan Shang at Hereon.

420 °C without additives. The XRD analysis performed for the sample is presented in Figure 5.24a. Figure 5.24b displays a HAADF-STEM image obtained from a specific region of interest. In the same region, an electron diffraction pattern was acquired and is shown in Figure 5.24c. Furthermore, Figure 5.24d exhibits the corresponding EDXS elemental map of Mg and O for the same region.

The existence of MgB_2 and LiH was confirmed based on the XRD spectrum depicted in Figure 5.24a, indicating the successful reaction between $LiBH_4$ and Mg at 420 °C. However, the detection of unknown peaks suggests the possibility of by-products generated from side reactions, given the higher dehydrogenation temperature applied in this case, as introduced in Figure 2.2. The presence of parallel-oriented crystals was observed in the HAADF-STEM image displayed in Figure 5.24b. The presence of MgB_2 in the local region was confirmed through the electron diffraction pattern, as shown in Figure 5.24c. Furthermore, EDXS mapping was performed for the same region, as illustrated in Figure 5.24d. The distribution of the observed parallel-oriented

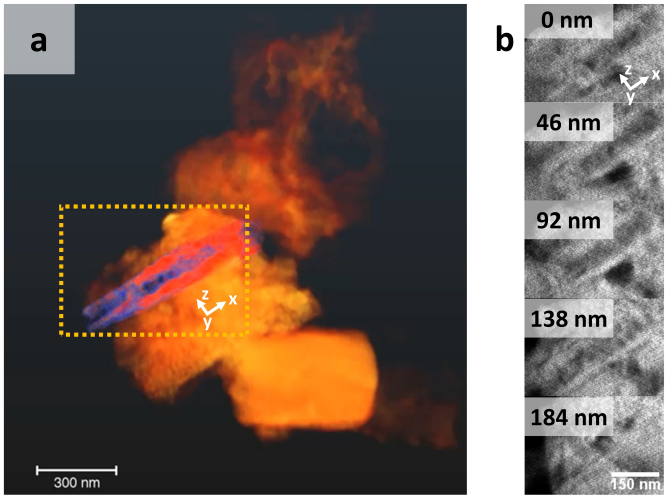

Figure 5.25.: $LiBH_4$-MgH_2 desorbed at 420 °C without additives: (a) a tomographic image from the reconstructed dataset acquired in the same region using a SC of 146 pA, a DT of 3 μs, a PS of 1.16 nm, a CL of 91 mm, a CA of 8.6 mrad, and a tilt series ranging from -72° to 72° at a tilt step of 2°. The alignment of the tilt series was made using cross-correlation, and the reconstruction algorithm utilized was SIRT, with 100 iterations; (b) orthoslices for the area highlighted by the yellow dashed lines in subfigure a. The displayed orthoslices have a depth ranging from 0 to 184 nm at a step of 46 nm. The tomography of the observed MgB_2 crystals were determined to be platelet-shaped rather than bar-shaped.

crystals aligns with the EDXS elemental map of Mg. Therefore, these crystals were identified as MgB_2 crystals. However, it is evident that the MgB_2 crystals generated at a higher annealing temperature of 420 °C exhibit noticeable differences compared to those formed at the lower annealing temperature of 400 °C, as illustrated in Figure 5.4.

To enhance the comprehension of the MgB_2 morphology in this scenario, STEM tomography was utilized on the same region, as depicted in Figure 5.25. Figure 5.25a presents a tomographic image derived from the reconstructed dataset. The yellow square highlights two parallel-oriented MgB_2 crystals that were chosen for further examination, which are displayed in blue for clarity. Figure 5.25b presents the corresponding orthoslices for the selected region, displaying a depth (measured in the y-direction) range from 0 nm to 184 nm at intervals of 46 nm. An aspect ratio of approximately 3 is estimated for the basal plane of the MgB_2 crystals relative to the x- and y-directions. Moreover, the observed crystals demonstrate a platelet-shaped morphology, which is attributed to their comparatively small thickness (measured in the z-direction) compared to their depth and width. It is worth noting that the platelet-shaped morphology of the MgB_2 crystals is distinctively formed after dehydrogenation at 420 °C, in contrast to the bar-shaped morphology observed after dehydrogenation at 400 °C.

5.2.4. Effect of Cycling

The influence of cycling was examined by studying the microstructure of the resulting MgB_2 crystals. Both the as-milled and cycled states of LiH-MgB_2 were investigated.

5.2.4.1. As-Milled State

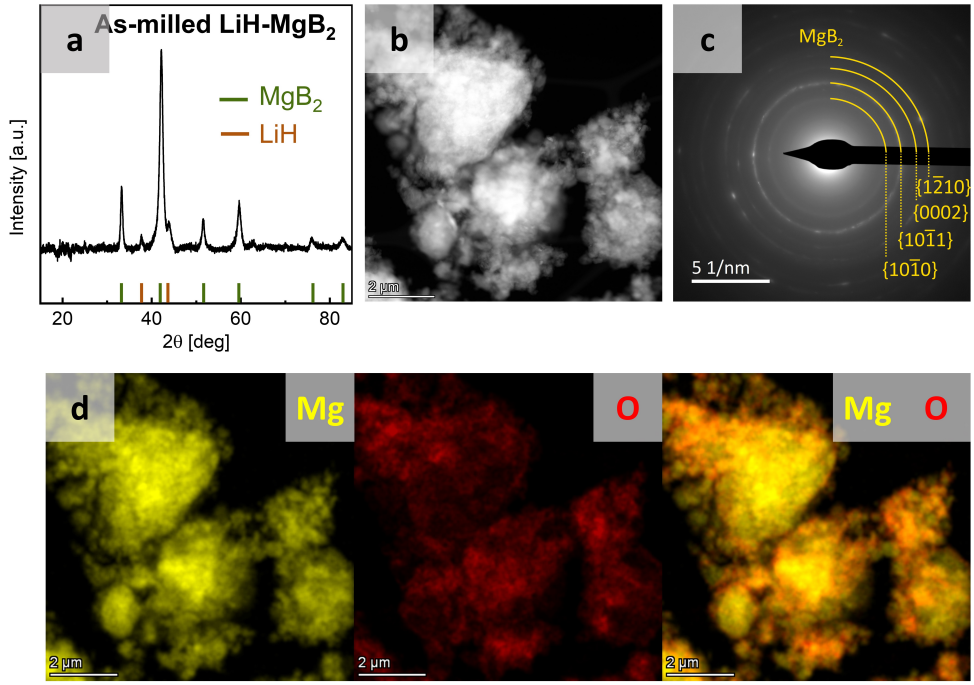

Figure 5.26.: As-milled LiH-MgB_2: (a) XRD analysis; (b) a HAADF-STEM image; (c) a diffraction pattern obtained for the corresponding area of 2.27 μm × 2.27 μm utilizing a SC of 40 pA and an ET of 60 s, leading to an electron dose of about 29 $e^-/Å^2$; (d) EDXS elemental maps of Mg (K-line) and O (K-line) for the same region, generated by integrating 344 frames with a SC of 144 pA, a DT of 10 μs, a PS of 17.98 nm, a CL of 91 mm, and a CA of 30 mrad. The distribution and morphology of MgB_2 grains in the as-milled state was illustrated. The XRD measurements and phase analyses were performed by Yuanyuan Shang at Hereon.

The relevant results for the sample of as-milled LiH-MgB_2 are depicted in Figure 5.26. The XRD spectrum recorded for the sample is presented in Figure 5.26a. Figure 5.26b displays a HAADF-STEM image obtained from a region of interest. The corresponding electron diffraction pattern acquired in the same region is shown in Figure 5.26c. Furthermore, Figure 5.26d exhibits the corresponding EDXS elemental map of Mg and O for the same region.

According to the XRD spectrum presented in Figure 5.26a, MgB_2 and LiH were identified as expected in the as-milled LiH-MgB_2 sample. The size and distribution of the sample was visualized in the HAADF-STEM image of Figure 5.26b. The existence of MgB_2 was determined by the diffraction pattern obtained from the same region. LiH was not detected. This absence can be attributed to the oxidation of LiH rather than electron beam damage, considering that only a low electron dose of down to 29 $e^-/Å^2$ was applied in this case.

Figure 5.26d exhibits the EDXS elemental map of Mg and O. With respect to the distribution of the large grains shown in the EDXS elemental map of Mg, there is no correlation between the distribution of Mg and O. Thus, the EDXS elemental map of Mg can be considered as the distribution of MgB_2 crystals, while the EDXS elemental map of O may indicate the distribution of oxidized LiH. It is important to note that the observed morphology of MgB_2 in the as-milled state differs from the morphology of MgB_2 in the desorbed state, as there have been no observations of parallel-oriented crystals in this case.

5.2.4.2. Cycled State

To investigate the changes in MgB_2 microstructure resulting from cycling, the sample of 10-cycled LiH-MgB_2 was examined as depicted in Figure 5.27. The XRD spectrum encompassing the entire sample is presented in Figure 5.27a. Figure 5.27b displays a HAADF-STEM image obtained from a region of interest. The corresponding electron diffraction pattern obtained from the same region is shown in Figure 5.27c. Additionally, Figure 5.27d exhibits the EDXS elemental map of Mg and O for the region highlighted by the yellow square in Figure 5.27b.

As displayed in the XRD spectrum of Figure 5.27a, in addition to the expected identification of MgB_2 and LiH, the presence of Mg was detected. This indicates an incomplete reaction between $LiBH_4$ and Mg during cycling. Furthermore, the morphological differences between the materials after cycling, as shown in the HAADF-STEM image in Figure 5.27b, and the as-milled state (see Figure 5.26b) are evident. The diffraction pattern displayed in Figure 5.27c identified not only MgB_2 but also MgO. Considering the identification of Mg by XRD, the detection of MgO by electron diffraction suggests the oxidation of Mg. This oxidation may occur during the transportation of the materials or during the investigation within the TEM column. In order to differentiate the distribution of MgB_2 and MgO, EDXS mapping was conducted in the corresponding region, as shown in Figure 5.27d. By comparing the EDXS elemental map of Mg and O, it is possible to determine the distribution of MgB_2 crystals. Consequently, the observed hexagonal-shaped crystals correspond to MgB_2, which have emerged after cycling.

A deeper understanding of the morphology of these MgB_2 crystals was achieved through STEM tomography, as depicted in Figure 5.28. The entire region shown in Figure 5.27b was

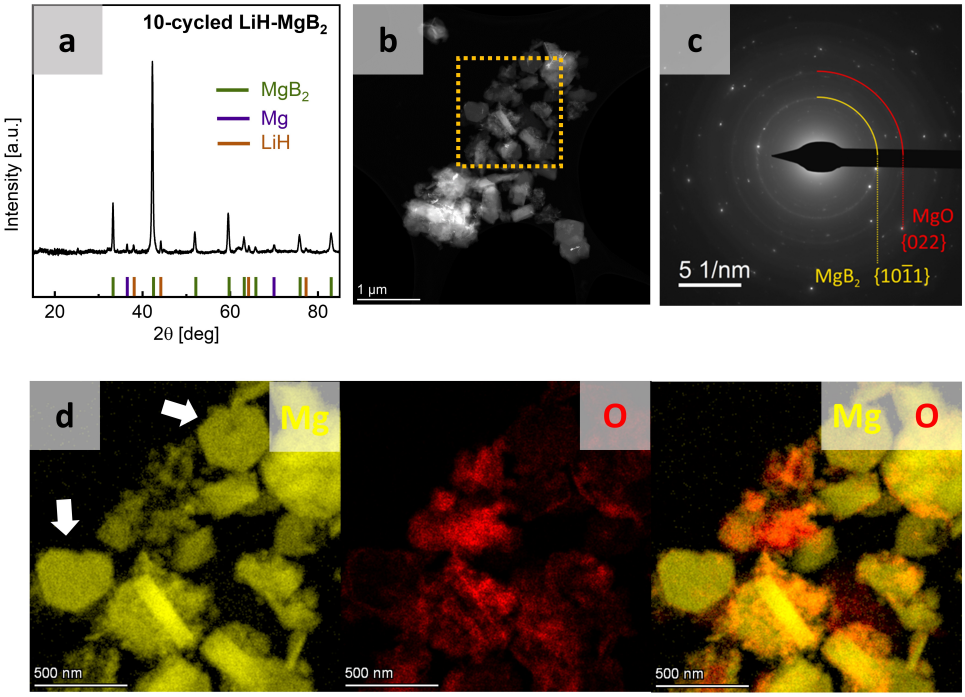

Figure 5.27.: 10-cycled LiH-MgB_2: (a) XRD analysis; (b) a HAADF-STEM image; (c) a diffraction pattern acquired using a SC of 500 pA and an ET of 16 s; (d) EDXS elemental maps of Mg (K-line) and O (K-line) for the area highlighted in subfigure a, generated by integrating 750 frames using a SC of 196 pA, a DT of 10 μs, a PS of 3.27 nm, a CL of 91 mm, and a CA of 30 mrad. A change in the distribution and morphology of MgB_2 was observed after cycling, compared to the initial as-milled state. The XRD measurements and phase analyses were performed by Yuanyuan Shang at Hereon.

subjected to reconstruction and post-processing by volume rendering, as displayed in Figure 5.28a. For clarity, two representative MgB_2 crystals, labeled as 1 and 2, were selected. Figure 5.28b and c present the respective top and side views of these crystals. The observations reveal a hexagonal platelet-shaped morphology for the MgB_2 crystals after cycling.

The crystal orientations in relation to the hexagonal platelet-shaped MgB_2 crystals were determined through the 4D-STEM analysis presented in Figure 5.29. Figure 5.29a illustrates the region of interest where diffraction patterns were collected for each pixel. Two MgB_2 crystals, labeled as 1 and 2, were selected for further analysis. Their respective diffraction patterns and corresponding virtual images are displayed in Figure 5.29b and c. The virtual images were acquired by mapping the diffraction spots $(\bar{1}\,\bar{1}\,2\,0)_{MgB_2}$ and $(0\,0\,0\,2)_{MgB_2}$ from the respective diffraction patterns. As shown in Figure 5.29b, the zone axis of the hexagonal platelet-shaped MgB_2 crystal selected was identified as $[0\,0\,0\,2]_{MgB_2}$. Based on its morphology, the six-fold symmetric facets can be indexed as $\{1\,0\,\bar{1}\,0\}_{MgB_2}$. Figure 5.29c indicates that the thickness of these MgB_2 crystals,

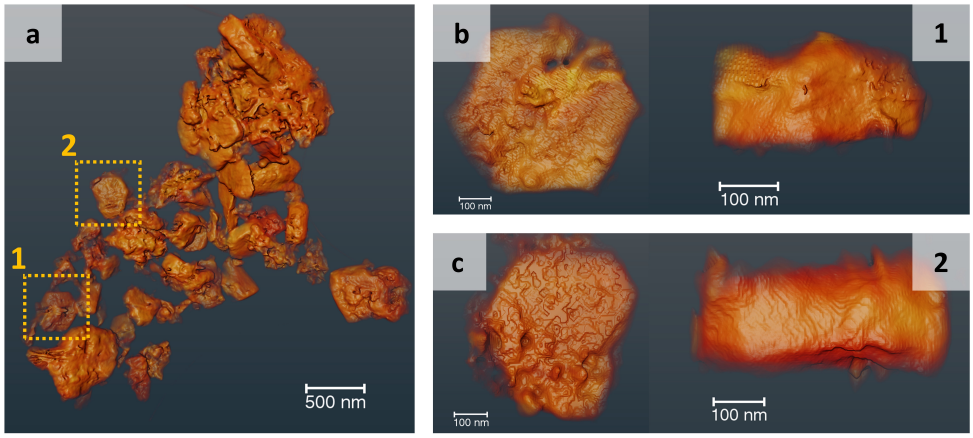

Figure 5.28.: 10-cycled LiH-MgB_2 without additives: (a) a volume rendering from tomographic reconstruction of the region shown in Figure 5.27a. The STEM tomography was performed using a SC of 196 pA, a DT of 3 μs, and a PS of 1.95 nm. The CL was set to 91 mm, the CA was 8.6 mrad, and the tilt range angles range from -68° to 62°, with a tilt step of 2°. The tilt series was aligned using cross-correlation, and the reconstruction algorithm adopted was SIRT with 100 iterations; (b-c) surface renderings of the crystals labeled as 1 and 2 highlighted in subfigure a, providing top and side views. A hexagonal platelet-shape morphology was determined for MgB_2 crystals after cycling.

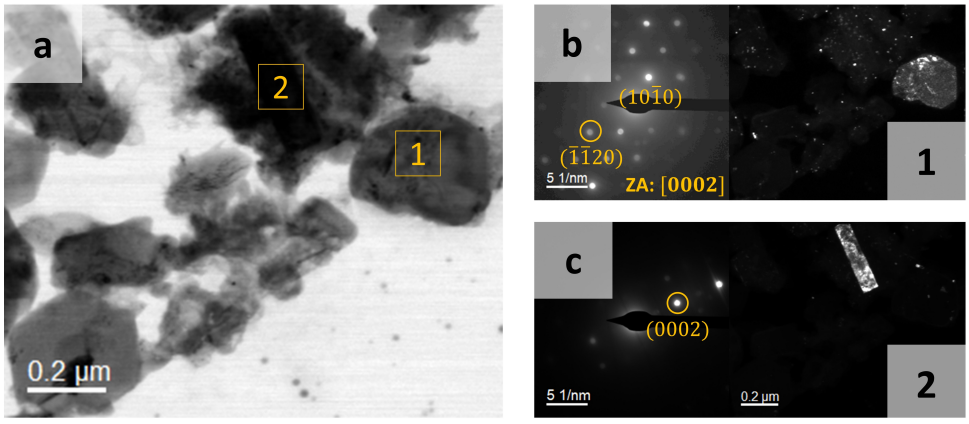

Figure 5.29.: 10-cycled LiH-MgB_2 without additives: (a) a STEM bright-field image acquired for 4D-STEM. The 4D-STEM was performed utilizing a SC of 500 pA, a DT of 20 ms, a PS of 4.20 nm, a CL of 720 mm, and a CA of 1.1 mrad; (b-c) diffraction patterns acquired in the area 1 and 2 highlighted in subfigure a, with the corresponding distribution of MgB_2 crystals mapped by the selected diffraction spots $(\bar{1}\,\bar{1}\,2\,0)$ and $(0\,0\,0\,2)$, respectively. The crystal orientations with respect to the hexagonal platelet-shaped morphology for MgB_2 crystals were determined. The cases influenced by cycling and additives were both observed to have similarities and differences in terms of the generated MgB_2 crystals.

measured along the c-axis $[0\,0\,0\,2]_{MgB_2}$, ranges from 100 nm to 200 nm. It is noteworthy that the morphology and crystal orientations determined for the MgB_2 crystals in this case are consistent

with those in the case where additives are present, as discussed in Section 5.1.3.2. However, despite having similar-sized hexagonal basal planes, approximately 300 nm to 500 nm, the MgB_2 crystals observed after cycling have a thickness of up to 200 nm, whereas the thickness observed in the case with additives generally remains below 50 nm, see Section 5.1.3.2.

5.3. Investigation on Na-RHC

The study of $NaBH_4$-MgH_2 was also conducted in order to examine the extent to which the knowledge obtained from Li-RHCs can be applied to other reactive hydride composites. Due to the lower required back-pressure for the dehydrogenation of $NaBH_4$-MgH_2, it allows for the in-situ TEM investigation of $NaBH_4$-MgH_2, which may yield new insights into the system of reactive hydride composites. Kinetics measurements for the relevant samples can be found in Subsection 5.3.1. The investigation of $NaBH_4$-MgH_2 was carried out using both ex-situ and in-situ experimental methods, as described in Subsections 5.3.2 and 5.3.4, respectively.

5.3.1. Kinetics Measurement

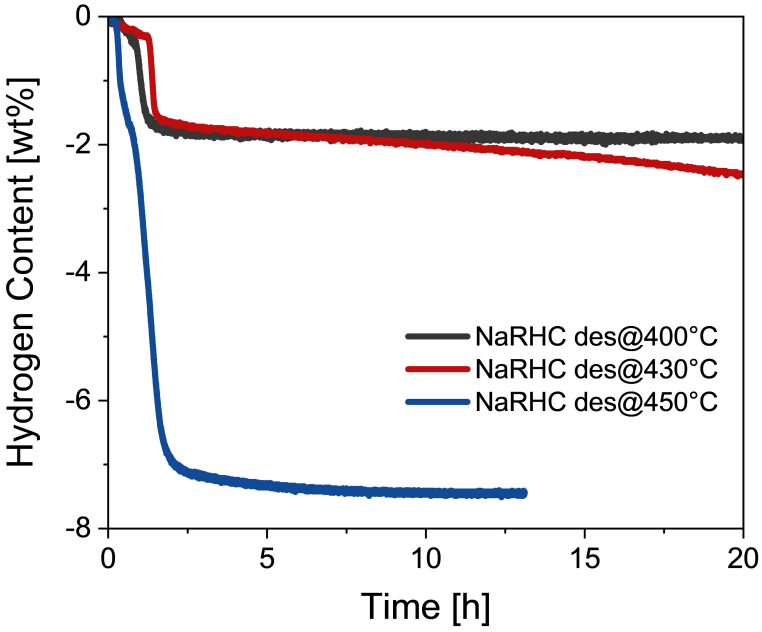

Figure 5.30.: Kinetics measurements of $NaBH_4$-MgH_2 desorbed at 400, 430 and 450 °C. Even after 20 hours of annealing at 400 or 430 °C, the dehydrogenation process was not completed. However, upon increasing the temperature to 450 °C, the dehydrogenation process was completed within 5 hours. The kinetics measurements were performed by Yuanyuan Shang at Hereon.

Figure 5.30 depicts the monitoring of hydrogen release from samples of $NaBH_4$ desorbed under a hydrogen atmosphere of 0.015 MPa, with temperature rates of 3 °C/min at 400 °C, 430 °C, and 450 °C. It was observed that even after maintaining the annealing temperature of 400

°C for over 20 hours, no further hydrogen release occurred beyond the decomposition of MgH_2 (the first step of dehydrogenation). This indicates a significant restriction on the kinetics of the reaction between $NaBH_4$ and Mg (the second step of dehydrogenation). Although the hydrogen release from the second step of dehydrogenation became noticeable upon increasing the annealing temperature to 430 °C, the reaction proceeded slowly. Even after 20 hours, less than 3 wt%H_2 was released. However, by further increasing the annealing temperature to 450 °C, the incubation plateau nearly disappeared, and approximately 90% of the hydrogen was released within about three hours. This suggests that the heterogeneous nucleation of MgB_2 was significantly enhanced at higher annealing temperatures, in agreement with the observations for Li-RHCs.

5.3.2. Ex-situ Analysis

5.3.2.1. As-Milled State

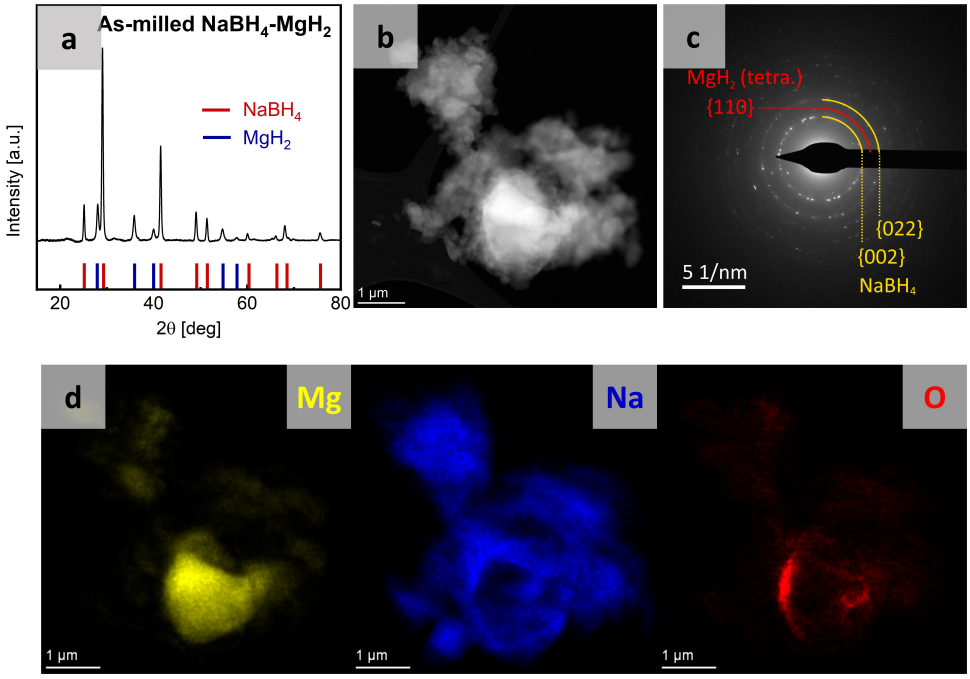

Figure 5.31.: As-milled $NaBH_4$-MgH_2 without additives: (a) XRD analysis; (b) a HAADF-STEM image; (c) a diffraction pattern obtained from the recorded area of 2.68 μm × 2.68 μm using an ET of 40 s and a SC of 30 pA, leading to an electron dose of roughly 10 $e^-/Å^2$; (d) EDXS elemental maps of Mg (K-line), Na (K-line) and O (K-line) for the same region, generated by integrating 928 frames with a DT of 10 μs, a SC of 158 pA, a PS of 12.71 nm, a CL of 91 mm, and a CA of 30 mrad. The XRD measurements and phase analyses were performed by Yuanyuan Shang at Hereon.

The sample of as-milled $NaBH_4$-MgH_2 without additives served as reference for studying Na-RHC. The XRD spectrum acquired for the entire sample is presented in Figure 5.31a. Figure 5.31b shows a HAADF-STEM image obtained from a region of interest. The corresponding electron diffraction pattern acquired in the same region is depicted in Figure 5.31c. Additionally, Figure 5.31d displays the corresponding EDXS elemental map of Mg, Na, and O for the same region.

$NaBH_4$ and MgH_2 in the as-milled state of $NaBH_4$-MgH_2 were identified as indicated by the XRD in Figure 5.31a. The morphology and distribution of the sample was observed in the HAADF-STEM image shown in Figure 5.31b. The existence of $NaBH_4$ and MgH_2 was confirmed based on the corresponding diffraction pattern acquired in the same region. The detection of $NaBH_4$ suggests that $NaBH_4$ is more resilient to oxidation and beam damage compared to $LiBH_4$.

To discern the distribution of MgH_2 and $NaBH_4$, EDXS mapping was conducted. The distribution of MgH_2 and $NaBH_4$ can be represented by the EDXS elemental map of Mg and Na, respectively. The observed regions with high contrast correspond to MgH_2, while the agglomerates with low contrast correspond to $NaBH_4$ in the surrounding area. Furthermore, the oxidation of either MgH_2 or $NaBH_4$ is negligible as indicated by the EDXS map of O.

5.3.2.2. Desorbed State

As evident from Figure 5.30, only the dehydrogenation process at 450 °C was fully accomplished for $NaBH_4$-MgH_2. Consequently, the investigation was focused solely on the MgB_2 microstructure of $NaBH_4$-MgH_2 desorbed at 450 °C, as presented in Figure 5.32. The XRD spectrum for the entire sample is depicted in Figure 5.32a. Figure 5.32b displays a HAADF-STEM image acquired from a region of interest. The corresponding electron diffraction pattern obtained from the same region is presented in Figure 5.32c. Additionally, Figure 5.32d exhibits the EDXS elemental map of Mg, Na, and O for the region highlighted by the yellow square in Figure 5.32b, while Table 5.5 outlines the corresponding EDXS quantification.

The XRD spectrum in Figure 5.32a identified the components MgB_2 and NaH generated from the dehydrogenation process of $NaBH_4$-MgH_2. However, the detection of $NaBH_4$ and Na was unexpected. The existence of $NaBH_4$ suggests that the reaction between $NaBH_4$ and Mg was incomplete. Furthermore, the generation of Na indicates a further decomposition of NaH into Na and H_2. This decomposition might be triggered by the high temperature (> 425 °C), see Figure 2.5. Although a large yield of greater than 7.5 wt% for hydrogen release has been achieved, a part of the released hydrogen may be from the partial decomposition of NaH. The decomposition of NaH is detrimental to the reversibility of $NaBH_4$-MgH_2. As shown in Figure

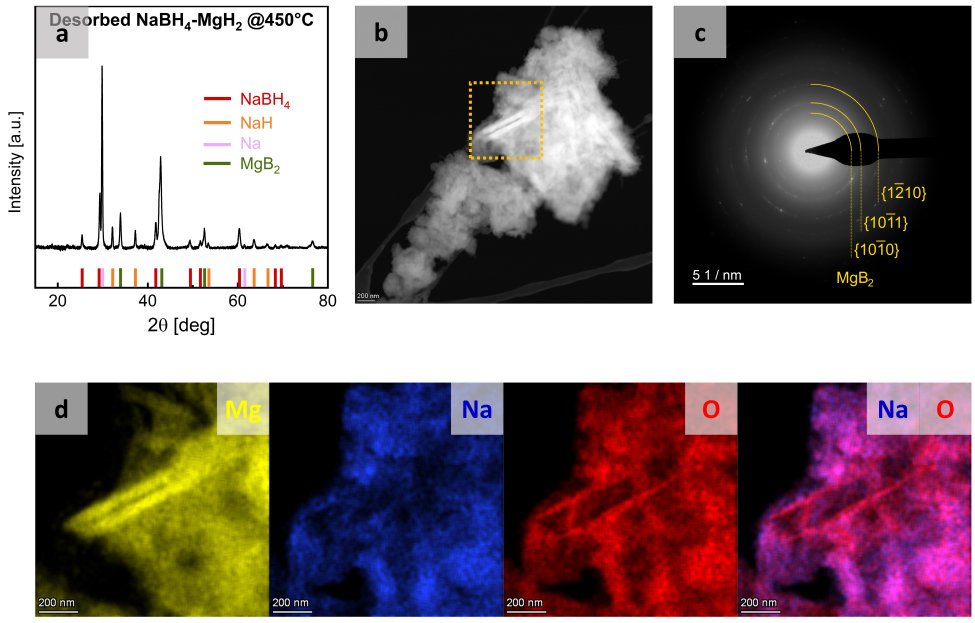

Figure 5.32.: $NaBH_4$-MgH_2 desorbed at 450 °C without additives: (a) XRD analysis; (b) a HAADF-STEM image showing the region of interest; (c) EDXS elemental maps of Mg (K-line), Na (K-line) and O (K-line) for the corresponding region, generated using 349 frames with a SC of 106 pA, a DT of 8 μs, a PS of 2.32 nm, a CL of 91 mm, and a CA of 30 mrad. Parallel-oriented MgB_2 crystals were observed after the dehydrogenation process of $NaBH_4$-MgH_2 at 450 °C. However, both $NaBH_4$ and Na were unexpectedly identified, indicating an incomplete reaction between $NaBH_4$ and Mg, and the decomposition of NaH. The XRD measurements and phase analyses were performed by Yuanyuan Shang at Hereon.

5.32b, parallel-oriented crystals were also observed. According to the corresponding diffraction pattern in Figure 5.32c, the existence of MgB_2 in the local region was confirmed. However, other materials detected by XRD were not detected by electron diffraction. The absence of $NaBH_4$ can be attributed to the inhomogeneous distribution of the residual $NaBH_4$, so they were detected globally (by XRD) but not locally (by electron diffraction). As for NaH and Na, they were very likely oxidized due to the presence of oxygen in the TEM column.

For further characterization, EDXS elemental maps of Mg, Na, and O were collected, as illustrated in Figure 5.32d. According to the EDXS map of Mg, the observed parallel-oriented crystals were confirmed to be MgB_2. On the other hand, a correlation between the distribution of Na and O was also observed, indicating the oxidation of Na-containing materials in this region. As shown in Table 5.5, EDXS quantitative analysis was also conducted in the same region. Up to 40 at% oxygen was detected in this region, verifying the oxidation of Na and/or NaH.

The crystal orientation of the observed MgB_2 crystals was determined by implementing 4D-STEM, as demonstrated in Figure 5.33. Figure 5.33a illustrates the region where data was

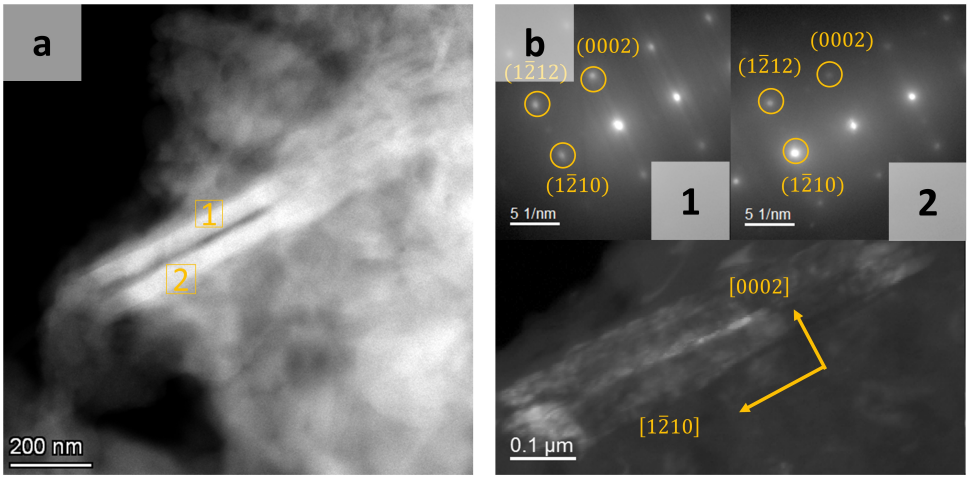

Figure 5.33.: Desorbed $NaBH_4$-MgH_2 without additives: (a) a HAADF-STEM image showing the acquisition area for 4D-STEM. The 4D-STEM analysis was performed using a SC of 500 pA, a DT of 100 ms, a PS of 2.6 nm, a CL of 720 mm, and a CA of 1.1 mrad; (b) diffraction patterns acquired in the area 1 and 2 highlighted in subfigure a, with the corresponding distribution of MgB_2 crystals mapped by the selected diffraction spots $(1\,\bar{2}\,1\,0)$, $(1\,\bar{2}\,1\,2)$ and $(0\,0\,0\,2)$. A spatial and crystallographic parallelism was observed for the observed MgB_2 crystals.

Table 5.5.: EDXS quantitative analysis conducted on desorbed $NaBH_4$-MgH_2 without additives, indicating a oxidation of Na-containing materials.

Element	Family	Atomic Fraction [at%]
O	K	38.0 ± 3.7
Mg	K	13.9 ± 2.8
Na	K	48.1 ± 5.2

collected. Figure 5.33b presents the diffraction patterns recorded within the highlighted areas 1 and 2 in Figure 5.33a, along with the corresponding virtual image generated by mapping the selected diffraction spots. It turns out that both MgB_2 crystals exhibited identical diffraction patterns, indicating spatial and crystallographic parallelism between them. Furthermore, this parallelism was verified by virtually mapping the distribution of the MgB_2 crystals. The diffraction spots $(1\,\bar{2}\,1\,0)$, $(1\,\bar{2}\,1\,2)$, and $(0\,0\,0\,2)$ were selected for the mapping collectively. As a result of overlapping diffraction spots between the both diffraction patterns, both parallel-oriented MgB_2 crystals were consistently simultaneously mapped.

To determine the morphology of MgB_2, STEM tomography was conducted for the entire region depicted in Figure 5.32b. A STEM tomographic image extracted from the reconstructed dataset was presented in Figure 5.34a, with parallel-oriented MgB_2 crystals highlighted in blue.

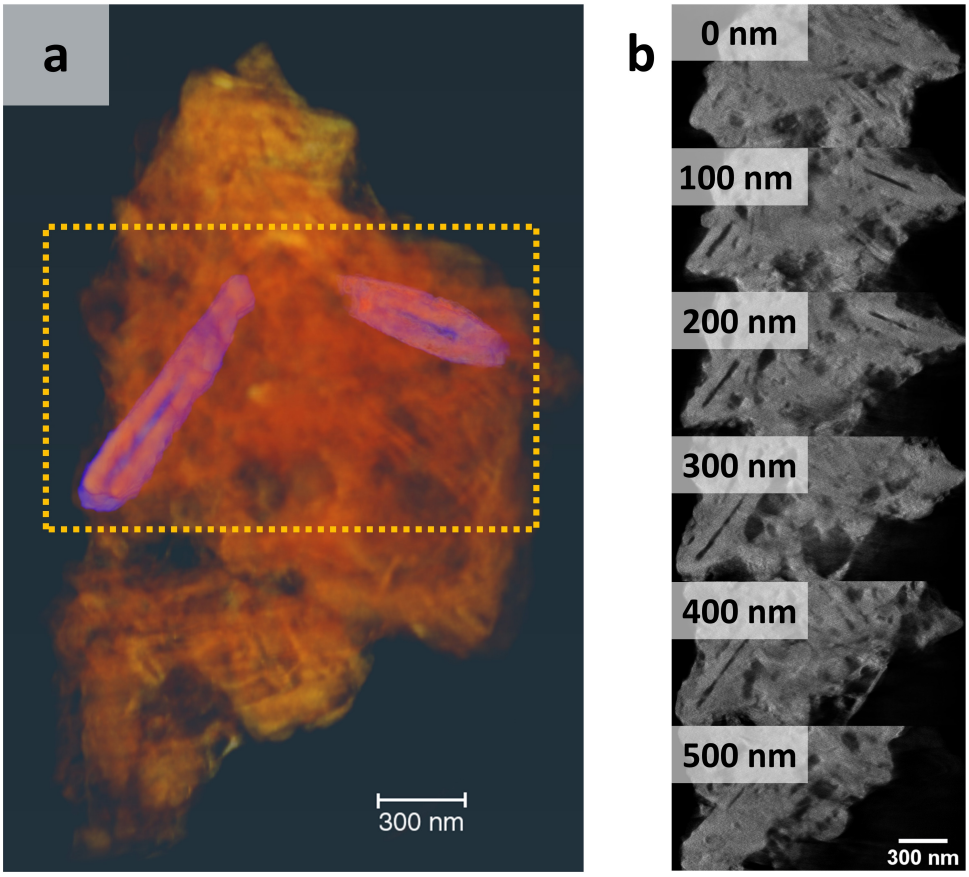

Figure 5.34.: Desorbed $NaBH_4$-MgH_2 without additives: (a) a tomographic image from the reconstructed dataset acquired in the same region using a SC of 106 pA, a DT of 5 μs, a PS of 1.62 nm, a CL of 91 mm, a CA of 8.6 mrad, and a tilt series ranging from -74° to 70° at a tilt step of 2°. Cross-correlation was applied for the alignment of the tilt angle series, and SIRT was applied for reconstruction using 100 iterations; (b) orthoslices for the area highlighted by the yellow dashed lines in subfigure a. The displayed orthoslices have a depth ranging from 0 to 500 nm at a step of 100 nm. A platelet-shaped morphology was observed for the MgB_2 crystals generated after the dehydrogenation process of $NaBH_4$-MgH_2, which was similar to the previous observations with $LiBH_4$-MgH_2.

Due to the agglomeration of the materials, the MgB_2 crystals could not be well separated from the agglomeration. As a result, orthoslices were employed to determine the morphology for this sample. The corresponding orthoslices of the region highlighted by the yellow square in Figure 5.34a were featured in Figure 5.34b, spanning a depth range of 0 to 500 nm at intervals of 100 nm. It was observed that the width of the MgB_2 crystals observed in Figure 5.34a was comparable to the depth observed in Figure 5.34b. An aspect ratio close to 2 for the basal plane of the MgB_2 crystals can be thus estimated. In contrast, the thickness was comparatively smaller. These observations

indicates a platelet-shaped morphology for MgB_2 crystals formed from the dehydrogenation of $NaBH_4$-MgH_2 at 450 °C. Furthermore, this morphology was analogous to the MgB_2 crystals generated after the dehydrogenation of $LiBH_4$-MgH_2 at 420 °C, as illustrated in Figure 5.25.

5.3.3. Beam Sensitivity

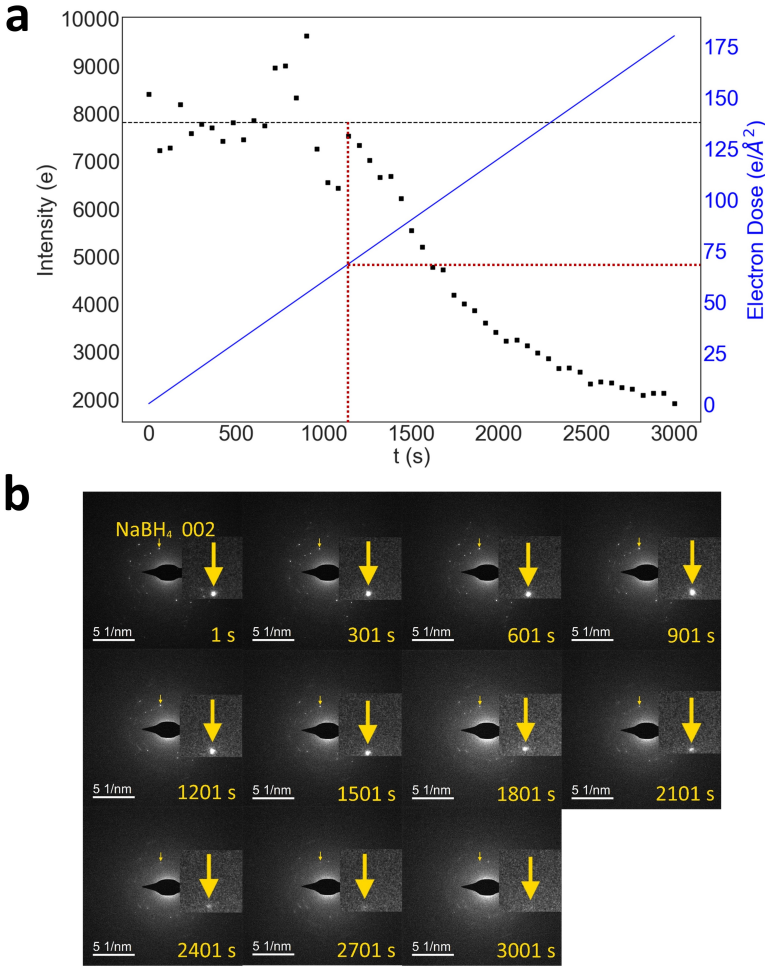

Figure 5.35.: Beam sensitivity test conducted on as-milled $NaBH_4$-MgH_2: (a) the intensity change of the diffraction spot $(0\,0\,2)_{NaBH_4}$ over time while being exposed to electron beam illumination; (b) the diffraction pattern displayed at 300-second interval, highlighting the diffraction spot $(0\,0\,2)_{NaBH_4}$ under continuous investigation. At room temperature, it was discovered that an electron dose of approximately 70 $e^-/Å^2$ triggers the destruction of $NaBH_4$, as indicated by the red lines.

Understanding a material's tolerance to electron beam is of importance, particularly when conducting in-situ TEM investigations. Since Mg is resilient to electron beam, the beam sensitivity of $NaBH_4$ was examined and evaluated in the TEM mode at room temperature, as shown in Figure 5.35. A region of interest, measuring 1.80 μm $\times$ 1.80 μm and housing $NaBH_4$, was subjected to electron beam illumination with a low beam current of 3.1 pA. The diffraction pattern was captured every second, enabling almost continuous monitoring of the intensity change in the diffraction spot $(0\,0\,2)_{NaBH_4}$. Since approximately 1.95×10^7 electrons per second can be collected by the camera, the electron dose rate is approximately 0.06 $e^-/(s \cdot Å^2)$.

Figure 5.35a illustrates the intensity change in the $(0\,0\,2)_{NaBH_4}$ diffraction spot plotted at 60-second intervals. The corresponding electron dose, calculated based on the determined electron dose rate of 0.06 $e^-/(s \cdot Å^2)$, is represented by a blue straight line. To visualize the time-dependent behavior of the intensity change in the $(0\,0\,2)_{NaBH_4}$ diffraction spot, Figure 5.35b shows the diffraction patterns recorded at intervals of 300 s.

As shown in Figure 5.35a, over the course of the initial 1000 seconds of investigation, the intensity of the diffraction spot $(0\,0\,2)_{NaBH_4}$ exhibited fluctuations around 8000 e^-, signifying the tolerability of $NaBH_4$ to electron beam illumination at an electron dose of 70 $e^-/Å^2$, as indicated by the red lines. As time progressed, a gradual decline in intensity became apparent. Notably, after 3000 seconds of illumination, corresponding to an electron dose of approximately 180 $e^-/Å^2$, the $(0\,0\,2)_{NaBH_4}$ diffraction spot became nearly imperceptible, as illustrated in Figure 5.35b. The observed intensity plateau around 2000 e^- can be attributed to the background. It can be thus inferred that $NaBH_4$ was completely disrupted by the electron beam. By considering the intensity thresholds of 8000 e^- and 2000 e^-, it can be determined that approximately 50% of $NaBH_4$ was damaged when the intensity decreased to 2000 e^- after being illuminated for 1500 seconds. This corresponds to an electron dose of around 90 $e^-/Å^2$.

5.3.4. In-situ Analysis

5.3.4.1. In-situ Investigation under 0.015 MPa H_2

An investigation on the change of as-milled $NaBH_4$-MgH_2 during the dehydrogenation process was carried out using the in-situ gas system, see Figure 4.2d. The same pressure of 0.015 MPa H_2 and the same annealing temperature of 450 °C, which were used for the kinetics measurements in Figure 5.30, was also applied in this case for the in-situ experiments.

Figure 5.36 illustrates the EDXS mapping of $NaBH_4$-MgH_2 throughout the annealing process. As shown in Figure 5.36a, EDXS elemental maps of Mg, Na, and O, along with the corresponding HAADF-STEM image (4 rows), were recorded for the three states of interest (3

columns): before heating at room temperature, after increasing the annealing temperature to 450 °C, and after maintaining the isothermal condition at 450 °C for 30 min. Considering the tolerance of $NaBH_4$ to the electron beam, as discussed in Section 5.3.3, the use of an electron dose of approximately 8 $e^-/Å^2$ for each acquisition of EDXS mapping at room temperature should not be detrimental to $NaBH_4$. The EDXS map mixed of Mg (yellow), Na (blue), and O (red) of the corresponding states is shown in Figure 5.36b.

The EDXS maps acquired prior to elevating the temperature are presented in the first column of Figure 5.36a. Afterwards, the pressure was set to 0.015 MPa H_2, and the temperature was increased from room temperature (RT) to 450 °C at a rate of 30 °C/s. The EDXS maps in the second column were recorded at this stage. The entire system was then held isothermally at 450 °C for 30 min. Following this, the EDXS maps in the last column were acquired. Throughout the entire experiment, the materials were well-protected by blanking the electron beam, except during the acquisition of EDXS mapping.

Table 5.6.: EDXS quantitative analysis of as-milled $NaBH_4$-MgH_2 during the in-situ dehydrogenation process at 0.015 MPa H_2.

	Atomic Fraction [at%]		
Element	**RT**	**450 °C**	**450 °C for 30 min**
O	5.8 ± 0.7	21.8 ± 2.3	22.5 ± 2.5
Mg	17.4 ± 3.5	16.6 ± 3.2	16.0 ± 3.2
Na	23.7 ± 4.5	13.3 ± 2.7	8.2 ± 1.8
Si	53.2 ± 5.8	48.4 ± 5.3	53.2 ± 5.3

As depicted in Figure 5.36b, there is almost no correlation between O and either Mg or Na at room temperature, which is evident from the absence of visible orange regions in the mixed EDXS maps. This is consistent with the previous ex-situ investigation on as-milled $NaBH_4$-MgH_2 in Figure 5.31. This finding excludes the possibility of the relevant materials undergoing oxidation before annealing. Therefore, the EDXS elemental maps of Mg and Na can directly represent the distribution of MgH_2 and $NaBH_4$ in this case, respectively. Upon raising the annealing temperature to 450 °C, the morphology of the materials underwent significant changes, as evident from the corresponding EDXS elemental maps in Figure 5.36b. A hollow structure emerged for Mg as highlighted by the arrows, indicating the oxidation of Mg during annealing [169]. The formation of the hollow structure is attributed to the Kirkendall effect [170]. According to this phenomenon, the differential mobilities of Mg moving in and out of the particles lead to the

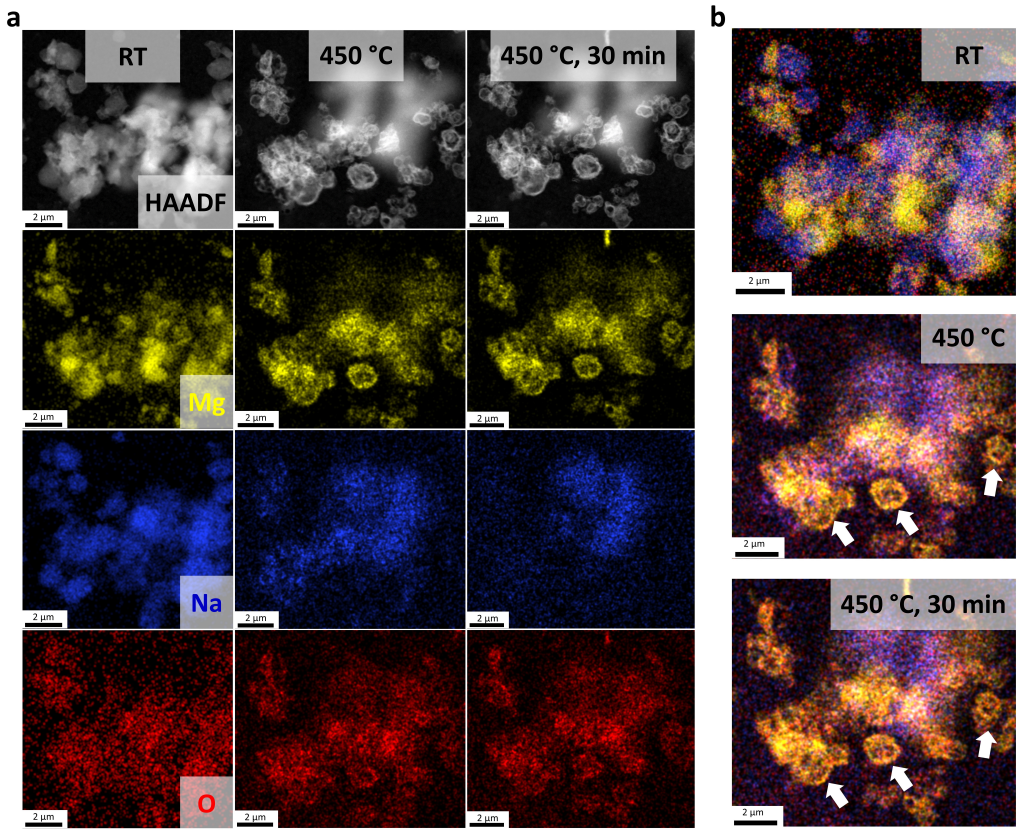

Figure 5.36.: (a) in-situ Investigation on as-milled $NaBH_4$-MgH_2 during the dehydrogenation process under pressure of 0.015 MPa H_2, relying on the in-situ gas system. EDXS mapping was carried out for the respective states: at room temperature before heating, after the annealing temperature was increased to 450 °C, and after keeping the isothermal condition at 450 °C for 30 min. The STEM EDXS maps of Mg (K-line), Na (K-line) and O (K-line) were generated by 100 frames using a DT of 20 μs, a SC of 80 pA, a PS of 37.19 nm, a CL of 91 nn, and a CA of 30 mrad, delivering an electron dose of about 8 $e^-/Å^2$ for each acquisition. The reaction between $NaBH_4$ and Mg did not occur, which was presumably attributed to the oxidation of generated Mg grains. (b) the corresponding EDXS map mixed of Mg (yellow), Na (blue), and O (red) of the corresponding states.

generation and aggregation of vacancies, thereby resulting in a nanohole at the center of the particles. The presence of orange regions signifies the correlation between the distribution of Mg and O at this temperature, thereby confirming the occurrence of oxidation. This was not observed prior to annealing. The detection of MgO seems to indicate the occurrence of the first step of dehydrogenation, namely the decomposition of MgH_2. However, it appears that the generated Mg crystals were subsequently oxidized during annealing. Similarly, the distribution of Na exhibited significant changes after reaching a temperature of 450 °C. Furthermore, the intensity of Na significantly decreased after annealing, indicating a considerable loss of $NaBH_4$

from the investigated region. Following an isothermal condition of 450 °C for an additional 30 minutes, the amount of Na in this region continued to decline, as indicated by the diminishing blue contrast shown in Figure 5.36b. In contrast, no noticeable changes were observed in the distribution of Mg and O. Based on these observations, it can be inferred that the second step of dehydrogenation, namely the reaction between $NaBH_4$ and Mg, did not occur despite employing the same operating conditions of annealing temperature and H_2 pressure utilized in the kinetic measurements. This is presumably attributed to the oxidation of Mg and the loss in $NaBH_4$.

Table 5.6 presents the results of EDXS quantitative analysis, which was conducted to assess the changes in the elemental quantities during the annealing process. In this case, Si from the substrate (silicon nitride E-chip) was included as a reference. To ensure consistency in the captured elemental quantities of Si across all three cases, comparable regions of the same area were selected for the EDXS quantification. By comparing their atomic fractions with that of Si, which remained constant, the actual changes in the elemental quantities of Na, Mg, and O in the local area could be determined. It is evident that the Mg-to-Si ratio remained constant at approximately 1:3 throughout all three stages, indicating no significant variation in the Mg elemental quantity during the investigation. In contrast, the O-to-Si ratio increased from 1:10 at the first stage of room temperature to approximately 1:2 in the subsequent two stages. On the contrary, the Na-to-Si ratio decreased from 1:2 at the first stage of room temperature to around 1:4 when the temperature was elevated to 450 °C. A further decrease in the Na-to-Si ratio to about 1:7 was observed after maintaining the temperature for an additional 30 minutes. These changes signify a decrease in the elemental quantity of Na and an increase in the elemental quantity of O during the annealing process.

The loss of Na can primarily be attributed to the flow of melted $NaBH_4$ away from the local region under investigation, considering its melting point of approximately 400 °C. Alternatively, the possibility of $NaBH_4$ evaporation or $NaBH_4$ degradation into volatile Na-species caused by beam damage during such a high-temperature annealing process cannot be disregarded, as it may also lead to a significant loss of Na. The increase in O could potentially be attributed to the oxidation of Mg, which is supported by the observed correlation between the distribution of Mg and O after the temperature was raised to 450 °C. Consequently, the oxidation may be ascribed to the presence of oxygen in the tiny cell formed by the two E-chips. Therefore, the exclusion of oxygen may be essential for the successful occurrence of the reaction between $NaBH_4$ and Mg.

5.3.4.2. In-situ Investigation under 0.1 MPa H_2

To mitigate the oxidation of Mg, a higher pressure of 0.1 MPa H_2 was applied for another in-situ TEM investigation using the in-situ gas system, see Figure 4.2d. A related measurement sequence

is depicted in Figure 5.37. The EDXS mapping was performed solely at the conclusion of the experiment to minimize the possible damage induced by the electron beam. Throughout the experiment, solely HAADF-STEM images were recorded, resulting in an electron dose of 0.28 $e^-/Å^2$ per acquisition, with a total of approximately 2 $e^-/Å^2$ except for the EDXS mapping.

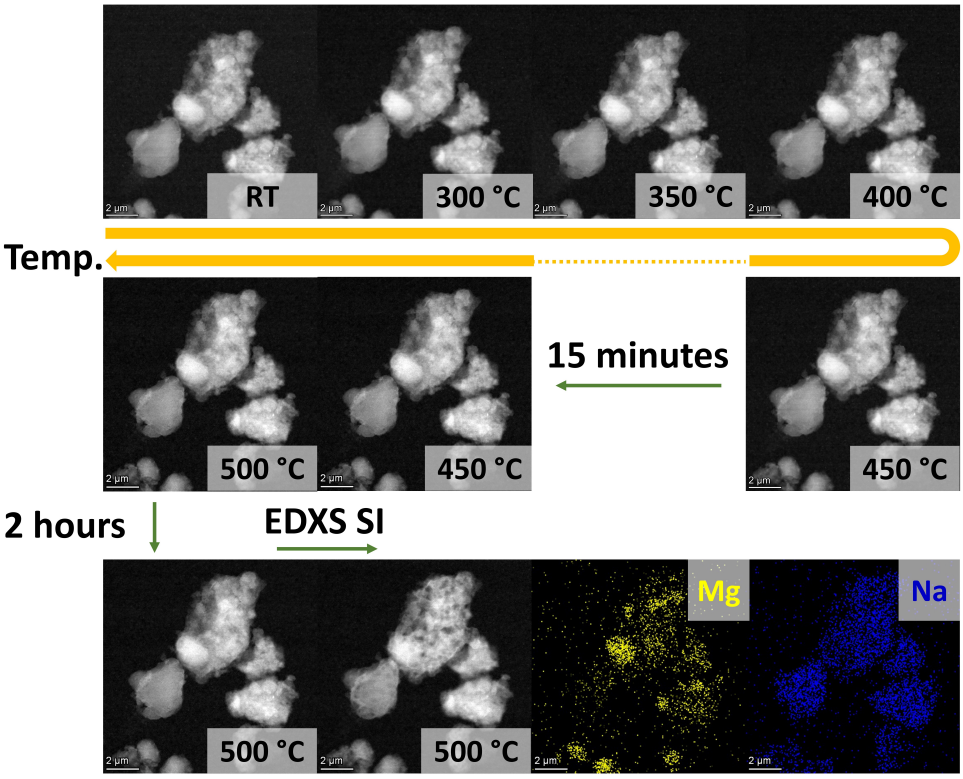

Figure 5.37.: In-situ Investigation on as-milled $NaBH_4$-MgH_2 during the dehydrogenation process under pressure of 0.1 MPa H_2, relying on the in-situ gas system. During the investigation, HAADF-STEM images were acquired at respective temperature using a DT of 4 μs, a SC of 49 pA, a PS of 6.56 nm, a CL of 91 nm, and a CA of 30 mrad, leading to an electron dose of 0.28 $e^-/Å^2$ for each acquisition. EDXS elemental maps of Mg (K-line) and Na (K-line) were acquired in the end of the investigation, generated from 70 frames using a DT of 8 μs, a SC of 51 pA, a PS of 26.30 nm, a CL of 91 nn, and a CA of 30 mrad, delivering an electron dose of about 2.58 $e^-/Å^2$ for the acquisition. A higher pressure of 0.1 MPa H_2 effectively alleviated the oxidation of Mg. However, still no reaction between $NaBH_4$ and Mg was observed.

As shown in Figure 5.37, a HAADF-STEM image was recorded prior to the initiation of annealing. Subsequently, the pressure was adjusted to 0.1 MPa H_2, and the annealing temperature was gradually raised from room temperature to 450 °C at a rate of 6 °C/min. HAADF-STEM images were captured at 300 °C, 350 °C, 400 °C, and 450 °C during the temperature increase. It is important to note that the electron beam was blanked throughout the experiment, except

during the acquisition of HAADF-STEM images or EDXS elemental maps, to ensure effective protection of the materials. When the temperature reached 450 °C, the electron beam was blanked, and the system was maintained under an isothermal condition for 15 minutes. Subsequently, a HAADF-STEM image was recorded. The temperature was then further increased to 500 °C, and another HAADF-STEM image was recorded. After a 2-hour isothermal period at 500 °C with the electron beam blanked, EDXS mapping was conducted. Both the HAADF-STEM images acquired before and after the acquisition of EDXS mapping are presented, along with the EDXS elemental map of Mg and Na.

Throughout the experiment, the presence of hollow structures indicating oxidation of Mg was not observed, in contrast to the previous case using 0.015 MPa $\mathrm{H_2}$. This observation suggests that the materials were effectively protected from oxidation during the experiment due to the use of a higher pressure of $\mathrm{H_2}$, which effectively purged the environment. Comparing the HAADF-STEM images acquired at different stages, it was apparent that the morphology and distribution of the materials remained nearly unchanged. Therefore, it can be anticipated that both $\mathrm{NaBH_4}$ and $\mathrm{MgH_2}$ retained their original forms, even after being annealed at 500°C for two hours. As a result, it can be inferred that the expected reaction between Mg and $\mathrm{NaBH_4}$ did not occur.

To confirm the presence of $\mathrm{NaBH_4}$ and $\mathrm{MgH_2}$ in the local region under investigation, EDXS mapping was thus conducted at the end of the investigation. The acquisition of the EDXS maps resulted in an electron dose of approximately 2.58 $\mathrm{e^-/Å^2}$. The EDXS elemental maps of Mg and Na enabled the differentiation of the distribution and morphology of $\mathrm{MgH_2}$ and $\mathrm{NaBH_4}$. As the signal intensity of oxygen was negligible, the EDXS map of O was not displayed. Furthermore, it is worth noting that despite the accumulated electron dose being only approximately 2.58 $\mathrm{e^-/Å^2}$, the materials suffered significant damage from the electron beam after EDXS mapping. This can be attributed to the high temperature applied, which may intensify the beam damage compared to that experienced at room temperature.

5.3.4.3. In-situ Investigation under Vacuum

To gain further insight into the pressure effect on the oxidation of Mg, an in-situ annealing test was conducted under vacuum using the in-situ annealing holder, as shown in Figure 4.2d. With the in-situ annealing holder, the materials were directly exposed to the TEM column. A related measurement sequence is depicted in Figure 5.38. The annealing temperature was gradually increased from room temperature to 450 °C at a rate of 6 °C/min, and HAADF-STEM images were obtained at RT, 200 °C, 250 °C, 300 °C, 350 °C, 400 °C, and 450 °C, respectively. For each acquisition, an electron dose of 0.90 $\mathrm{e^-/Å^2}$ could be accumulated. Additionally, diffraction patterns were captured before annealing at room temperature and after annealing at 450 °C.

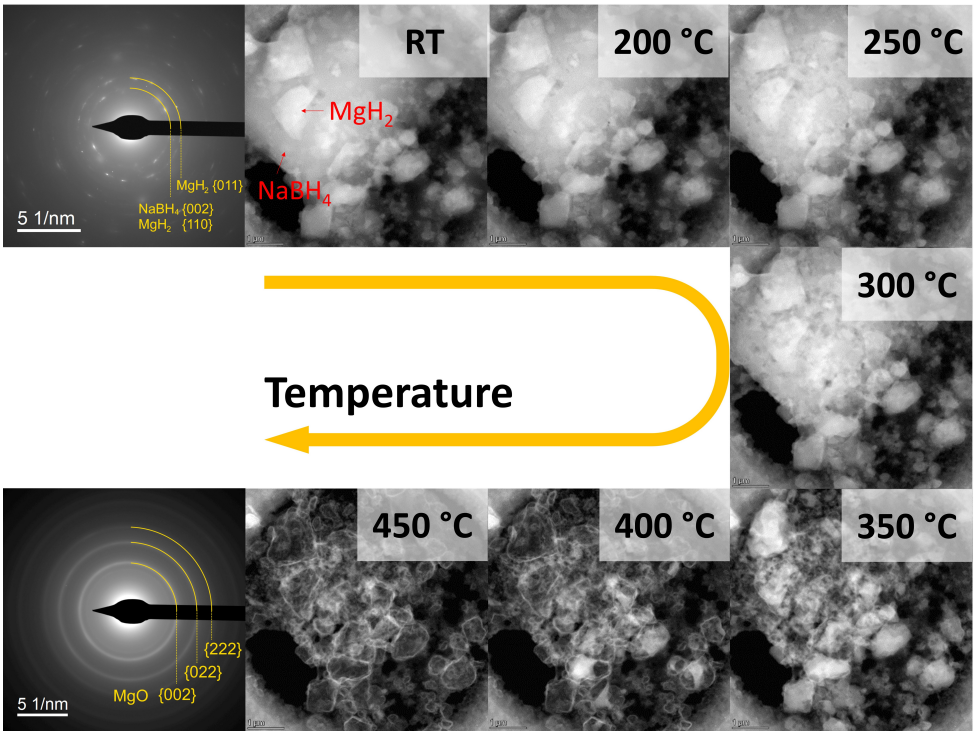

Figure 5.38.: In-situ Investigation on as-milled $NaBH_4$-MgH_2 during the dehydrogenation process under vacuum, relying on the in-situ heating holder. During the investigation, HAADF-STEM images were acquired at respective temperature using a DT of 6 μs, a SC of 26 pA, a PS of 3.29 nm, a CL of 91 nm, and a CA of 30 mrad, leading to an electron dose of 0.90 $e^-/Å^2$ for each acquisition. Diffraction patterns were acquired prior to the begin of annealing and in the end of the investigation. It shows that the oxidation of Mg became severe again under vacuum, verifying the importance of applying a higher pressure.

As depicted in Figure 5.38, the presence of $NaBH_4$ and MgH_2 was determined through electron diffraction prior to the annealing process. At room temperature, it was also observed that crystals with higher contrast were embedded within crystals with lower contrast. Based on previous observations, the crystals with higher contrast were identified as MgH_2, whereas the crystals with lower contrast were identified as $NaBH_4$, as indicated by the arrows. As the temperature increased, the morphology and distribution of the investigated materials remained relatively stable up to 250 °C. Subsequently, changes in the morphology of $NaBH_4$ were observed. The change became even more pronounced with further temperature increase. At 350 °C, hollow structures appeared, suggesting the decomposition of MgH_2 and oxidation of Mg. At 450 °C, almost all Mg grains transformed into hollow structures, indicating complete oxidation of Mg. The formation of MgO was also confirmed by the diffraction pattern obtained at the completion of the annealing process. This should be attributed to the presence of oxygen in the TEM column.

Furthermore, it was noted that $NaBH_4$ had entirely disappeared from the local region under investigation, possibly due to its melting or evaporation behaviors. In summary, the exclusion of the materials' exposure to oxygen is deemed necessary. The application of higher pressure is considered an effective method, which has successfully alleviated the oxidation of Mg and the disappearance/degradation of $NaBH_4$.

6. Discussion

In this chapter, the kinetics of reactive hydride composites (RHCs), specifically the lithium and sodium systems, will be further discussed and analyzed in relation to MgB_2 nucleation and growth. Section 6.1 will focus on MgB_2 nucleation, encompassing the determination of crystal orientation and morphology for MgB_2, identification of the MgB_2 nucleation center, and the determination of relevant orientation relationships. Section 6.2 will delve into MgB_2 growth. Various factors impacting MgB_2 growth, such as temperature, cycling, and different reactive hydride composite systems, will be covered. Furthermore, the rate-controlling step for MgB_2 growth will be determined. Section 6.3 provides a comprehensive overview of the nucleation and growth processes of MgB_2 with respect to various nucleation centers.

6.1. MgB_2 Nucleation Mechanism

The sluggish kinetics of reactive hydride composites (RHCs) represents a significant obstacle to their practical application. In the case of $LiBH_4$-MgH_2, even though the theoretical dehydrogenation temperature of $LiBH_4$-MgH_2 is as low as 225 °C under atmospheric pressure, higher temperatures are practically necessary to expedite the process. As illustrated in Figure 5.1, even at a temperature of 400 °C, it still took about 12 hours to release the majority of H_2 from the material. The incubation plateau, which lasts more than 6 hours, indicates a sluggish MgB_2 nucleation, presumed to be the major bottleneck accounting for the restricted kinetics of $LiBH_4$-MgH_2. As introduced in previous chapters, transition metal additives can provide an impressive boost to the dehydrogenation kinetics. However, due to a lack of microscopic investigations, the underlying mechanism of this kinetic promotion brought by additives has yet to be explicitly clarified, and it will be addressed in this section.

To address this question, $3TiCl_3{\cdot}AlCl_3$ [28] was selected as the additive for this study because of its proven prominent effect on promoting the dehydrogenation kinetics of $LiBH_4$-MgH_2 and its low cost, see Section 2.4.2.3. To amplify the additive effect, in order to simplify the TEM investigations, an overdose of 10 mol% $3TiCl_3{\cdot}AlCl_3$ was purposefully applied. As shown in Figure 5.1, adding 10 mol% $3TiCl_3{\cdot}AlCl_3$ almost eliminates the incubation plateau, indicating

significant facilitation for the heterogeneous nucleation of MgB_2. For a more comprehensive understanding of the additive effect, the sample of $LiBH_4$-MgH_2 with 10 mol% $3TiCl_3 \cdot AlCl_3$ was studied in both as-milled and desorbed states. For comparison, the sample of $LiBH_4$-MgH_2 without additives were investigated throughout the dehydrogenation process, including the state of as-milled, incubated, incompletely-desorbed and desorbed. These states were represented by the timestamps from A through D, labeled in Figure 5.1.

6.1.1. Determination of Crystal Orientation and Morphology for MgB_2

For the sample of $LiBH_4$-MgH_2 without additives, the dehydrogenation was confirmed by the successful transition of $LiBH_4$ and MgH_2 into LiH and MgB_2, as shown in the corresponding XRD spectra in Figure 5.2a and Figure 5.4a. Furthermore, according to the TEM investigations, a significant change in the distribution and morphology was observed between the reactant MgH_2 and the product MgB_2. In contrast to the irregular MgH_2 grains observed before dehydrogenation in Figure 5.2, a rectangular bar-shaped morphology was determined for individual MgB_2 grains generated from the dehydrogenation process, as shown by the tomographic analysis in Figures 5.5a and b.

The crystal orientations of the rectangular bar-shaped grains of MgB_2 were further determined by the related HRTEM in Figure 5.6 and 4D-STEM analysis in Figure 5.7. It was discovered that the predominant growth of MgB_2 crystals occurred in the crystal orientation $\langle 1\,\bar{2}\,1\,0 \rangle_{MgB_2}$. Furthermore, a restricted growth was found along a perpendicular orientation, which was determined to be $\langle 0\,0\,0\,2 \rangle_{MgB_2}$ due to the growth constraint along the c-axis for MgB_2, as reported by Lee *et al.* [168]. Accordingly, the crystal orientation of MgB_2 for the moderate growth direction, which is perpendicular to the predominant and restricted growth orientations, was determined to be $\langle 1\,0\,\bar{1}\,0 \rangle_{MgB_2}$.

The observation of a bar-shaped morphology is surprising. The hexagonal close-packed lattice structure of MgB_2 leads to a close-packed arrangement of atoms in the $\{0\,0\,0\,2\}$ plane, resulting in the lowest surface energy and the largest possible $\{0\,0\,0\,2\}$ facets. Typically, this pattern aligns with a hexagonal platelet-shaped morphology, with prism planes exhibiting six-fold symmetry acting as borders. However, in this particular case, the MgB_2 crystals with a bar-shaped morphology can be observed where the $\{0\,0\,0\,2\}$ facets are bordered by two perpendicular planes of different types. This suggests the occurrence of a lattice matching phenomenon between MgB_2 crystals and a nucleation center.

Moreover, it seems that the generated MgB_2 crystals grew predominantly not only in the same spatial orientation, but also in the same crystal orientation. This was determined by the 4D-STEM analysis in Figure 5.7. The diffraction patterns represent the respective MgB_2 crystals, which were spatially parallel-oriented. Although they were displayed along different zone axes, their predominant growth was found to occur with respect to the same crystal orientation, which was $(1\,\bar{2}\,1\,0)_{MgB_2}$. This parallelism behavior was verified by conversely mapping the distribution of MgB_2 by selecting different diffraction spots. It turns out that the mapped MgB_2 crystals were spatially orienting in the same direction. The observed parallelism is considered to indicate the heterogeneous nucleation of MgB_2 on the same nucleation center.

Similarly, parallel-oriented MgB_2 crystals were still observed by adding 10 mol% $3TiCl_3{\cdot}AlCl_3$, as illustrated in Figure 5.11. In contrast, instead of the rectangular bar-shaped morphology observed earlier, a hexagonal platelet-shaped morphology was determined in this case by the tomographic analysis based on the EDXS elemental map of Mg, as shown in Figure 5.12. Accordingly, the crystal orientations with respect to this new morphology were also studied. Considering the crystal structure of hexagonal close-packed for MgB_2, the basal plane was determined to be $\{0\,0\,0\,2\}_{MgB_2}$, while the prism plane with six-fold symmetry was determined to be either $\{1\,0\,\bar{1}\,0\}_{MgB_2}$ or $\{1\,\bar{2}\,1\,0\}_{MgB_2}$.

The significantly larger aspect ratio for the basal plane $\{0\,0\,0\,2\}_{MgB_2}$ of the rectangular bar-shaped MgB_2 was considered to result from the combination of predominant growth in $\langle 1\,\bar{2}\,1\,0\rangle_{MgB_2}$ and moderate growth in $\langle 1\,0\,\bar{1}\,0\rangle_{MgB_2}$. However, such distinct growth behavior was not observed for the hexagonal platelet-shaped MgB_2, as reflected in its aspect ratio of approximately 1 for the basal plane $\{0\,0\,0\,2\}_{MgB_2}$. Notably, a larger number of MgB_2 crystals with a hexagonal platelet-shaped morphology were observed, while MgB_2 crystals with a rectangular bar-shaped morphology were found to be larger in dimension, with a maximum length of up to tens of micrometers for the predominant growth direction. These variations suggest that the heterogeneous nucleation of MgB_2 may depend on different nucleation centers, resulting in a different morphology.

6.1.2. Determination of MgB_2 Nucleation Centers

The observed spatially parallel-oriented MgB_2 crystals generated from the reaction between $LiBH_4$ and Mg suggest a heterogeneous nucleation based on a nucleation center, which is speculated to have controlled the formation of MgB_2. In the absence of additives, candidates for this nucleation center include Mg and $LiBH_4$, given the two-step dehydrogenation of $LiBH_4$-MgH_2 shown in Equation 5. Since $LiBH_4$ is liquid during dehydrogenation at 400 °C, the solid Mg is

considered to be the nucleation center for the observed MgB_2 bars. Moreover, the nucleation center must provide a superficial plane with sufficient area to accommodate the nucleation of several MgB_2 crystals on the same class of atomic layer. Mg generated from the decomposition of MgH_2 was thus investigated, as illustrated in Figure 5.3. It was observed that the formed Mg grains were several hundred nanometers in size, meeting the requirement to serve as the nucleation center for heterogeneous nucleation of bar-shaped MgB_2 crystals with a lateral dimension of about 200 nm, see Figure 5.5b.

To validate the role of Mg as the nucleation center, the sample containing incompletely-desorbed $LiBH_4$-MgH_2 without additives was examined, referred to as timestamp C in Figure 5.1. In this case, both Mg and MgB_2 coexisted, providing an opportunity to investigate their relative positions. As depicted in Figures 5.8 and 5.9, Mg grains were observed at the bottom of the parallel-oriented MgB_2 crystals. This finding confirms that the Mg grains act as nucleation centers for MgB_2 crystals. Furthermore, through Figure 5.9d, it can be observed that these MgB_2 crystals are interconnected at the bottom position (area 5). Hence, the bottom region of MgB_2 is considered as the former location of the nucleation center Mg. Since Mg could act as the nucleation center for the heterogeneous nucleation of MgB_2, the improvement in dehydrogenation kinetics observed with the non-stoichiometric Li-RHC (e.g., $LiBH_4$+$2MgH_2$) compared to the stoichiometric Li-RHC (e.g., $2LiBH_4$+MgH_2), as previously reported by Price *et al.* [171], could also be interpreted. This improvement was mainly attributed to the addition of an excess amount of Mg grains, which led to more nucleation centers to facilitate the heterogeneous nucleation of MgB_2.

The presence of another nucleation center, in addition to Mg, is found to be related to $3TiCl_3{\cdot}AlCl_3$, as reflected in the change in the MgB_2 morphology (Figure 5.12), crystallographic variation (Figure 5.13) and accelerated dehydrogenation kinetics of $LiBH_4$-MgH_2 (Figure 5.1) in the presence of additives. A reaction between $3TiCl_3{\cdot}AlCl_3$ and $LiBH_4$ is proved to occur because they are the only materials capable of providing Li and Cl in this case, resulting in the generation of $LiCl$, see Figure 5.10 and 5.11. Further identification of other products from the reaction between $3TiCl_3{\cdot}AlCl_3$ and $LiBH_4$ was performed using EELS, as illustrated in Figure 5.14. A correlation between Ti and B with respect to elemental distribution was determined based on the EELS elemental maps of these elements. The crystallographic information was determined by HRTEM, which identified the generation of TiB_2, as shown in Figure 5.15. It is thus considered that TiB_2 is the other nucleation center for heterogeneous nucleation of MgB_2 crystals with a platelet-shaped morphology. Considering TiB_2 and AlB_2 share the same crystal structure and similar lattice constants, AlB_2 may also act as the nucleation center. However, in this case, the existence of AlB_2 cannot be determined through HRTEM or EELS. The practical verification of the role of TiB_2 (and AlB_2) as the nucleation center is not feasible due to the small average size of TiB_2 nanoparticles, approximately 3 nm, as shown in Figure 5.15. The absence of TiB_2 in

the electron diffraction pattern and XRD spectrum is further evidence of their small dimensions, making it nearly impossible to determine the orientation relationship with respect to the proper interface between MgB_2 and TiB_2 (and AlB_2) directly using TEM approaches.

6.1.3. Orientation Relationship between MgB_2 and Nucleation Centers

As the nucleation centers have been identified for the respective cases, determining the orientation relationships between MgB_2 and either nucleation center with respect to their interface is deemed crucial for understanding the morphological differences. However, direct experimental investigations of their orientation relationships at the interface proves were not successfully conducted. Thus, the orientation relationships were analytically determined using the edge-to-edge matching model, as described in Subsection 2.4.3. It provides the energetically most relevant orientation relationships between the nucleation centers and MgB_2. According to the edge-to-edge matching model [172, 172], the matching directions and matching planes are normally chosen from the close packed or nearly close packed directions and planes. Since MgB_2, Mg, and TiB_2 (and AlB_2) share the same hexagonal close-packed (hcp) crystal structure, their close or nearly close-packed directions and planes are similarly indexed. Based on the crystallographic characteristics of the hcp crystal structure [127], the close or nearly close-packed directions are $\langle 1\,0\,\bar{1}\,0\rangle$, $\langle 1\,1\,\bar{2}\,3\rangle$, and $\langle 1\,\bar{2}\,1\,0\rangle$, whereas the close or nearly close-packed planes are $\{1\,0\,\bar{1}\,0\}$, $\{1\,0\,\bar{1}\,1\}$, $\{0\,0\,0\,2\}$, and $\{1\,\bar{2}\,1\,0\}$.

As the growth of MgB_2 crystals was found to be restricted in the $\langle 0\,0\,0\,2\rangle$ direction, regardless of the presence or absence of additives, $\{0\,0\,0\,2\}_{MgB_2}$ is considered as the matching plane for MgB_2. The interplanar misfit between the matching plane $\{0\,0\,0\,2\}_{MgB_2}$ MgB_2 and the possible matching plane for Mg is listed in Table 6.1. Accordingly, the most reasonable matching plane for Mg is determined as $\{1\,\bar{2}\,1\,0\}_{Mg}$, delivering the lowest interplanar misfit of 9.3 %. It should be noted that the interplanar misfit can be further reduced by rotating the two matching planes about their matching directions.

Table 6.1.: The interplanar misfit between the relevant matching planes of MgB_2 and Mg.

	$\{0\,0\,0\,2\}/\{1\,0\,\bar{1}\,1\}$	$\{0\,0\,0\,2\}/\{1\,0\,\bar{1}\,0\}$	$\{0\,0\,0\,2\}/\{0\,0\,0\,2\}$	$\{0\,0\,0\,2\}/\{1\,\bar{2}\,1\,0\}$
MgB_2 / Mg	-28.4 %	-36.9 %	-32.7 %	**9.3 %**

It is known that the corresponding close or nearly close-packed direction should be included in the close or nearly close-packed plane. Given that the matching plane for MgB_2 is

Table 6.2.: The interatomic misfit between the relevant matching directions of MgB_2 and Mg.

	$\langle 1\,0\,\bar{1}\,0\rangle \| \langle 1\,0\,\bar{1}\,0\rangle$	$\langle 1\,\bar{2}\,1\,0\rangle \| \langle 1\,0\,\bar{1}\,0\rangle$
MgB_2 ∥ Mg	**-4.3 %**	-44.7 % %

$\{0\,0\,0\,2\}_{MgB_2}$, the possible matching direction for MgB_2 should be selected from $\langle 1\,0\,\bar{1}\,0\rangle_{MgB_2}$ and $\langle 1\,\bar{2}\,1\,0\rangle_{MgB_2}$. Similarly, since the matching plane for Mg is $\{1\,\bar{2}\,1\,0\}_{Mg}$, the matching direction for Mg is supposed to be $\langle 1\,0\,\bar{1}\,0\rangle_{Mg}$. The related interatomic misfits of the respective combinations of matching directions have been calculated and listed in Table 6.2. An interatomic misfit of about -4.3 % is delivered by the combination of $\langle 1\,0\,\bar{1}\,0\rangle_{MgB_2}$ and $\langle 1\,0\,\bar{1}\,0\rangle_{Mg}$. The theoretical orientation relationship between MgB_2 and Mg are derived as follows:

$$\langle 1\,0\,\bar{1}\,0\rangle_{MgB_2} || \langle 1\,0\,\bar{1}\,0\rangle_{Mg}, \{0\,0\,0\,2\}_{MgB_2} / \{1\,\bar{2}\,1\,0\}_{Mg} \tag{6.1}$$

Table 6.3.: The interplanar misfit between the relevant matching interatomic planes of MgB_2 and TiB_2 or AlB_2.

	$\{0\,0\,0\,2\}/\{1\,0\,\bar{1}\,1\}$	$\{0\,0\,0\,2\}/\{1\,0\,\bar{1}\,0\}$	$\{0\,0\,0\,2\}/\{0\,0\,0\,2\}$	$\{0\,0\,0\,2\}/\{1\,\bar{2}\,1\,0\}$
MgB_2 ∥ TiB_2	-13.6 %	-32.9 %	**9.0 %**	16.1 %
MgB_2 ∥ AlB_2	-13.4 %	-32.3 %	**8.2 %**	17.2 %

Table 6.4.: The interatomic misfit between the relevant matching directions of MgB_2 and TiB_2 or AlB_2.

	$\langle 1\,0\,\bar{1}\,0\rangle \| \langle 1\,0\,\bar{1}\,0\rangle$	$\langle 1\,0\,\bar{1}\,0\rangle \| \langle 1\,\bar{2}\,1\,0\rangle$	$\langle 1\,\bar{2}\,1\,0\rangle \| \langle 1\,0\,\bar{1}\,0\rangle$	$\langle 1\,\bar{2}\,1\,0\rangle \| \langle 1\,\bar{2}\,1\,0\rangle$
MgB_2 ∥ TiB_2	**1.7 %**	76.2 %	-41.2 %	**1.7 %**
MgB_2 ∥ AlB_2	**2.6 %**	77.8 %	-40.7 %	**2.7 %**

The same approach can be utilized to derive the orientation relationship between MgB_2 and TiB_2 (and AlB_2). As the matching plane for MgB_2 remains $\{0\,0\,0\,2\}_{MgB_2}$, a low interplanar misfit can be achieved, when the matching plane for Mg is $\{0\,0\,0\,2\}_{TiB_2}$, with a misfit of down to 9.0 %, as shown in Table 6.3. Therefore, the matching direction for both MgB_2 and TiB_2 should be selected from $\langle 1\,0\,\bar{1}\,0\rangle$ and $\langle 1\,\bar{2}\,1\,0\rangle$, which are included in the matching plane $\{0\,0\,0\,2\}$. The interatomic misfit between MgB_2 and TiB_2 was then calculated based on the corresponding combinations of matching directions, as presented in Table 6.4. The combination of either $\langle 1\,0\,\bar{1}\,0\rangle_{MgB_2}$ and $\langle 1\,0\,\bar{1}\,0\rangle_{TiB_2}$ or $\langle 1\,\bar{2}\,1\,0\rangle_{MgB_2}$ and $\langle 1\,\bar{2}\,1\,0\rangle_{TiB_2}$ results in the lowest interatomic misfit, which is

about 1.7 %. Thus, the possible orientation relationships between MgB_2 and TiB_2 can be derived as follows:

$$\langle 1\,0\,\bar{1}\,0\rangle_{MgB_2} || \langle 1\,0\,\bar{1}\,0\rangle_{TiB_2}, \{0\,0\,0\,2\}_{MgB_2} / \{0\,0\,0\,2\}_{TiB_2} \tag{6.2}$$

$$\langle 1\,\bar{2}\,1\,0\rangle_{MgB_2} || \langle 1\,\bar{2}\,1\,0\rangle_{TiB_2}, \{0\,0\,0\,2\}_{MgB_2} / \{0\,0\,0\,2\}_{TiB_2} \tag{6.3}$$

The elastic strain energy density ϵ_{hkil} for any given lattice plane $\{h\,k\,i\,l\}$ can be calculated using the equation $\epsilon_{hkil} = \frac{1}{2} Y_{hkil} \delta_{hkil}^2$, where Y_{hkil} and δ_{hkil} represent the Young's modulus and the atomic misfit with respect to a certain crystal orientation [173]. The corresponding Young's modulus Y_{hkil} for MgB_2 can then be calculated by substituting the Miller indices of the lattice plane hkil, the elastic constants (C_{11} = 365 GPa, C_{12} = 98 GPa, C_{13} = 65 GPa, C_{33} = 203 GPa, and C_{44} = 58 GPa), and the lattice constants (a = 3.0851 Å and c = 3.5201 Å) into Equation 6.4 [174, 175]. The compliances S_{ij} in the equation can be determined from the elastic constants C_{lk} based on the given crystal structure [176].

$$Y_{hkil} = \frac{\left[h^2 + \frac{(h+2k)^2}{3} + \left(\frac{a}{c} l\right)^2 \right]^2}{\left[S_{11} \left(h^2 + \frac{(h+2k)^2}{3} \right)^2 + S_{33} \left(\frac{a}{c} l\right)^4 + (S_{44} + 2\,S_{13}) \left(h^2 + \frac{(h+2k)^2}{3} \right) \left(\frac{a}{c} l\right)^2 \right]} \tag{6.4}$$

The elastic strain energy density required for the nucleation of MgB_2 based on different nucleation centers can be calculated accordingly. The related crystal orientations for the nucleation of MgB_2 are $\langle 1\,0\,\bar{1}\,0\rangle_{MgB_2}$, $\langle 1\,\bar{2}\,1\,0\rangle_{MgB_2}$, and $\langle 0\,0\,0\,2\rangle_{MgB_2}$. The corresponding Young's modulus Y_{hkil} can be determined for MgB_2 with respect to the related crystal orientations, as shown in Table 6.5, based on Equation 6.4. The corresponding elastic strain energy density for the nucleation of MgB_2 can be determined, as shown in Table 6.5, by knowing the corresponding Young's modulus Y_{hkil} and the atomic misfit δ_{hkil} with respect to either Mg or TiB_2.

A large elastic strain energy density of 7.4×10^8 J/m^3 was determined for the nucleation of MgB_2 with respect to the orientation $\langle 0\,0\,0\,2\rangle_{MgB_2}$ when Mg is the nucleation center. This large value of elastic strain energy density may be responsible for the restricted growth observed in MgB_2 crystals with a bar-shaped morphology along $\langle 0\,0\,0\,2\rangle_{MgB_2}$. Additionally, a elastic strain energy density of 2.9×10^8 J/m^3 was determined for the nucleation of MgB_2 along the orientation $\langle 1\,0\,\bar{1}\,0\rangle_{MgB_2}$. Table 6.1 and 6.2 show that $\langle 1\,\bar{2}\,1\,0\rangle_{MgB_2}$ cannot serve as the matching plane or matching direction for MgB_2 when Mg is the nucleation center. Therefore, the elastic strain energy density was not calculated for MgB_2 with respect to the orientation $\langle 1\,\bar{2}\,1\,0\rangle_{MgB_2}$ in this case, as marked as 'not relevant' in Table 6.5.

Table 6.5.: Elastic strain energy density for MgB_2 determined by the Young's modulus Y_{hkil} and the atomic misfit δ_{hkil} for MgB_2 with respect to a different nucleation center (Mg or TiB_2), based on the crystal orientations $\langle 0\,0\,0\,2\rangle_{MgB_2}$, $\langle 1\,0\,\bar{1}\,0\rangle_{MgB_2}$, and $\langle 1\,\bar{2}\,1\,0\rangle_{MgB_2}$ for MgB_2.

MgB_2 Orientation		$\langle 0\,0\,0\,2\rangle$	$\langle 1\,0\,\bar{1}\,0\rangle$	$\langle 1\,\bar{2}\,1\,0\rangle$
Y_{hkil} [GPa]		184.7	326.9	326.9
δ_{hkil} [%]	Mg	9.3	-4.3	not relevant
	TiB_2	9.0	1.7	1.7
ϵ_{hkil} [10^7 J/m^3]	Mg	74	29	not relevant
	TiB_2	73	4.7	4.7

When TiB_2 serves as the nucleation center, a large elastic strain energy density of 7.3×10^8 J/m^3 was also determined for the nucleation of MgB_2 with respect to the orientation $\langle 0\,0\,0\,2\rangle_{MgB_2}$. This may also be responsible for the restricted growth observed in MgB_2 crystals with a platelet-shaped morphology along $\langle 0\,0\,0\,2\rangle_{MgB_2}$, as reflected in their relatively small thickness. Two possible orientation relationships between TiB_2 and MgB_2 have been determined (Table 6.4), and the matching direction for MgB_2 at the interface with TiB_2 can be either $\langle 1\,\bar{2}\,1\,0\rangle_{MgB_2}$ or $\langle 1\,0\,\bar{1}\,0\rangle_{MgB_2}$. In either case, the required elastic strain energy density for both $\langle 1\,\bar{2}\,1\,0\rangle_{MgB_2}$ and $\langle 1\,0\,\bar{1}\,0\rangle_{MgB_2}$ is determined to be 4.7×10^7 J/m^3.

6.1.4. Growth of MgB_2 Precipitates

As illustrated in Figure 6.1, when comparing the elastic strain energy density raised along respective matching directions between Mg and TiB_2, it is observed that a considerably larger elastic strain energy density is required for the matching to Mg (2.9×10^8 J/m^3 in $\langle 1\,0\,\bar{1}\,0\rangle_{MgB_2}$) than for the matching to TiB_2 (4.7×10^7 J/m^3 in $\langle 1\,0\,\bar{1}\,0\rangle_{MgB_2}$ or $\langle 1\,\bar{2}\,1\,0\rangle_{MgB_2}$). According to the experimental observations shown in Figure 5.7, the predominant growth direction of MgB_2 crystals with a bar-shaped morphology is $\langle 1\,\bar{2}\,1\,0\rangle_{MgB_2}$. This predominant growth can be considered as a result of the high elastic strain energy density required at the interface between MgB_2 and Mg, as $\langle 1\,\bar{2}\,1\,0\rangle_{MgB_2}$ is perpendicular to both $\langle 1\,0\,\bar{1}\,0\rangle_{MgB_2}$ and $\langle 0\,0\,0\,2\rangle_{MgB_2}$. In other words, the MgB_2 crystals tend to grow in the direction that is perpendicular to the MgB_2-Mg interface. On the other hand, in the presence of TiB_2 nanoparticles, the perpendicular growth direction of MgB_2 crystals relative to the connection position was observed to be $\langle 1\,0\,\bar{1}\,0\rangle_{MgB_2}$, as shown in Figure 5.13. This experimental observation is in agreement with the theoretical prediction, see Table 6.4. With the inclusion of TiB_2, the matching direction for MgB_2 crystals can be $\langle 1\,\bar{2}\,1\,0\rangle_{MgB_2}$, and the corresponding matching plane is $\{0\,0\,0\,2\}_{MgB_2}$. Consequently, the growth direction of MgB_2

crystals, mutually perpendicular to both the matching plane and the matching direction, turns out to be $\langle 1\,0\,\bar{1}\,0\rangle_{MgB_2}$.

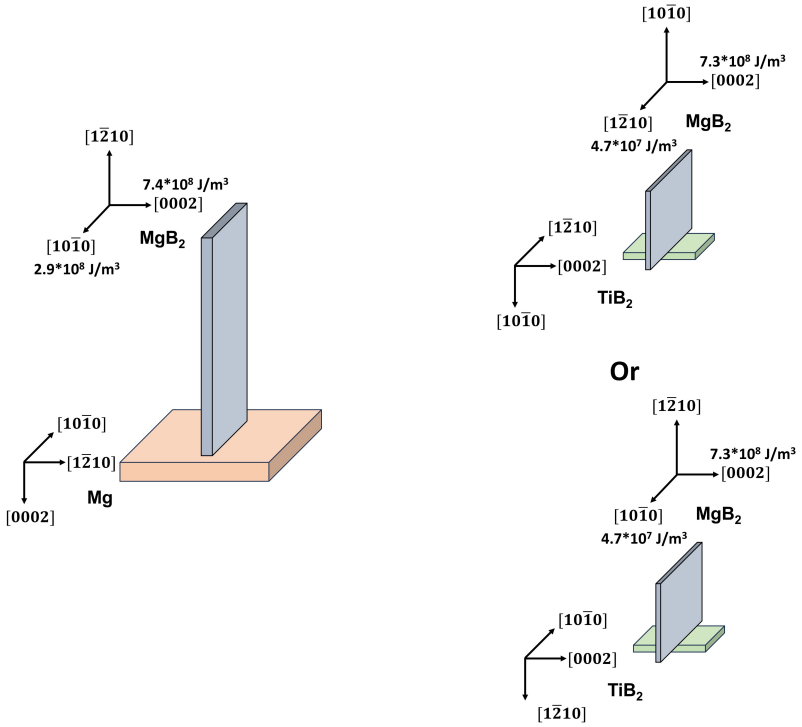

Figure 6.1.: Schematic illustration depicting the heterogeneous nucleation of MgB_2 based on Mg or TiB_2, considering the orientation relationships and the associated elastic strain energy density.

As discussed in Section 2.3.1, at 400°C, $LiBH_4$ is in a molten state, approximately 120 °C above its melting point. The observed bar-shaped morphology of MgB_2 suggests that the nucleation and subsequent growth of MgB_2 are continuously influenced by the high elastic strain energy density required at the interface between MgB_2 and Mg. It can be inferred that molten $LiBH_4$ constantly reacts with solid Mg at the MgB_2-Mg interface to generate MgB_2. For MgB_2 growth on top of the precipitates, it is necessary to have Mg grains in that position. Therefore, diffusion of Mg would have to occur at the side of MgB_2 towards the top of the precipitate. The same principle applies when TiB_2 acts as the nucleation center, resulting in MgB_2 generation at the MgB_2-TiB_2 interface. It should be noted that the parallel-oriented MgB_2 platelets should be not solely reliant on a single TiB_2 nanoparticle, considering the smaller size of TiB_2 (3 nm on average) and the much larger dimension of the resulting MgB_2 crystals (> 100 nm). It is likely a collective effect involving multiple TiB_2 nanoparticles positioned on the surface of Mg grains.

The presence of TiB_2 nanoparticles between Mg and MgB_2 effectively decreases the elastic strain energy density, facilitating phase matching and heterogeneous nucleation of MgB_2. Moreover, it is suggested that the growth of MgB_2 crystals is not hindered based on TiB_2, except along the $\langle 0\,0\,0\,2 \rangle_{MgB_2}$ direction, thus leading to the formation of hexagonal platelet-shaped morphology. Therefore, it is reasonable to attribute the accelerated nucleation process of MgB_2 caused by additives to the presence of a heterogeneous nucleation center, which reduces the elastic strain energy density for MgB_2 generation at the MgB_2-TiB_2 interface.

6.2. MgB_2 Growth Mechanism

In addition to the major bottleneck caused by the nucleation of MgB_2 for the dehydrogenation kinetics of $LiBH_4$-MgH_2, the speed of hydrogen release is also considerably affected by the subsequent growth of MgB_2. To comprehend the underlying mechanism responsible for the growth of MgB_2, different variables were involved for investigation and discussion, including additive content, annealing temperature for dehydrogenation, and cycling. Furthermore, determining the rate-controlling step for the growth of MgB_2 under these circumstances aims to address further restrictions on the kinetics of $LiBH_4$-MgH_2.

6.2.1. MgB_2 Growth under Varying Circumstances

It is demonstrated in Figure 5.16 that the incubation plateau can be almost eliminated through the addition of 1 mol% $3TiCl_3{\cdot}AlCl_3$. According to the previous discussion, this indicates the occurrence of a heterogeneous nucleation process for MgB_2 facilitated by TiB_2, which requires a lower elastic strain energy density for the nucleation of MgB_2. However, as shown in Figure 5.20 and 5.21, both bar-shaped and platelet-shaped MgB_2 crystals were observed, indicating the possibility of a heterogeneous nucleation process that relies on both Mg and TiB_2 when 1 mol% $3TiCl_3{\cdot}AlCl_3$ is added. In contrast, increasing the additive content to 5 mol% $3TiCl_3{\cdot}AlCl_3$ resulted in the observation of solely platelet-shaped MgB_2 crystals as displayed in Figure 5.22 and 5.23. This absence of MgB_2 crystals with a bar-shaped morphology suggests that the MgB_2 nucleation based on TiB_2 dominates as the additive amount increases, compared to that based on Mg. Nevertheless, it is imperative to note that MgB_2 nucleation based on Mg can still occur, but due to experimental limitations, it was not observed.

The dehydrogenation of $LiBH_4$-MgH_2 was attempted at a higher annealing temperature to investigate the effect on MgB_2 nucleation and growth. Raising the annealing temperature to 420°C still revealed a noticeable incubation plateau, though the incubation period was reduced

substantially to around 5 hours compared to 8 hours at 400°C, as shown in Figure 5.16. The decrease in incubation period at 420°C also appears to have affected the MgB_2 morphology. As shown in Figure 5.24 and 5.25, parallel-oriented MgB_2 crystals were observed exhibiting a platelet-shaped morphology and an aspect ratio close to 3 for the basal plane, rather than a bar-shaped morphology with an aspect ratio of several tens generated at 400°C. This is impressive since Mg served as the sole nucleation center in this case. As it is known, raising the temperature of a reaction can accelerate the motion of reactant particles, and potentially aid in surmounting the activation energy barrier. Therefore, the elevation of the annealing temperature potentially mitigated the constraints on MgB_2 nucleation and growth along the in-plane directions based on Mg grains. Based on this observation, it is considered that the growth of MgB_2 is not that limited from an energetic perspective. Furthermore, an increase in temperature can result in the expansion of the lattice, which can potentially impact the misfit at the interface between MgB_2 and Mg, thereby altering the required elastic strain energy density for MgB_2. However, considering the small temperature increment of only 20 °C, the change in the misfit and the required elastic strain energy density is deemed to be negligible.

The effect of cycling on the dehydrogenation kinetics of LiH-MgB_2 was studied within 10 cycles. When compared with directly desorbed $LiBH_4$-MgH_2, the 10th dehydrogenation process of the cycled LiH-MgB_2 nearly eliminated the incubation plateau, as shown in Figure 5.16. Since the hydrogen uptake throughout the cycling process is less than 10 wt%, which is lower than the theoretical hydrogen storage capacity of 11.5 %, the hydrogenation process was not complete. Thus, the existence of residual MgB_2 can be expected. This must be present from the beginning of the cycling process. The acceleration in the nucleation process of MgB_2 can be therefore attributed to its heterogeneous nucleation relying on residual MgB_2 crystals serving as nuclei during the cycling process, as their misfit being zero. This was further supported by the altered the MgB_2 morphology, as observed in Figures 5.26 through 5.28. Hexagonal platelet-shaped MgB_2 crystals were observed with the same crystal orientations with respect to the morphology, appearing comparable to the case when additives are present. However, in this case, the observed MgB_2 crystals had a much larger thickness of more than 100 nm, given that the basal plane was still on a comparable scale. This suggests that MgB_2 was much less restricted to grow along the c-axis $\langle 0\,0\,0\,2\rangle_{MgB_2}$, compared to the heterogeneous nucleation of MgB_2 based on TiB_2. This can be attributed to the fact that when residual MgB_2 crystals act as the nucleation center, no interface energy is required. Furthermore, in this case, the absence of parallel-oriented MgB_2 crystals was observed, which indicates that the heterogeneous nucleation of MgB_2 is predominantly based on residual MgB_2 rather than Mg.

The cycling performance of LiH-MgB_2 was evaluated without and with additives, as shown in Figures 5.17 and 5.18. In the absence of additives, an improved dehydrogenation kinetics of LiH-MgB_2 was observed for each cycle due to heterogeneous nucleation of MgB_2 based on residual

MgB_2, as previously discussed. The addition of 5 mol% $3TiCl_3{\cdot}AlCl_3$ further improved the dehydrogenation kinetics, reducing the total duration from about 2 hours to less than half an hour. The presence of additives also significantly impacted hydrogenation kinetics, reducing the initial duration from about 5 hours in the absence of additives to approximately 0.5 hours. Additionally, the performance in hydrogenation kinetics became more stable and consistent with the presence of additives for each cycle. This improvement raised by additives can be attributed to an instability of MgB_2 nuclei responsible for heterogeneous nucleation in terms of their distribution and size. During hydrogenation or dehydrogenation, the consumption and agglomeration of residual MgB_2 nuclei occur. This hinders the even distribution of nucleation centers, consequently impacting the nucleation of MgB_2. Thus, it is necessary to introduce TiB_2 nanoparticles that support a more stable heterogeneous nucleation of MgB_2 for achieving a synergetic improvement in kinetics, as compared to the unstable heterogeneous nucleation of MgB_2 relying solely on residual MgB_2. Furthermore, the addition of TiB_2 also directly increases the number of nucleation centers, thereby further accelerating the nucleation of MgB_2.

To determine whether the knowledge gained from Li-RHC could be applied to other reactive hydride composites, Na-RHC was studied. Although the theoretical dehydrogenation temperature for $NaBH_4$-MgH_2 was found to be 350 °C at atmospheric pressure, it was necessary to increase the temperature to 450 °C to complete the dehydrogenation process within a reasonable timeframe, as depicted in Figure 5.30. This requirement may be also attributed to the necessity of the liquid phase of $NaBH_4$ with a melting point of 400 °C (see Section 6.1.4), which accelerates the motion of $NaBH_4$ and, thus, facilitates the reaction between $NaBH_4$ and Mg. A similar phenomenon was also observed for $LiBH_4$-MgH_2, where the theoretical decomposition temperature is approximately 225 °C, but a much higher temperature of 400 °C is necessary in practice to proceed with the decomposition, considering the melting point of $LiBH_4$, which is around 277 °C.

When $NaBH_4$-MgH_2 was annealed at 450 °C, the decomposition kinetics was improved and MgB_2 was identified. However, the presence of $NaBH_4$ and Na was also observed, indicating an incomplete reaction between $NaBH_4$ and Mg, and the hydrogen release being partially the result of a further decomposition of NaH under the given conditions, as illustrated in Figure 5.32. The further decomposition of NaH has a negative impact on the cyclability of $NaBH_4$-MgH_2, as the restoration of reversibility can only be achieved by subjecting the hydrogenation process to significantly more harsh temperature and pressure conditions. Spatially parallel-oriented MgB_2 crystals with a platelet-shaped morphology were also observed, as depicted in Figures 5.32 and 5.34. 4D-STEM analysis revealed that both parallel MgB_2 crystals orientated in the same direction from the crystallographic perspective, as shown in Figure 5.33. The similar morphology and crystal orientation of MgB_2 observed in Na-RHC and Li-RHC suggested that both materials shared the same underlying mechanism for the nucleation and growth of MgB_2, which influenced

the dehydrogenation kinetics. It was also confirmed that the knowledge gained from one system could be applied to another. To gain a deeper understanding of the mechanism involved, in-situ TEM analysis was performed on $NaBH_4$-MgH_2 since complete dehydrogenation of $LiBH_4$-MgH_2 was not technically achievable due to limited pressure of up to 0.1 MPa. The information gathered from Na-RHC could then be reasonably applied to further develop $LiBH_4$-MgH_2.

Although the same conditions were applied for in-situ TEM analysis as in kinetics measurements, the reaction between Mg and $NaBH_4$-MgH_2 did not occur, which was attributed to the oxidation of Mg at the first stage, as can be seen in Figures 5.36 and 5.38. This emphasizes the importance of a purged environment in the absence of oxygen to protect Mg and potentially also $NaBH_4$. The oxidation of Mg was effectively alleviated by increasing the pressure to 0.1 MPa H_2, which is also the maximum pressure achievable with the in-situ gas system. Nevertheless, the dehydrogenation process still did not occur, as reflected in the unaltered morphology of the relevant materials throughout the entire in-situ investigation despite annealing at 500 °C for several hours, as shown in Figure 5.37. It is possible that the reaction may occur by further increasing the annealing temperature under the applied pressure of 0.1 MPa. However, it should be noted that increasing the temperature would cause more severe electron beam damage (see Section 5.3.4.3), which could conversely limit the window for effective TEM investigation and analysis. On the other hand, another concern arises when the temperature is further increased due to the potential evaporation of $NaBH_4$, which has a boiling temperature of 500 °C [177].

6.2.2. Rate-Controlling Step for MgB_2 Growth Kinetics

Various variables can affect the growth kinetics of MgB_2, which is reflected not only in the varied morphology of MgB_2, but also in the hydrogen release rate. As shown in Figure 6.2, the hydrogen release over time resulting from the reaction between Mg and $LiBH_4$ for the relevant samples is normalized via min-max normalization. The start and end points of the curves were determined with respect to the respective onsets. As demonstrated, it generally takes about twice as long to release approximately 90 % of hydrogen from $LiBH_4$-MgH_2 annealed at 400 °C in the absence of additives compared to when additives are present or when annealed at a higher temperature. Therefore, it is essential to determine the rate-controlling step for MgB_2 growth under different conditions.

As introduced in Subsection 2.4.1, the Johnson-Mehl-Avrami-Kolmogorov (JMAK) equation, represented by Equation 2.6 [104], can be effectively utilized to describe the kinetics of phase transformation in solids and to gain a comprehensive understanding of the growth of MgB_2 during the dehydrogenation process.

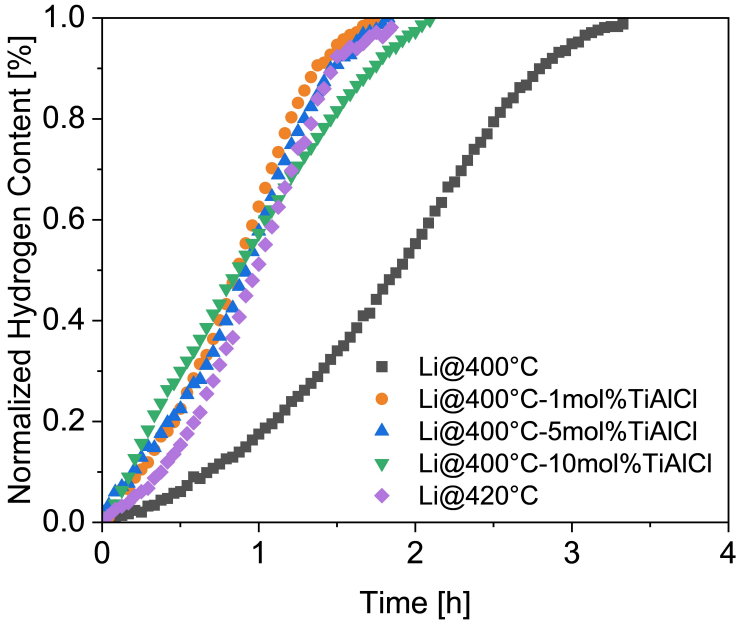

Figure 6.2.: Min-max normalized hydrogen release over time relating to the second dehydrogenation step, namely the reaction between Mg and $LiBH_4$. It turns out that 90 % of H_2 was released within one and half an hour in presence of additives or with a higher annealing temperature, whereas it took around three hours in absence of additives at a lower annealing temperature. Kinetics measurements were performed by Yuanyuan Shang at Hereon.

$$\alpha = 1 - \exp\left[-(\mathrm{kt})^{\mathrm{n}}\right] \tag{6.5}$$

In the equation above, α denotes the fraction of released hydrogen over time, and can be also used to represent the change in volume fraction of MgB_2 in this case. k denotes the reaction rate constant and n refers to the Avrami exponent. The Avrami exponent serves as an informative indicator for understanding the behavior of materials, since it is capable of providing information on the nucleation mode, dimensionality of growth, and growth mode [105, 109]. The Avrami exponent n can be expressed as d/m. d represents the dimensionality of crystal growth, with the conditions that $1 \leq \mathrm{d} \leq 2$ referring to one-dimensional growth (e.g., needle), $2 \leq \mathrm{d} \leq 3$ referring to two-dimensional growth (e.g., platelet and sheet), and $3 \leq \mathrm{d} \leq 4$ referring to three-dimensional growth (e.g., sphere). m indicates the growth mode, i.e. the rate-controlling step for the phase transformation, with m = 1 referring to the interface-controlled growth, and m = 2 representing the diffusion-controlled growth.

As introduced in Section 2.4, by plotting $\ln[-\ln(1-\alpha)]$ against $\ln(t)$ according to Equation 2.7, the Avrami exponent n can be immediately determined by the slope of the plot. To maintain consistency and interpretability of the analysis, the hydrogen release fraction α ranging from 15 % to 85 % was selected for the plot and the determination of the Avrami exponent n, which are displayed in Figure 6.3a and b, respectively. Based on the TEM observations of bar-shaped and platelet-shaped MgB_2 crystals, the growth of MgB_2 is supposed to be two-dimensional in both cases, as a significantly restricted growth was determined along the c-axis of MgB_2. Therefore, the dimensionality d should be located between 2 and 3. It turns out that the Avrami exponent was determined to be 2.31 in the absence of additives, suggesting that the MgB_2 growth is interface-controlled (m = 1). Since only the heterogeneous nucleation of MgB_2 based on Mg is expected in this case, the growth of the MgB_2 crystals with a rectangular bar-shaped morphology is thus considered as interface-controlled. In presence of 10 mol% $3TiCl_3{\cdot}AlCl_3$, the Avrami exponent was reduced to 1.29, indicating the diffusion-controlled (m = 2) growth for MgB_2. Considering the overdose of 10 mol% $3TiCl_3{\cdot}AlCl_3$, it is anticipated that only the heterogeneous nucleation of MgB_2 based on TiB_2 occurred. Therefore, the growth of the MgB_2 crystals with a hexagonal platelet-shaped morphology is regarded as diffusion-controlled.

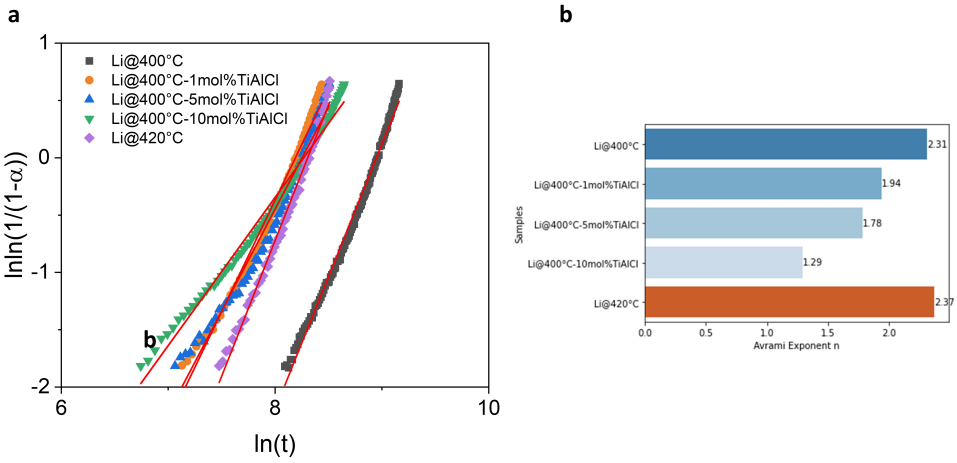

Figure 6.3.: (a) JMAK plots of lnln(1/(1-α)) vs. ln(t) with the normalized hydrogen release α ranging from 15 % to 85 % for the relevant samples. (b) the corresponding Avrami exponent n. Kinetics measurements were performed by Yuanyuan Shang at Hereon.

The Avrami exponents ranging between 1.5 and 2 for the sample in the presence of 1 or 5 mol% $3TiCl_3{\cdot}AlCl_3$ are indicative of a combination of interface-controlled and diffusion-controlled modes for the growth of MgB_2. This combination of two growth modes is supported by the observation of MgB_2 crystals with a bar-shaped morphology for the sample with 1 mol% $3TiCl_3{\cdot}AlCl_3$ (see Figure 5.20). Although the presence of MgB_2 with a bar-shaped morphology

was not observed for the sample with 5 mol% $3TiCl_3 \cdot AlCl_3$, the contribution of heterogeneous nucleation of MgB_2 based on Mg may not be disregarded. At an annealing temperature of 420 °C, the TEM observation of MgB_2 crystals with a platelet-shaped morphology implies a facilitated nucleation and growth for MgB_2 at the interface with Mg. However, this is contradicted by the Avrami exponent which was determined to be 2.37, still suggesting a interface-controlled growth for MgB_2.

As introduced in Subsection 2.4.1, in interface-controlled growth, the rate-limiting step for the phase transformation is related to the growth of interfaces or boundaries between the two phases. In diffusion-controlled growth, the rate-limiting step for the phase transformation is related to the diffusion of atoms or molecules to the growth front of the forming phase. The interface-controlled growth determined for MgB_2 based on Mg indicates the limited growth of MgB_2 at the MgB_2-Mg interface. This limitation is supported by the determination of a large elastic strain energy density for MgB_2 to form in the in-plane directions at the MgB_2-Mg interface, resulting in the formation of the bar-shaped morphology for MgB_2. When TiB_2 (and AlB_2) is present and acts as the nucleation center for MgB_2, which is generated during the ball milling process, the required elastic strain energy density for MgB_2 at the MgB_2-TiB_2 interface is significantly reduced. Consequently, apart from the c-axis direction of MgB_2, there are no limitations for the nucleation and growth of MgB_2, leading to the formation of a hexagonal platelet-shaped morphology. Following the release of the MgB_2-TiB_2 interface limitation, the rate-limiting step for MgB_2 growth transitions from interface-controlled to diffusion-controlled. In other words, the growth rate of MgB_2 primarily depends on the diffusion speed of B and Mg atoms towards the MgB_2-TiB_2 interface.

In general, both temperature and cycling affect the nucleation and growth of MgB_2. By increasing the temperature from 400 °C to 420 °C during the dehydrogenation of $LiBH_4$-MgH_2, the incubation plateau is shortened, indicating an acceleration of MgB_2 nucleation. Furthermore, instead of MgB_2 bars observed at 400 °C, MgB_2 platelets were observed at 420 °C, suggesting an energetic relaxation of MgB_2 growth along interfacial directions based on Mg grains. During cycling of LiH-MgB_2, after dehydrogenation, thick MgB_2 platelets without parallelism were observed, in contrast to the thin MgB_2 platelets with parallel orientation observed in the presence of additives. This can be attributed to the residual MgB_2 grains during cycling acting as nucleation centers. Similarly, in the sodium system, parallel-oriented MgB_2 platelets were observed, indicating that both the sodium and lithium systems are likely to share the same mechanism for the generation of MgB_2. According to modeling associated with the JMAK equation, the rate-limiting step for MgB_2 growth is determined. The growth of MgB_2 based on Mg is interface-controlled, while the growth based on TiB_2 is diffusion-controlled. This is consistent with the variation in elastic strain energy density determined for MgB_2 with respect to Mg and TiB_2.

6.3. Image of MgB_2 Nucleation and Growth

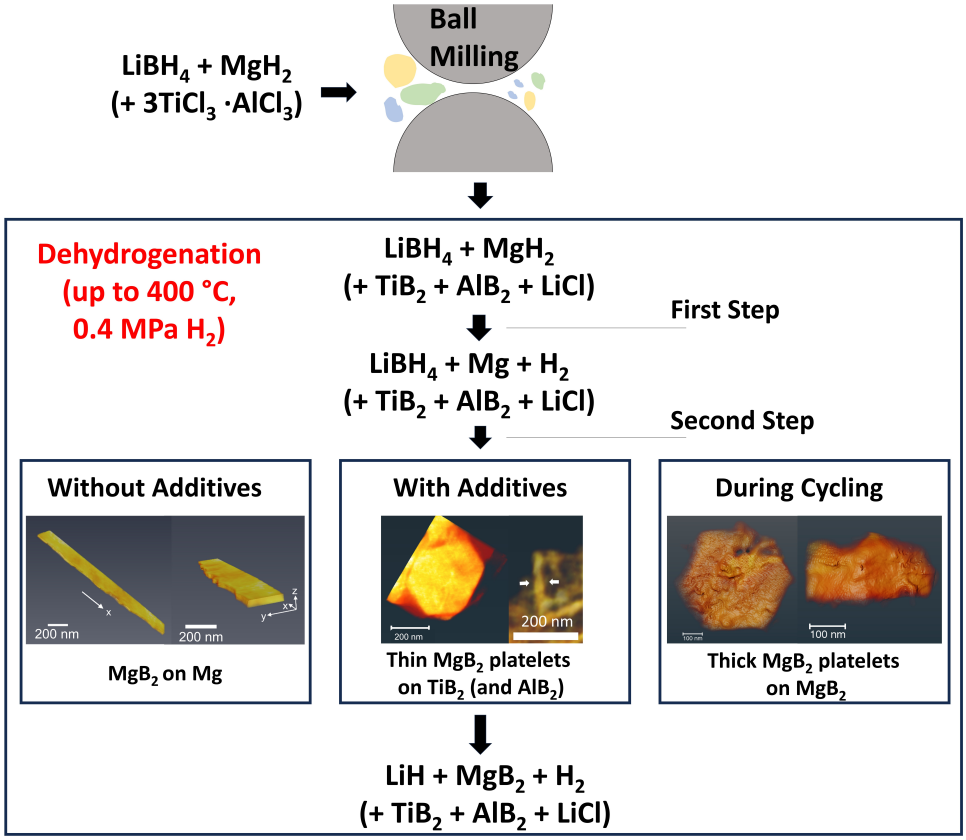

Figure 6.4.: A schematic illustration depicting the MgB_2 nucleation and growth following the chemical reaction of $LiBH_4$-MgH_2 dehydrogenation, with respect to different nucleation centers.

As discussed, the nucleation and growth of MgB_2 can be influenced by the selection of nucleation centers, as illustrated in Figure 6.4. In the absence of additives, parallel-oriented MgB_2 bars were observed after dehydrogenation at 400 °C and 0.4 MPa H_2 of $LiBH_4$-MgH_2. In this case, Mg serves as the nucleation center. By incorporating $3TiCl_3{\cdot}AlCl_3$ as additives, a reaction between $LiBH_4$ and $TiCl_3$ (and $AlCl_3$) occurs during ball milling, resulting in the formation of TiB_2, AlB_2, and $LiCl$. The generated TiB_2 (and AlB_2) nanoparticles are considered as new nucleation centers for MgB_2, requiring significantly less elastic strain energy density compared to nucleation on Mg. This is evidenced by the improved dehydrogenation kinetics and the observation of parallel-oriented MgB_2 platelets. Regarding the MgB_2 crystals generated

during cycling of LiH-MgB_2, thick MgB_2 platelets without parallelism were observed. Given the significant improvement in dehydrogenation kinetics during cycling, the absence of parallel orientation in the MgB_2 crystals, and their increased thickness, the presence of residual MgB_2 grains is considered another nucleation centers.

In summary, various factors such as temperature, cycling, and the incorporation of additives during the dehydrogenation process of reactive hydride composites (Li-based and Na-based) have a substantial influence on the formation and morphology of MgB_2. This influence is reflected in the change in MgB_2's morphology. The morphological changes observed are correlated to the necessary elastic strain energy density at the interface between MgB_2 and its nucleation centers, which affects the kinetics performance.

7. Summary and Outlook

Among a variety of advanced materials for hydrogen storage, $LiBH_4$-MgH_2 is recognized as one of the most promising candidates for practical applications. This is primarily due to its high gravimetric hydrogen storage capacity, which is approximately 12 wt%. However, the sluggish dehydrogenation kinetics is a significant challenge for this material. This challenge is evidenced by the prolonged incubation plateau lasting for several hours. This incubation plateau is assigned to the slow formation of MgB_2, resulting from the dehydrogenation process of $LiBH_4$-MgH_2. However, the mechanism underlying the formation of MgB_2 remains unclear. The objective of this study is to thoroughly investigate the nucleation and growth of MgB_2 on a nanoscale under different conditions, utilizing advanced transmission electron microscopy techniques. Through comprehensive analysis, this work aims to elucidate the essential mechanisms that enhance the kinetics of reactive hydride composites (Li-RHCs and Na-RHCs). The determination of the underlying mechanisms will aid in selecting appropriate parameters for future reactive hydride composites.

In the absence of additives, the prolonged dehydrogenation of $LiBH_4$-MgH_2 at 400 °C resulted in the formation of MgB_2 crystals with a rectangular bar-shaped morphology (shown by electron tomography). This was attributed to heterogeneous nucleation of MgB_2 on the Mg surface. This relation was demonstrated by studying the intermediate states of $LiBH_4$-MgH_2 during dehydrogenation using 4D-STEM. These MgB_2 crystals exhibited predominant growth perpendicular to the MgB_2-Mg interface. To assess the effect of transition metal-based additives on the kinetics of Li-RHCs, $3TiCl_3{\cdot}AlCl_3$ was selected for its cost-efficiency and significant impact on kinetics. When $3TiCl_3{\cdot}AlCl_3$ additives were present, the resulting morphology of the MgB_2 crystals are hexagonal platelets (as evidenced by electron tomography). This change in morphology was observed to occur due to the presence of TiB_2 (and AlB_2) nanoparticles, which were found to be generated from the reaction between $LiBH_4$ and $3TiCl_3{\cdot}AlCl_3$ during the ball milling process (HRTEM and EELS). It was concluded that these newly formed TiB_2 (and AlB_2) nanoparticles acted as nucleation centers, facilitating the formation of MgB_2.

To gain a deeper understanding of how these nucleation centers contribute to the nucleation of MgB_2, the crystal orientations of MgB_2 were determined in relation to their corresponding morphology (4D-STEM and electron tomography). The study revealed a strong restriction for both

MgB_2 bars and platelets to grow along the $\langle 0\,0\,0\,2\rangle_{MgB_2}$ orientation. Additionally, a predominant growth direction was identified for MgB_2 bars, which is perpendicular to the connected region between MgB_2 bars and aligns with the $\langle 1\,\bar{2}\,1\,0\rangle_{MgB_2}$ orientation. In contrast, no predominant growth direction was observed for MgB_2 platelets, although the direction perpendicular to the connected region between MgB_2 platelets was determined to be $\langle 1\,0\,\bar{1}\,0\rangle_{MgB_2}$. In this context, the connected region between MgB_2 crystals was considered as the area where either the MgB_2-Mg or the MgB_2-TiB_2 interface was present.

The edge-to-edge matching model was utilized to elucidate the orientation relationships between MgB_2 and the nucleation centers. In the absence of additives, the formation of MgB_2 in the in-plane directions at the MgB_2-Mg interface necessitates an elastic strain energy density of 2.9 $\times$ 10^8 J/m^3 along the $\langle 1\,0\,\bar{1}\,0\rangle_{MgB_2}$ orientation. However, with the introduction of TiB_2 additives, the energy requirement for MgB_2 formation in the in-plane directions at the MgB_2-TiB_2 interface is significantly reduced to 4.7 $\times$ 10^7 J/m^3 along the $\langle 1\,\bar{2}\,1\,0\rangle_{MgB_2}$ (or $\langle 1\,0\,\bar{1}\,0\rangle_{MgB_2}$) orientation. These findings indicate that the nucleation of MgB_2 on TiB_2 necessitates an elastic strain energy density that is approximately 6.2 times smaller than that on Mg, significantly enhancing the dehydrogenation kinetics. This substantial energy difference accounts for the prevalence of rectangular bar-shaped MgB_2 crystals perpendicular to the MgB_2-Mg interface (out-of-plane growth), as the in-plane growth of MgB_2 at the MgB_2-Mg interface requires significantly higher energy. Conversely, when the required energy density is lowered through the introduction of the MgB_2-TiB_2 interface, the in-plane growth of MgB_2 is once again energetically favored, resulting in the formation of hexagonal platelet-shaped MgB_2 crystals. The interface between MgB_2 and the corresponding nucleation centers, where the MgB_2 formation occurs, thus plays a crucial role to affect the kinetics. The observed morphological change, coupled with the decrease in required elastic strain energy density due to the presence of additives, is consistent with the identified transition in the rate-limiting step for MgB_2 growth, as determined by JMAK modeling. The shift from interface-controlled growth to diffusion-controlled growth of MgB_2 upon additive introduction signifies the reduction in interface restrictions for the MgB_2 growth.

Temperature is another key factor that influences the dehydrogenation kinetics of RHCs. While the theoretical dehydrogenation temperature for $LiBH_4$-MgH_2 is estimated to be around 225 °C, a higher temperature of 400 °C is required to ensure the completion of the dehydrogenation process within a reasonable time frame in practice. This suggests that $LiBH_4$ has to be in a liquid state, and thus above its melting point of 277 °C. This significantly enhances the motion of $LiBH_4$. By increasing the temperature from 400 °C to 420 °C for dehydrogenation, the in-plane nucleation and growth of MgB_2 on Mg are found to be effectively facilitated. This is reflected in a shortened incubation plateau and the transition of MgB_2 morphology from bar-shaped to platelet-shaped. However, the preservation of the incubation plateau suggests that the formation of MgB_2 is still limited by the interface between MgB_2 and Mg. This is supported by JMAK modelling, which

shows that the MgB_2 growth remains to be interface-controlled, suggesting the MgB_2 growth at the interface being the rate-limiting step. Furthermore, it was observed that the dehydrogenation kinetics is significantly improved during the cycling of LiH-MgB_2. This was attributed to the occurrence of heterogeneous nucleation of MgB_2 relying on the residual MgB_2 nuclei. Although the MgB_2 generated relying on the residual MgB_2 shows a hexagonal platelet-shaped morphology as the MgB_2 generated from heterogeneous nucleation based on TiB_2, but a significantly larger thickness for the platelets was observed. Moreover, the addition of $3TiCl_3{\cdot}AlCl_3$ can further improve the kinetics during cycling, reflected in the reduced duration of only about half an hour for both hydrogenation and dehydrogenation.

$NaBH_4$-MgH_2 was investigated to ascertain whether different reactive hydride composites share the same underlying mechanism controlling MgB_2 formation and influencing dehydrogenation kinetics.To complete dehydrogenation of $NaBH_4$-MgH_2 within a reasonable time frame, a high temperature of 450 °C is applied, surpassing the theoretical dehydrogenation temperature of 350 °C. This necessity may also arise from the requirement of $NaBH_4$ to be in a liquid state, which has a melting point of 400 °C. Following the dehydrogenation process, similar platelet-shaped MgB_2 crystals aligned in a parallel orientation were observed in Na-RHCs. This observation indicates that both Li- and Na-RHCs share a common underlying mechanism for MgB_2 formation, which impacts their kinetic performance. Moreover, the incomplete dehydrogenation process observed in the in situ TEM studies conducted on $NaBH_4$-MgH_2 indicates the need for further optimization of the operating conditions for $NaBH_4$-MgH_2 within the TEM environment (in-situ TEM with environment system).

In summary, it is suggested here that the occurrence of heterogeneous nucleation of MgB_2 relying on MgB_2 and TiB_2 simultaneously might be a solution for a further improvement in the kinetics for practical applications of $LiBH_4$-MgH_2, $NaBH_4$-MgH_2 and other RHCs, whose kinetics performance primarily depends on the formation of MgB_2. With that being said, a ball-milled mixture of MgB_2, and some qualified additives that requires a low energy density for the heterogeneous nucleation of MgB_2 might be promising for further study. Additionally, utilizing a lightweight scaffold, which can also affect the melting point of hydrogen storage materials [119, 178, 179], allows for the mixture to effectively minimize agglomeration and ensure a fine distribution of MgB_2. This is supposed to be an effective complement to further optimize the heterogeneous nucleation of MgB_2 based on the residual MgB_2 during long-term cycling. It can be also anticipated that a higher temperature introduces the benefit of fulfilling the required elastic strain energy density determined by the nucleation center, or in other words, overcoming the activation energy. However, for practical applications, especially for on-board utilization, such high temperatures may not be practical and efficient. Further investigation is thus required to determine the necessity of $LiBH_4$ (or $NaBH_4$) being in a liquid phase for accelerating the dehydrogenation process. Moreover, it is necessary to optimize the operating conditions further

to successfully advance the dehydrogenation of $NaBH_4$-MgH_2 within the TEM environment in future research, allowing for a more comprehensive understanding of reactive hydride composites at the nanoscale.

A. Appendix

2Theta [°]	d-spacing [Å]	Intensity	h	k	l
17.949	4.938	12047.33	1	0	1
23.925	3.7164	17304.14	0	1	1
24.785	3.5893	9457.71	2	0	0
26.177	3.4016	7647.99	0	0	2
26.995	3.3003	13617.4	1	1	1
28.086	3.1746	44.4	2	0	1
29.025	3.074	2749.38	1	0	2
32.048	2.7905	752.73	2	1	0
34.718	2.5818	2021.29	2	1	1
35.499	2.5268	2472.39	1	1	2
36.358	2.469	2102.87	2	0	2
39.906	2.2573	3247.19	3	0	1
40.636	2.2184	4219.1	0	2	0
41.737	2.1624	8.91	1	0	3
41.837	2.1574	105.07	2	1	2
44.749	2.0236	2844.36	1	2	1
44.85	2.0193	4211.12	0	1	3
45.024	2.0119	658.04	3	1	1
46.356	1.9571	548.02	3	0	2
46.692	1.9438	742.02	1	1	3
47.381	1.9171	363.74	2	0	3
48.183	1.8871	1026.72	2	2	0
48.981	1.8582	683.79	0	2	2

50.708	1.7989	3.49	1	2	2
50.836	1.7946	229.01	4	0	0
50.958	1.7907	3827.18	3	1	2
51.914	1.7599	2854.48	2	1	3
52.707	1.7353	6.42	4	0	1
53.86	1.7008	249.13	0	0	4
55.162	1.6637	35.03	4	1	0
55.478	1.655	380.05	1	0	4
55.654	1.6502	478.38	2	2	2
55.807	1.646	4.76	3	0	3
56.933	1.6161	143.54	4	1	1
58.064	1.5873	3.9	4	0	2
58.267	1.5822	3585.34	3	2	1
59.573	1.5506	209.01	1	1	4
59.664	1.5485	1.22	1	2	3
59.888	1.5432	7.53	3	1	3
60.156	1.537	135.48	2	0	4
62.05	1.4945	225.11	4	1	2
63.318	1.4676	320.94	3	2	2
64.065	1.4523	382.97	2	1	4
64.152	1.4505	8.3	2	2	3
64.418	1.4452	402.17	0	3	1
65.872	1.4168	72.06	1	3	1
66.373	1.4073	56.98	4	0	3
66.507	1.4048	317.75	5	0	1
67.02	1.3953	77.96	4	2	0
67.512	1.3863	249.22	3	0	4
68.572	1.3674	16.9	2	3	0
68.607	1.3668	7.82	4	2	1
69.597	1.3498	191.69	0	2	4
70.093	1.3414	38.45	4	1	3
70.142	1.3406	162.54	2	3	1

70.223	1.3393	163.62	5	1	1
70.369	1.3368	98.62	1	0	5
70.618	1.3327	385.48	1	3	2
70.998	1.3265	118.53	1	2	4
71.203	1.3232	1047.11	3	1	4
71.233	1.3227	106	5	0	2
72.62	1.3008	226.35	0	1	5
73.997	1.28	7.47	1	1	5
74.521	1.2723	60.68	2	0	5
74.765	1.2687	45	2	3	2
74.845	1.2676	541.45	5	1	2
75.137	1.2634	102.71	2	2	4
76.898	1.2388	653.23	0	3	3
77.024	1.2371	155.62	3	3	1
77.215	1.2345	37.17	4	0	4
78.077	1.223	252.09	2	1	5
78.249	1.2207	113.86	1	3	3
78.842	1.213	9.01	5	0	3
80.156	1.1964	188.06	6	0	0
80.734	1.1893	29.6	4	1	4
80.814	1.1883	196.67	4	2	3
80.938	1.1868	561.12	5	2	1
81.273	1.1828	342.06	3	0	5
81.511	1.1799	1098.54	3	3	2
81.644	1.1783	70	6	0	1
81.873	1.1756	245.95	3	2	4
82.266	1.171	529.27	2	3	3
82.344	1.1701	42.79	5	1	3
83.646	1.1552	305.5	6	1	0
84.558	1.145	164.95	1	2	5
84.753	1.1429	122.23	3	1	5
84.895	1.1413	56.59	4	3	0

85.122	1.1389	162	6	1	1
85.378	1.1361	200.25	5	2	2
85.587	1.1339	298.87	0	0	6
86.078	1.1287	75.99	6	0	2
86.368	1.1256	23.86	4	3	1
86.909	1.12	187.43	1	0	6
87.968	1.1092	399.15	0	4	0
88.525	1.1037	154.64	2	2	5
88.615	1.1028	125.65	1	3	4
88.887	1.1001	3.18	3	3	3
89.196	1.0971	7.53	5	0	4
89.535	1.0938	187.88	6	1	2

Table A1.: Reflection parameters of $LiBH_4$ with a space group of Pnma(62)-orthorhombic, and lattice constants of a = 7.1786 Å, b = 4.4369 Å and c = 6.8032 Å, based on Cu K_α wit λ = 1.54184 Å [163].

Table A2.: Reflection parameters of MgH_2 with a space group of group P 42/mnm(136)-tetragonal , and lattice constants of a = 4.5147 Å and c = 3.0193 Å, based on Cu K_α wit λ = 1.54184 Å [180].

2Theta [°]	d-spacing [Å]	Intensity	h	k	l
27.926	3.1924	22129.47	1	1	0
35.748	2.5098	20949.05	0	1	1
39.905	2.2573	7110.16	0	2	0
41.116	2.1936	117.38	1	1	1
44.856	2.019	31.33	1	2	0
54.64	1.6784	13415.31	1	2	1
57.709	1.5962	2913.87	2	2	0
61.361	1.5096	1230.76	0	0	2
65.306	1.4277	3501.93	1	3	0
66.169	1.4111	1.22	2	2	1
68.725	1.3647	3067.66	1	1	2
69.768	1.3469	3109.2	0	3	1
73.286	1.2907	1.98	1	3	1
75.736	1.2549	2083.54	0	2	2
79.154	1.209	1.74	1	2	2
83.516	1.1566	3161.83	2	3	1
86.076	1.1287	771.51	0	4	0
89.226	1.0968	1442.21	2	2	2
89.415	1.095	1.04	1	4	0

Table A3.: Reflection parameters of Mg with a space group of P63/mmc(194)-hexagonal, and lattice constants of a = 3.2200 Å and c = 5.2300 Å, based on Cu K_α wit λ = 1.54184 Å [181].

2Theta [°]	d-spacing [Å]	Intensity	h	k	l
32.071	2.7886	5715.02	0	1	0
34.263	2.615	6358.77	0	0	2
36.486	2.4607	24029.94	0	1	1
47.635	1.9075	3678.38	0	1	2
57.168	1.61	4140.92	-1	2	0
62.811	1.4782	4560.3	0	1	3
67.072	1.3943	612.33	0	2	0
68.369	1.371	4592.11	-1	2	2
69.746	1.3472	3224.04	0	2	1
72.192	1.3075	640.71	0	0	4
77.524	1.2303	768.61	0	2	2
81.186	1.1838	668.34	0	1	4

Table A4.: Reflection parameters of LiH with a space group of Fm-3m(225)-cubic, and a lattice constant of a = 4.0834 Å, based on Cu K_α wit λ = 1.54184 Å [182].

2Theta [°]	d-spacing [Å]	Intensity	h	k	l
38.142	2.3576	1645.76	1	1	1
44.331	2.0417	2249.75	0	0	2
64.493	1.4437	1173.16	0	2	2
77.46	1.2312	850.51	1	1	3
81.608	1.1788	344.77	2	2	2

Table A5.: Reflection parameters of MgB_2 with a space group of P6/mmm(191)-hexagonal, and lattice constants of a = 3.0851 Å and c = 3.5201 Å, based on Cu K_α wit λ = 1.54184 Å [183].

2Theta [°]	d-spacing [Å]	Intensity	h	k	l
25.281	3.5201	299.45	0	0	1
33.514	2.6718	2353.08	0	1	0
42.44	2.1282	8610.23	0	1	1
51.909	1.7601	1110.65	0	0	2
59.916	1.5425	2068.6	-1	2	0
63.214	1.4698	808.12	0	1	2
66.078	1.4128	286.41	-1	2	1
70.426	1.3359	280.14	0	2	0
76.158	1.249	1311.13	0	2	1
82.065	1.1734	21.28	0	0	3
83.213	1.1601	1516.12	-1	2	2

Table A6.: Reflection parameters of LiCl with a space group of Fm-3m(225)-cubic, and a lattice constant of a = 5.143 Å, based on Cu K_α wit λ = 1.54184 Å [184].

2Theta [°]	d-spacing [Å]	Intensity	h	k	l
30.071	2.9693	217241.3	1	1	1
34.861	2.5715	182261.9	0	0	2
50.128	1.8183	112182	0	2	2
59.571	1.5507	66406.3	1	1	3
62.509	1.4847	36169.67	2	2	2
73.612	1.2858	16506.55	0	0	4
81.515	1.1799	27456.15	1	3	3
84.106	1.15	47260.25	0	2	4

Table A7.: Reflection parameters of MgO with a space group of Fm-3m(225)-cubic, and a lattice constant of a = 4.214 Å, based on Cu K_α wit λ = 1.54184 Å [185].

2Theta [°]	d-spacing [Å]	Intensity	h	k	l
36.916	2.433	7777.59	1	1	1
42.888	2.107	110288.8	0	0	2
62.266	1.4899	58788.02	0	2	2
74.64	1.2706	7417.25	1	1	3
78.576	1.2165	17186.04	2	2	2

Table A8.: Reflection parameters of TiB_2 with a space group of P6/mmm(191)-hexagonal, and lattice constants of a = 3.0325 Å and c = 3.2313 Å, based on Cu K_α wit λ = 1.54184 Å [186].

2Theta [°]	d-spacing [Å]	Intensity	h	k	l
27.583	3.2313	3115.28	0	0	1
34.113	2.6262	10002.99	0	1	0
44.416	2.038	18828.34	0	1	1
56.95	1.6157	1796.74	0	0	2
61.065	1.5163	4271.99	-1	2	0
68.08	1.3761	2526.97	0	1	2
68.275	1.3726	1683.53	-1	2	1
71.835	1.3131	1060.34	0	2	0
78.575	1.2165	3023.01	0	2	1
88.328	1.1056	2944.4	-1	2	2

Table A9.: Reflection parameters of AlB_2 with a space group of P6/mmm(191)-hexagonal, and lattice constants of a = 3.016 Å and c = 3.268 Å, based on Cu K_α wit λ = 1.54184 Å.

2Theta [°]	d-spacing [Å]	Intensity	h	k	l
27.267	3.268	270.5	0	0	1
34.305	2.6119	2408.62	0	1	0
44.362	2.0403	8117.13	0	1	1
56.253	1.634	931.7	0	0	2
61.435	1.508	2107.09	-1	2	0
67.569	1.3853	810.19	0	1	2
68.467	1.3693	357.73	-1	2	1
72.29	1.306	327.42	0	2	0
78.867	1.2127	1385.27	0	2	1
88.07	1.1082	1531.9	-1	2	2

Table A10.: Reflection parameters of $NaBH_4$ with a space group of Fm-3m(225)-cubic, and a lattice constant of a = 6.1453 Å, based on Cu K_α wit λ = 1.54184 Å.

2Theta [°]	d-spacing [Å]	Intensity	h	k	l
25.079	3.548	43095.18	1	1	1
29.038	3.0726	219136.9	0	0	2
41.53	2.1727	138252.6	0	2	2
49.131	1.8529	53781.2	1	1	3
51.471	1.774	44680.67	2	2	2
60.185	1.5363	16120.43	0	0	4
66.238	1.4098	15695.34	1	3	3
68.191	1.3741	48708.97	0	2	4
75.77	1.2544	35031.09	2	2	4
81.284	1.1827	2611.75	3	3	3
81.284	1.1827	8666.21	1	1	5

Table A11.: Reflection parameters of NaH with a space group of Fm-3m(225)-cubic, and a lattice constants of a = 4.8900 Å, based on Cu K_α wit λ = 1.54184 Å.

2Theta [°]	d-spacing [Å]	Intensity	h	k	l
31.667	2.8232	100014.3	1	1	1
36.728	2.445	64967.36	0	0	2
52.917	1.7289	39409.73	0	2	2
62.994	1.4744	37457.84	1	1	3
66.143	1.4116	11702.18	2	2	2
78.115	1.2225	4846.62	0	0	4
86.729	1.1218	12994.51	1	3	3
89.574	1.0934	12777.94	0	2	4

B. Appendix

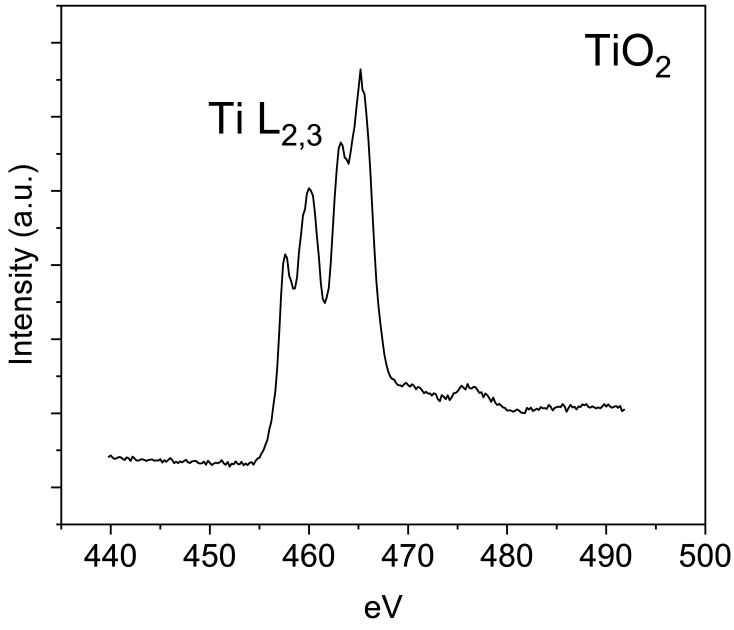

Figure A1.: EELS edges of Ti $L_{2,3}$ in TiO_2 [187].

List of Figures

List of Tables

List of Publication

[1] Jin, Ou ; Shang, Yuanyuan ; Huang, Xiaohui ; Mu, Xiaoke ; Szabó, Dorothée V. ; Le, Thi T. ; Wagner, Stefan ; Kübel, Christian ; Pistidda, Claudio ; Pundt, Astrid: Microstructural study of MgB2 in the $LiBH_4$–MgH_2 composite by using TEM. In: *Nanomaterials* 12 (2022), Nr. 11, S. 1893

[2] Jin, Ou ; Shang, Yuanyuan ; Huang, Xiaohui ; Szabó, Dorothée V. ; Le, Thi T. ; Wagner, Stefan ; Klassen, Thomas ; Kübel, Christian ; Pistidda, Claudio ; Pundt, Astrid: Transformation Kinetics of $LiBH_4$–MgH_2 for Hydrogen Storage. In: *Molecules* 27 (2022), Nr. 20, S. 7005

[3] Shang, Yuanyuan ; Jin, Ou ; Puszkiel, Julián A. ; Karimi, Fahim ; Dansirima, Palmarin ; Sittiwet, Chongsutthamani ; Utke, Rapee ; Soontaranon, Siriwat ; Le, Thi T. ; Gizer, Gökhan ; Szabó, Dorothée V. ; Wagner, Stefan ; Kübel, Christian ; Klassen, Thomas ; Dornheim, Martin ; Pundt, Astrid ; Pistidda, Claudio: Effects of metal-based additives on dehydrogenation process of $2NaBH_4 + MgH_2$ system. In: *International Journal of Hydrogen Energy* 47 (2022), Nr. 89, S. 37882–37894

Bibliography

[1] G.W. Crabtree, M.S. Dresselhaus, and M.V. Buchanan. The hydrogen economy. *Physics today*, 57(12):39–44, 2004.

[2] M. Ball and M. Wietschel. The future of hydrogen–opportunities and challenges. *International journal of hydrogen energy*, 34(2):615–627, 2009.

[3] D.J. Durbin and C. Malardier-Jugroot. Review of hydrogen storage techniques for on board vehicle applications. *International journal of hydrogen energy*, 38(34):14595–14617, 2013.

[4] H. Barthélémy, M. Weber, and F. Barbier. Hydrogen storage: Recent improvements and industrial perspectives. *International journal of hydrogen energy*, 42(11):7254–7262, 2017.

[5] A. Züttel. Hydrogen storage methods. *Naturwissenschaften*, 91(4):157–172, 2004.

[6] E. Rivard, M. Trudeau, and K. Zaghib. Hydrogen storage for mobility: a review. *Materials*, 12(12):1973, 2019.

[7] EH Kisi, CE Buckley, and EM Gray. The hydrogen activation of lani$_5$. *Journal of alloys and compounds*, 185(2):369–384, 1992.

[8] S. Orimo, Y. Nakamori, J.R. Eliseo, A. Züttel, and C.M. Jensen. Complex hydrides for hydrogen storage. *Chemical reviews*, 107(10):4111–4132, 2007.

[9] M.B. Ley, L.H. Jepsen, Y. Lee, Y.W. Cho, J.M.B. Von Colbe, M. Dornheim, M. Rokni, J.O. Jensen, M. Sloth, Y. Filinchuk, et al. Complex hydrides for hydrogen storage–new perspectives. *Materials today*, 17(3):122–128, 2014.

[10] W.M. Mueller, J.P. Blackledge, and G.G. Libowitz. *Metal hydrides*. Elsevier, 2013.

[11] B. Sakintuna, F. Lamari-Darkrim, and M. Hirscher. Metal hydride materials for solid hydrogen storage: a review. *International journal of hydrogen energy*, 32(9):1121–1140, 2007.

[12] J.J. Reilly Jr and R.H. Wiswall Jr. Reaction of hydrogen with alloys of magnesium and copper. *Inorganic chemistry*, 6(12):2220–2223, 1967.

[13] P. Chen, Z. Xiong, J. Luo, and K.L. Lin, J.and Tan. Interaction of hydrogen with metal nitrides and imides. *Nature*, 420(6913):302–304, 2002.

[14] J.J. Vajo, F. Mertens, C.C. Ahn, R.C. Bowman Jr, and B. Fultz. Altering hydrogen storage properties by hydride destabilization through alloy formation: LiH and MgH_2 destabilized with Si. *The journal of physical chemistry B*, 108(37):13977–13983, 2004.

[15] G. Barkhordarian, T. Klassen, M. Dornheim, and R. Bormann. Unexpected kinetic effect of MgB_2 in reactive hydride composites containing complex borohydrides. *Journal of alloys and compounds*, 440(1-2):L18–L21, 2007.

[16] J.J. Vajo, S.L. Skeith, and F. Mertens. Reversible storage of hydrogen in destabilized $LiBH_4$. *The journal of physical chemistry B*, 109(9):3719–3722, 2005.

[17] B. Bogdanović, K. Bohmhammel, B. Christ, A. Reiser, K. Schlichte, R. Vehlen, and U. Wolf. Thermodynamic investigation of the magnesium–hydrogen system. *Journal of alloys and compounds*, 282(1-2):84–92, 1999.

[18] P. Mauron, F. Buchter, O. Friedrichs, A. Remhof, M. Bielmann, C.N. Zwicky, and A. Züttel. Stability and reversibility of $LiBH_4$. *The journal of physical chemistry B*, 112(3):906–910, 2008.

[19] U. Bösenberg, S. Doppiu, L. Mosegaard, G. Barkhordarian, N. Eigen, A. Borgschulte, T.R. Jensen, Y. Cerenius, O. Gutfleisch, T. Klassen, et al. Hydrogen sorption properties of MgH_2-$LiBH_4$ composites. *Acta materialia*, 55(11):3951–3958, 2007.

[20] N.A. Ali, N.A. Sazelee, and M. Ismail. An overview of reactive hydride composite (rhc) for solid-state hydrogen storage materials. *International journal of hydrogen energy*, 46(62):31674–31698, 2021.

[21] M.A. Rahmaninasab, S. Raygan, H. Abdizadeh, M. Pourabdoli, and S.H. Mirghaderi. Properties of activated MgH_2 mischmetal nanostructured composite produced by ball-milling. *Materials for renewable and sustainable energy*, 7:1–11, 2018.

[22] I. Tajima, M. Abe, H. Uchida, M. Hattori, Y. Miyamoto, and T. Haraki. Hydrogen sorption kinetics of FeTi alloy with nano-structured surface layers. *Journal of alloys and compounds*, 580:S33–S35, 2013.

[23] M. Konarova, A. Tanksale, J.N. Beltramini, and G. Lu. Effects of nano-confinement on the hydrogen desorption properties of MgH_2. *Nano energy*, 2(1):98–104, 2013.

[24] J.J. Vajo. Influence of nano-confinement on the thermodynamics and dehydrogenation kinetics of metal hydrides. *Current opinion in solid state and materials science*, 15(2):52–61, 2011.

[25] B. Bogdanović and M. Schwickardi. Ti-doped alkali metal aluminium hydrides as potential novel reversible hydrogen storage materials. *Journal of alloys and compounds*, 253:1–9, 1997.

[26] M. Fan, L. Sun, Y. Zhang, F. Xu, J. Zhang, and H. Chu. The catalytic effect of additive Nb_2O_5 on the reversible hydrogen storage performances of $LiBH_4$–MgH_2 composite. *International journal of hydrogen energy*, 33(1):74–80, 2008.

[27] U. Bösenberg, J.W. Kim, D. Gosslar, N. Eigen, T.R. Jensen, J.M.B. Von Colbe, et al. Role of additives in $LiBH_4$-MgH_2 reactive hydride composites for sorption kinetics. *Acta materialia*, 58(9):3381–3389, 2010.

[28] T.T. Le, C. Pistidda, J. Puszkiel, Maria V. Castro R., F. Karimi, J. Skibsted, B. GharibDoust, S.P.and Richter, T. Emmler, C. Milanese, et al. Design of a nanometric AlTi additive for MgB_2-based reactive hydride composites with superior kinetic properties. *The journal of physical chemistry C*, 122(14):7642–7655, 2018.

[29] C.C. Nwakwuo, C. Pistidda, M. Dornheim, J.L. Hutchison, and J.M. Sykes. Microstructural study of hydrogen desorption in $2NaBH_4$+MgH_2 reactive hydride composite. *International journal of hydrogen energy*, 37(3):2382–2387, 2012.

[30] C.C. Nwakwuo, C. Pistidda, M. Dornheim, J.L. Hutchison, and J.M. Sykes. Microstructural analysis of hydrogen absorption in 2NaH+MgB_2. *Scripta materialia*, 64(4):351–354, 2011.

[31] U.S. Department of Energy. Doe technical targets for onboard hydrogen storage for light-duty vehicles. `https://www.energy.gov/eere/fuelcells/doe-technical-targets-onboard-hydrogen-storage-light-duty-vehicles`. [Accessed 2023-05-06].

[32] J.O. Abe, A. Popoola, E. Ajenifuja, and O.M. Popoola. Hydrogen energy, economy and storage: review and recommendation. *International journal of hydrogen energy*, 44(29):15072–15086, 2019.

[33] J. Yang, A. Sudik, C. Wolverton, and D.J. Siegel. High capacity hydrogen storage materials: attributes for automotive applications and techniques for materials discovery. *Chemical society reviews*, 39(2):656–675, 2010.

[34] A. Züttel, A. Remhof, A. Borgschulte, and O. Friedrichs. Hydrogen: the future energy carrier. *Philosophical transactions of the royal society A: Mathematical, physical and engineering sciences*, 368(1923):3329–3342, 2010.

[35] N. Wiberg and A.F. Holleman. Inorganic chemistry. *Academic press, California*, 2001.

[36] A. Züttel. Materials for hydrogen storage. *Materials today*, 6(9):24–33, 2003.

[37] J. Sery and P. Leduc. Fuel cell behavior and energy balance on board a hyundai nexo. *International journal of engine research*, 23(5):709–720, 2022.

[38] U.M. Nour, S. Awad, S. Yusup, and S. Sufian. Technical evaluation of current hydrogen storage technologies for vehicles. *Journal of applied sciences*, 10(12):1200–1203, 2010.

[39] W. Peschka. *Liquid hydrogen: fuel of the future*. Springer Science & Business Media, 2012.

[40] A. Midilli, M. Ay, I. Dincer, and M.A. Rosen. On hydrogen and hydrogen energy strategies: I: current status and needs. *Renewable and sustainable energy reviews*, 9(3):255–271, 2005.

[41] B. Sorensen and G. Spazzafumo. Hydrogen and fuel cells: emerging technologies and applications. 2018.

[42] R. Ströbel, J. Garche, P.T. Moseley, L. Jörissen, and G. Wolf. Hydrogen storage by carbon materials. *Journal of power sources*, 159(2):781–801, 2006.

[43] H. Cheng, Q. Yang, and C. Liu. Hydrogen storage in carbon nanotubes. *Carbon*, 39(10):1447–1454, 2001.

[44] S.S. Kaye, A. Dailly, O.M. Yaghi, and J.R. Long. Impact of preparation and handling on the hydrogen storage properties of Zn_4O (1, 4-benzenedicarboxylate) 3 (mof-5). *Journal of the american chemical society*, 129(46):14176–14177, 2007.

[45] N.L. Rosi, J. Eckert, D.T. Eddaoudi, M.and Vodak, J. Kim, M. O'Keeffe, and O.M. Yaghi. Hydrogen storage in microporous metal-organic frameworks. *Science*, 300(5622):1127–1129, 2003.

[46] M. Jordá-Beneyto, F. Suárez-García, D. Lozano-Castello, D. Cazorla-Amorós, and A. Linares-Solano. Hydrogen storage on chemically activated carbons and carbon nanomaterials at high pressures. *Carbon*, 45(2):293–303, 2007.

[47] S.P. Shet, S.S. Priya, K. Sudhakar, and M. Tahir. A review on current trends in potential use of metal-organic framework for hydrogen storage. *International journal of hydrogen energy*, 46(21):11782–11803, 2021.

[48] M. Mohan, V.K. Sharma, E.A. Kumar, and V. Gayathri. Hydrogen storage in carbon materials—a review. *Energy storage*, 1(2):e35, 2019.

[49] U.S. Department of Energy. Chemical hydrogen storage materials. `https://www.energy.gov/eere/fuelcells/chemical-hydrogen-storage-materials`. [Accessed 2023-05-06].

[50] D. Sheldon. Methanol production-a technical history. *Johnson matthey technology review*, 61(3):172–182, 2017.

[51] D. Cheddie. *Ammonia as a hydrogen source for fuel cells: a review*. InTech, 2012.

[52] T.R. Tephly. The toxicity of methanol. *Life sciences*, 48(11):1031–1041, 1991.

[53] F. Dalena, A. Senatore, A. Marino, A. Gordano, M. Basile, and A. Basile. Methanol production and applications: An overview. *Methanol*, pages 3–28, 2018.

[54] A.D. Sutton, A.K. Burrell, D.A. Dixon, E.B. Garner III, J.C. Gordon, T. Nakagawa, K.C. Ott, J.P. Robinson, and M. Vasiliu. Regeneration of ammonia borane spent fuel by direct reaction with hydrazine and liquid ammonia. *Science*, 331(6023):1426–1429, 2011.

[55] L. Klebanoff. *Hydrogen storage technology: materials and applications*. CRC Press, 2012.

[56] K.C. Kim, B. Dai, and D.S. Johnson, J.K.and Sholl. Assessing nanoparticle size effects on metal hydride thermodynamics using the wulff construction. *Nanotechnology*, 20(20):204001, 2009.

[57] A. Pundt and R. Kirchheim. Hydrogen in metals: microstructural aspects. *Annual review of materials research*, 36:555–608, 2006.

[58] C. Sachs, A. Pundt, R. Kirchheim, M.T. Winter, M.and Reetz, and D. Fritsch. Solubility of hydrogen in single-sized palladium clusters. *Physical review B*, 64(7):075408, 2001.

[59] B. Bogdanović and B. Spliethoff. Active MgH_2-Mg systems for hydrogen storage. *International journal of hydrogen energy*, 12(12):863–873, 1987.

[60] J.F. Stampfer Jr, C.E. Holley Jr, and J.F. Suttle. The magnesium-hydrogen system 1-3. *Journal of the american chemical society*, 82(14):3504–3508, 1960.

[61] A.S. Pedersen, J. Kjøller, B. Larsen, and B. Vigeholm. Magnesium for hydrogen storage. *International journal of hydrogen energy*, 8(3):205–211, 1983.

[62] A Rahwanto, Z Jalil, E Handoko, et al. Desorption properties of mechanically milled MgH_2 with double catalysts Ni and SiC. In *IOP Conference Series: Materials Science and Engineering*, volume 931, page 012012. IOP Publishing, 2020.

[63] H. Park, H. Lim, S.H. Oh, J. Park, H. Lim, and K. Kang. Tailoring ion-conducting interphases on magnesium metals for high-efficiency rechargeable magnesium metal batteries. *ACS energy letters*, 5(12):3733–3740, 2020.

[64] G. Sandrock. A panoramic overview of hydrogen storage alloys from a gas reaction point of view. *Journal of alloys and compounds*, 293:877–888, 1999.

[65] E.M. Dematteis, N. Berti, F. Cuevas, M. Latroche, and M. Baricco. Substitutional effects in TiFe for hydrogen storage: a comprehensive review. *Materials advances*, 2(8):2524–2560, 2021.

[66] D. Kim, K. Jang, and J. Lee. A review on the development of AB_2-type Zr-based laves phase hydrogen storage alloys for Ni–MH rechargeable batteries in the korea advanced institute of science and technology. *Journal of alloys and compounds*, 293:583–592, 1999.

[67] T. Kohno, S. Tsuruta, and M. Kanda. The hydrogen storage properties of new Mg_2Ni alloy. *Journal of the electrochemical society*, 143(9):L198, 1996.

[68] G. Liang, J. Huot, and R. Schulz. Hydrogen storage properties of the mechanically alloyed $LaNi_5$-based materials. *Journal of alloys and compounds*, 320(1):133–139, 2001.

[69] R.G. Pearson. The transition-metal-hydrogen bond. *Chemical reviews*, 85(1):41–49, 1985.

[70] G. Principi, F. Agresti, A. Maddalena, and S.L. Russo. The problem of solid state hydrogen storage. *Energy*, 34(12):2087–2091, 2009.

[71] L. Schlapbach and A. Züttel. Hydrogen-storage materials for mobile applications. *Nature*, 414(6861):353–358, 2001.

[72] P. Dantzer and F. Meunier. What materials to use in hydride chemical heat pumps? In *Materials Science Forum*, volume 31, pages 1–18. Trans Tech Publ, 1988.

[73] K.T. Møller, D.B. Sheppard, D.and Ravnsbæk, C.E. Buckley, E. Akiba, H. Li, and T.R. Jensen. Complex metal hydrides for hydrogen, thermal and electrochemical energy storage. *Energies*, 10(10):1645, 2017.

[74] J.A. Puszkiel. Tailoring the kinetic behavior of hydride forming materials for hydrogen storage. *Gold nanoparticles-reaching new heights*, 2018.

[75] A. Baldi, T.C. Narayan, A.L. Koh, and J.A. Dionne. In situ detection of hydrogen-induced phase transitions in individual palladium nanocrystals. *Nature materials*, 13(12):1143–1148, 2014.

[76] J.E. Lennard-Jones. Processes of adsorption and diffusion on solid surfaces. *Transactions of the faraday society*, 28:333–359, 1932.

[77] R.B. Schwarz and A.G. Khachaturyan. Thermodynamics of open two-phase systems with coherent interfaces: Application to metal–hydrogen systems. *Acta materialia*, 54(2):313–323, 2006.

[78] J.H. Van't Hoff. *Etudes de dynamique chimique*, volume 1. Muller, 1884.

[79] S. Orimo, Y. Nakamori, G. Kitahara, K. Miwa, N. Ohba, S. Towata, and A. Züttel. Dehydriding and rehydriding reactions of $LiBH_4$. *Journal of alloys and compounds*, 404:427–430, 2005.

[80] T. Nakagawa, T. Ichikawa, N. Hanada, Y. Kojima, and H. Fujii. Thermal analysis on the Li–Mg–B–H systems. *Journal of alloys and compounds*, 446:306–309, 2007.

[81] W. Oelerich. Sorptionseigenschaften von nanokristallinen metallhydriden fur die wasserstoffspeicherung (vom promotionsausschuss der technischen universitat hamburg-harburg als dissertation angenommene arbeit). *GKSS FORSCHUNGSZENTRUM GEESTHACHT GMBH-PUBLICATIONS-E*, 1(29):ALL–ALL, 1998.

[82] N. Ohba, K. Miwa, M. Aoki, T. Noritake, S. Towata, Y. Nakamori, S. Orimo, and A. Züttel. First-principles study on the stability of intermediate compounds of $LiBH_4$. *Physical review B*, 74(7):075110, 2006.

[83] U. Boesenberg, D.B. Ravnsbæk, H. Hagemann, V. D'Anna, C.B. Minella, C. Pistidda, W. Van Beek, T.R. Jensen, R. Bormann, and M. Dornheim. Pressure and temperature influence on the desorption pathway of the $LiBH_4$-MgH_2 composite system. *The journal of physical chemistry C*, 114(35):15212–15217, 2010.

[84] J.J. Vajo, T.T. Salguero, A.F. Gross, S.L. Skeith, and G.L. Olson. Thermodynamic destabilization and reaction kinetics in light metal hydride systems. *Journal of alloys and compounds*, 446:409–414, 2007.

[85] Thi Thu Le. *Tailoring the hydrogen sorption properties of the system $2LiBH_4 + MgH_2/2LiH + MgB_2$*. PhD thesis, Universitätsbibliothek der HSU/UniBwH, 2019.

[86] K. Kim, J. Shim, S. Park, I. Choi, K.H. Oh, and Y.W. Cho. Dehydrogenation reaction pathway of the $LiBH_4$-MgH_2 composite under various pressure conditions. *The journal of physical chemistry C*, 119(18):9714–9720, 2015.

[87] P. Chen and M. Zhu. Recent progress in hydrogen storage. *Materials today*, 11(12):36–43, 2008.

[88] P.E. de Jongh and P. Adelhelm. Nanosizing and nanoconfinement: new strategies towards meeting hydrogen storage goals. *ChemSusChem*, 3(12):1332–1348, 2010.

[89] E. Deprez, A. Justo, T.C. Rojas, C. López-Cartés, C.B. Minella, U. Bösenberg, M. Dornheim, R.U. Bormann, and A. Fernández. Microstructural study of the $LiBH_4$–MgH_2 reactive hydride composite with and without Ti-isopropoxide additive. *Acta materialia*, 58(17):5683–5694, 2010.

[90] Y. Yan, H. Li, H. Maekawa, K. Miwa, S. Towata, and S. Orimo. Formation of intermediate compound $Li_2B_{12}H_{12}$ during the dehydrogenation process of the $LiBH_4$–MgH_2 system. *The journal of physical chemistry C*, 115(39):19419–19423, 2011.

[91] Ulrike Bösenberg. *$LiBH_4$-MgH_2 composites for hydrogen storage*. PhD thesis, Technische Universität Hamburg, 2009.

[92] S. Orimo, Y. Nakamori, and A. Züttel. Material properties of MBH_4 (M= Li, Na, and K). *Materials science and engineering: B*, 108(1-2):51–53, 2004.

[93] N.N. Greenwood and A. Earnshaw. *Chemistry of the Elements*. Elsevier, 2012.

[94] P. Martelli, R. Caputo, A. Remhof, P. Mauron, A. Borgschulte, and A. Zuttel. Stability and decomposition of $NaBH_4$. *The journal of physical chemistry C*, 114(15):7173–7177, 2010.

[95] W.M. Haynes. *CRC handbook of chemistry and physics*. CRC press, 2016.

[96] Marcello Baricco, Mauro Palumbo, Eugenio Pinatel, Marta Corno, and Piero Ugliengo. Thermodynamic database for hydrogen storage materials. *Advances in Science and Technology*, 72:213–218, 2011.

[97] T. Czujko, R.A. Varin, Z. Wronski, Z.S. Zaranski, and T. Durejko. Synthesis and hydrogen desorption properties of nanocomposite magnesium hydride with sodium borohydride (mgh_2-$nabh_4$). *Journal of alloys and compounds*, 427(1-2):291–299, 2007.

[98] S. Garroni, C. Milanese, A. Girella, A. Marini, G. Mulas, E. Menéndez, C. Pistidda, M. Dornheim, S. Suriñach, and M.D. Baró. Sorption properties of $NaBH_4/MH_2$ (M= Mg, Ti) powder systems. *international journal of hydrogen energy*, 35(11):5434–5441, 2010.

[99] P.J. Linstrom. Nist standard reference database number 69. *NIST chemistry WebBook*, 2003.

[100] M. Martin, C. Gommel, C. Borkhart, and E. Fromm. Absorption and desorption kinetics of hydrogen storage alloys. *Journal of alloys and compounds*, 238(1-2):193–201, 1996.

[101] L. Stock. Structural thermochemistry of solids. *Thermochimica acta*, 148:149–164, 1989.

[102] K. Chou and K. Xu. A new model for hydriding and dehydriding reactions in intermetallics. *Intermetallics*, 15(5-6):767–777, 2007.

[103] J.T. Carstensen. Stability of solids and solid dosage forms. *Journal of pharmaceutical sciences*, 63(1):1–14, 1974.

[104] J.W. Christian. *The theory of transformations in metals and alloys*. Newnes, 2002.

[105] Y. Pang and Q. Li. A review on kinetic models and corresponding analysis methods for hydrogen storage materials. *international journal of hydrogen energy*, 41(40):18072–18087, 2016.

[106] A. Khawam and D.R. Flanagan. Solid-state kinetic models: basics and mathematical fundamentals. *The journal of physical chemistry B*, 110(35):17315–17328, 2006.

[107] W. Jander. Reaktionen im festen zustande bei höheren temperaturen. reaktionsgeschwindigkeiten endotherm verlaufender umsetzungen. *Zeitschrift für anorganische und allgemeine Chemie*, 163(1):1–30, 1927.

[108] A.M. Ginstling and B.I. Brounshtein. Concerning the diffusion kinetics of reactions in spherical particles. *Journal of applied chemistry of the USSR*, 23(12):1327–1338, 1950.

[109] A.T.W. Kempen, F. Sommer, and E.J. Mittemeijer. Determination and interpretation of isothermal and non-isothermal transformation kinetics; the effective activation energies in terms of nucleation and growth. *Journal of materials science*, 37:1321–1332, 2002.

[110] O. Kircher and M. Fichtner. Hydrogen exchange kinetics in $NaAlH_4$ catalyzed in different decomposition states. *Journal of applied physics*, 95(12):7748–7753, 2004.

[111] K. Koga, T. Ikeshoji, and K. Sugawara. Size-and temperature-dependent structural transitions in gold nanoparticles. *Physical review letters*, 92(11):115507, 2004.

[112] E. Roduner. Size matters: why nanomaterials are different. *Chemical society reviews*, 35(7):583–592, 2006.

[113] J. Jortner. Cluster size effects. *Zeitschrift für Physik D Atoms, Molecules and Clusters*, 24:247–275, 1992.

[114] Victor-Ishrayelu Merupo, Subramaniam Velumani, Karolina Ordon, Nicolas Errien, Jacek Szade, and Abdel-Hadi Kassiba. Structural and optical characterization of ball-milled copper-doped bismuth vanadium oxide (bivo 4). *CrystEngComm*, 17(17):3366–3375, 2015.

[115] R. Prabhukhot Prachi, M. Wagh Mahesh, and C. Gangal Aneesh. A review on solid state hydrogen storage material. *Advanced energy power*, 4(11), 2016.

[116] A. Zaluska, L. Zaluski, and J.O. Ström-Olsen. Nanocrystalline magnesium for hydrogen storage. *Journal of alloys and compounds*, 288(1-2):217–225, 1999.

[117] R.W.P. Wagemans, J.H. van Lenthe, P.E. de Jongh, A.J. Van Dillen, and K.P. de Jong. Hydrogen storage in magnesium clusters: quantum chemical study. *Journal of the american chemical society*, 127(47):16675–16680, 2005.

[118] A. Pundt. Hydrogen in nano-sized metals. *Advanced engineering materials*, 6(1-2):11–21, 2004.

[119] A.F. Gross, J.J. Vajo, S.L. Van Atta, and G.L. Olson. Enhanced hydrogen storage kinetics of $LiBH_4$ in nanoporous carbon scaffolds. *The journal of physical chemistry C*, 112(14):5651–5657, 2008.

[120] E.E. Santiso, A.M. George, C.H. Turner, M.K. Kostov, K.E. Gubbins, M. Buongiorno-Nardelli, and M. Sliwinska-Bartkowiak. Adsorption and catalysis: The effect of confinement on chemical reactions. *Applied surface science*, 252(3):766–777, 2005.

[121] YongJun Cho, Hyun Cho, and Eun Seon Cho. Nanointerface engineering of metal hydrides for advanced hydrogen storage. *Chemistry of Materials*, 35(2):366–385, 2023.

[122] Y. Wang and Y. Wang. Recent advances in additive-enhanced magnesium hydride for hydrogen storage. *Progress in natural science: materials international*, 27(1):41–49, 2017.

[123] O. Friedrichs, F. Aguey-Zinsou, J.R.A. Fernandez, J.C. Sanchez-Lopez, A. Justo, T. Klassen, R. Bormann, and A. Fernandez. MgH_2 with Nb_2O_5 as additive, for hydrogen storage: Chemical, structural and kinetic behavior with heating. *Acta materialia*, 54(1):105–110, 2006.

[124] M. Zhang and P.M. Kelly. Edge-to-edge matching model for predicting orientation relationships and habit planes—the improvements. *Scripta materialia*, 52(10):963–968, 2005.

[125] M. Zhang and P.M. Kelly. Edge-to-edge matching and its applications: Part ii. application to Mg–Al, Mg–Y and Mg–Mn alloys. *Acta materialia*, 53(4):1085–1096, 2005.

[126] P.M. Kelly and M-X Zhang. Edge-to-edge matching-the fundamentals. *Metallurgical and materials transactions*, 37(3A):833, 2006.

[127] M. Zhang, P.M. Kelly, M.A. Easton, and J.A. Taylor. Crystallographic study of grain refinement in aluminum alloys using the edge-to-edge matching model. *Acta materialia*, 53(5):1427–1438, 2005.

[128] G. Hübschen, I. Altpeter, R. Tschuncky, and H. Herrmann. *Materials characterization using nondestructive evaluation (NDE) methods*. Woodhead publishing, 2016.

[129] B. Fultz and J.M. Howe. *Transmission electron microscopy and diffractometry of materials*. Springer Science & Business Media, 2012.

[130] X. Mu, D. Wang, T. Feng, and C. Kübel. Radial distribution function imaging by stem diffraction: Phase mapping and analysis of heterogeneous nanostructured glasses. *Ultramicroscopy*, 168:1–6, 2016.

[131] W.H. Bragg and W.L. Bragg. The reflection of x-rays by crystals. *Proceedings of the royal society of London. Series A, Containing papers of a mathematical and physical character*, 88(605):428–438, 1913.

[132] D.B. Williams and C.B. Carter. The transmission electron microscope. In *Transmission electron microscopy*. Springer, 1996.

[133] Gatan Ltd. 4d stem @ONLINE. `https://www.gatan.com/techniques/4d-stem`. [Accessed 2023-05-06].

[134] Colin Ophus. Four-dimensional scanning transmission electron microscopy (4d-stem): From scanning nanodiffraction to ptychography and beyond. *Microscopy and Microanalysis*, 25(3):563–582, 2019.

[135] M. Born and E. Wolf. Principles of optics, 7th (expanded) edition. *United Kingdom: Press syndicate of the University of Cambridge*, 461:93, 1999.

[136] J.W. Goodman and P. Sutton. Introduction to fourier optics. *Quantum and semiclassical optics-journal of the european optical society part B*, 8(5):1095, 1996.

[137] J.C.H. Spence and A.V. Crewe. Experimental high-resolution electron microscopy. *Physics today*, 34(9):90, 1981.

[138] J.M. Cowley. *Diffraction physics*. Elsevier, 1995.

[139] B.B. Baker and E.T. Copson. *The mathematical theory of Huygens' principle*, volume 329. American Mathematical Soc., 2003.

[140] Y. Liao. Practical electron microscopy and database. *An online book*, 2006.

[141] JEOL Ltd. phase-contrast transfer function @ONLINE. `https://www.jeol.co.jp/en/words/emterms/search_result.html?keyword=phase-contrast%20transfer%20function`. [Accessed 2023-05-06].

[142] O. Scherzer. Über einige fehler von elektronenlinsen. *Zeitschrift für Physik*, 101(9):593–603, 1936.

[143] O. Scherzer. The theoretical resolution limit of the electron microscope. *Journal of applied physics*, 20(1):20–29, 1949.

[144] M.G. Burt. Fundamentals of envelope function theory for electronic states and photonic modes in nanostructures. *Journal of physics: Condensed matter*, 11(9):53, 1999.

[145] R. Jenkins, J.L. de Vries, and J.L. De Vries. Practical x-ray spectrometry. 1967.

[146] J.C. Russ. *Fundamentals of energy dispersive X-ray analysis: Butterworths monographs in materials*. Butterworth-Heinemann, 2013.

[147] Gatan Ltd. Spectrum imaging @ONLINE. `https://www.gatan.com/techniques/spectrum-imaging`. [Accessed 2023-05-06].

[148] R. Castaing. Application of electron probes to local chemical and crystallographic analysis. *Ph. D. Thesis (University of Paris)*, 1951.

[149] M. Watanabe and D.B. Williams. The quantitative analysis of thin specimens: a review of progress from the cliff-lorimer to the new ζ-factor methods. *Journal of microscopy*, 221(2):89–109, 2006.

[150] TU Graz. Electron energy loss spectroscopy - eels @ONLINE. `http://lampx.tugraz.at/~hadley/ss2/quasiparticles/eels/eels.php`. [Accessed 2023-05-06].

[151] Gatan Ltd. Quantify extracted signal @ONLINE. `https://eels.info/how/quantification/quantify-extracted-signal`. [Accessed 2023-05-06].

[152] Gatan Ltd. Extract signal @ONLINE. `https://eels.info/how/quantification/extract-signal`. [Accessed 2023-05-06].

[153] H. Tan, J. Verbeeck, A. Abakumov, and G. Van Tendeloo. Oxidation state and chemical shift investigation in transition metal oxides by eels. *Ultramicroscopy*, 116:24–33, 2012.

[154] X. Mu, A. Mazilkin, C. Sprau, A. Colsmann, and C. Kübel. Mapping structure and morphology of amorphous organic thin films by 4d-stem pair distribution function analysis. *Microscopy*, 68(4):301–309, 2019.

[155] J. Radon. 1.1 über die bestimmung von funktionen durch ihre integralwerte längs gewisser mannigfaltigkeiten. *Classic papers in modern diagnostic radiology*, 5:21, 2005.

[156] J. Trampert and J. Leveque. Simultaneous iterative reconstruction technique: physical interpretation based on the generalized least squares solution. *Journal of geophysical research: Solid earth*, 95(B8):12553–12559, 1990.

[157] P. Gilbert. Iterative methods for the three-dimensional reconstruction of an object from projections. *Journal of theoretical biology*, 36(1):105–117, 1972.

[158] M. Radermacher. Weighted back-projection methods. In *Electron tomography*, pages 245–273. Springer, 2007.

[159] J.R. Kremer, D.N. Mastronarde, and J.R. McIntosh. Computer visualization of three-dimensional image data using imod. *Journal of structural biology*, 116(1):71–76, 1996.

[160] O. Jin, Y. Shang, X. Huang, X. Mu, D.V. Szabó, T.T. Le, S. Wagner, C. Kübel, C. Pistidda, and A. Pundt. Microstructural study of MgB_2 in the $LiBH_4$-MgH_2 composite by using tem. *Nanomaterials*, 12(11):1893, 2022.

[161] O. Jin, Y. Shang, X. Huang, D.V. Szabó, T.T. Le, S. Wagner, T. Klassen, C. Kübel, C. Pistidda, and A. Pundt. Transformation kinetics of $LiBH_4$–MgH_2 for hydrogen storage. *Molecules*, 27(20):7005, 2022.

[162] Ou Jin, Yuanyuan Shang, Xiaohui Huang, Dorothée Vinga Szabó, Thi Thu Le, Stefan Wagner, Thomas Klassen, Christian Kübel, Claudio Pistidda, and Astrid Pundt. Transformation kinetics of $libh_4$–mgh_2 for hydrogen storage. *Molecules*, 27(20):7005, 2022.

[163] J-Ph Soulié, Guillaume Renaudin, R Černỳ, and Klaus Yvon. Lithium boro-hydride $LiBH_4$: I. crystal structure. *Journal of alloys and compounds*, 346(1-2):200–205, 2002.

[164] B. Bogdanović, M. Felderhoff, and G. Streukens. Hydrogen storage in complex metal hydrides. *Journal of the serbian chemical society*, 74(2):183–196, 2009.

[165] Ou Jin, Yuanyuan Shang, Xiaohui Huang, Xiaoke Mu, Dorothée Vinga Szabó, Thi Thu Le, Stefan Wagner, Christian Kübel, Claudio Pistidda, and Astrid Pundt. Microstructural study of mgb2 in the $libh_4$–mgh_2 composite by using tem. *Nanomaterials*, 12(11):1893, 2022.

[166] Ruiming Ren, Angel L Ortiz, Tippawan Markmaitree, William Osborn, and Leon L Shaw. Stability of lithium hydride in argon and air. *The Journal of Physical Chemistry B*, 110(21):10567–10575, 2006.

[167] Patrick J Herley and William Jones. Transmission electron microscopy of beam-sensitive metal hydrides. *Zeitschrift für Physikalische Chemie*, 147(1_2):147–159, 1986.

[168] S. Lee. Crystal growth of MgB2. *Physica C: Superconductivity*, 385(1-2):31–41, 2003.

[169] J. Liu and D. Xue. Thermal oxidation strategy towards porous metal oxide hollow architectures. *Advanced materials*, 20(13):2622–2627, 2008.

[170] AD Smigelskas. Zinc diffusion in alpha brass. *Trans. Aime*, 171:130–142, 1947.

[171] T.E.C. Price, D.M. Grant, V. Legrand, and G.S. Walker. Enhanced kinetics for the $LiBH_4$:MgH_2 multi-component hydrogen storage system–the effects of stoichiometry and decomposition environment on cycling behaviour. *International journal of hydrogen energy*, 35(9):4154–4161, 2010.

[172] PM Kelly and M-X Zhang. Edge-to-edge matching-a new approach to the morphology and crystallography of precipitates. In *Materials Forum*, volume 23, pages 41–62, 1999.

[173] G. Parker. Encyclopedia of materials: science and technology. 2001.

[174] J. Zhang, Y. Zhang, K. Xu, and V. Ji. Anisotropic elasticity in hexagonal crystals. *Thin solid films*, 515(17):7020–7024, 2007.

[175] V. Milman and M.C. Warren. Elastic properties of TiB_2 and MgB_2. *Journal of physics: condensed matter*, 13(24):5585, 2001.

[176] C.F. Cline, H.L. Dunegan, and G.W. Henderson. Elastic constants of hexagonal BeO, ZnS, and CdSe. *Journal of applied physics*, 38(4):1944–1948, 1967.

[177] chemicalbook. Sodium borohydride @ONLINE. `https://www.chemicalbook.com/ChemicalProductProperty_EN_CB5322426.htm`. [Accessed 2023-09-06].

[178] KM Unruh, TE Huber, and CA Huber. Melting and freezing behavior of indium metal in porous glasses. *Physical Review B*, 48(12):9021, 1993.

[179] Alfred René Ubbelohde. Melting and crystal structures. *(No Title)*, 1965.

[180] Toru Moriwaki, Yuichi Akahama, Haruki Kawamura, Satoshi Nakano, and Kenichi Takemura. Structural phase transition of rutile-type MgH_2 at high pressures. *Journal of the Physical Society of Japan*, 75(7):074603, 2006.

[181] Albert W Hull. The crystal structures of the common elements. *Journal of the Franklin Institute*, 193(2):189–216, 1922.

[182] RS Calder, W Cochran, D Griffiths, and RD Lowde. An x-ray and neutron diffraction analysis of lithium hydride. *Journal of Physics and Chemistry of Solids*, 23(6):621–632, 1962.

[183] Sergey Lee, Hatsumi Mori, Takahiko Masui, Yuri Eltsev, Ayako Yamamoto, and Setsuko Tajima. Growth, structure analysis and anisotropic superconducting properties of MgB_2 single crystals. *Journal of the Physical Society of Japan*, 70(8):2255–2258, 2001.

[184] H Ott. Die raumgitter der lithiumhalogenide. *Physikalische Zeitschrift*, 24:209–213, 1923.

[185] VG Tsirelson, AS Avilov, Yu A Abramov, EL Belokoneva, R Kitaneh, and D Feil. X-ray and electron diffraction study of mgo. *Acta Crystallographica Section B: Structural Science*, 54(1):8–17, 1998.

[186] Thorsten Hegenscheidt. *Möglichkeiten und Grenzen des Röntgen-Beugungsexperiments, aufgezeigt am Beispiel dreierëinfacherSStrukturen*. na, 1998.

[187] Gatan Ltd. Eels atlas ti @ONLINE. `https://eels.info/atlas/titanium`. [Accessed 2023-08-21].